TIME-RESOLVED NOISE SOURCE ANALYSIS IN SUBSONIC TURBULENT JETS

David E. S. Breakey

May 2014

Department of Mechanical and Manufacturing Engineering
Parsons Building, Trinity College
Dublin 2, Ireland

A thesis submitted to the University of Dublin in partial fulfillment of the requirements for the degree of PhD.

Declaration

I declare that this thesis has not been submitted as an exercise for a degree at this or any other university, and it is entirely my own work.

I agree to deposit this thesis in the University's open access institutional repository or allow the library to do so on my behalf, subject to Irish Copyright Legislation and Trinity College Library conditions of use and acknowledgement.

David E. S. Breakey, May 2014

At the tumultuous noise peoples flee;
when you lift yourself up, nations are scattered,
– Isaiah 33:3

S. D. G.

Abstract

For over sixty years, researchers have been trying to understand and predict jet noise emissions, seeking to reduce perceived noise levels for passengers and those who live and work near airports. The complexity of jet noise source mechanics has meant that an adequate theory of jet noise—one yielding predictions sufficiently accurate to fully incorporate noise concerns into the aircraft design cycle—does not yet exist.

This thesis contributes to the understanding of jet noise sources by developing and testing tools for the time-resolved analysis of jet noise sources. The time-resolved approach provides extra insight that is masked in a purely statistical analysis of the source dynamics.

First, time-resolved Particle Image Velocimetry is used to directly correlate jet velocity fluctuations with out-of-flow sound signals, yielding two principal advantages over traditional velocimetry techniques: temporal resolution of the development of individual flow features; and an estimate of the space–frequency coherence. The measured time-domain quantities are accurate, but in the frequency domain, errors arising from a combination of high-frequency aliasing and signal noise make the estimates inaccurate. Nonetheless, the correlation signature in a low-speed jet with a Mach number of 0.25 is shown to be consistent with a large-scale oscillatory source called a wavepacket.

Second, the pressure field of a jet with a Mach number of 0.6 is investigated to detect the presence of linear wavepackets in the near field. Beyond the end of the potential core, the wavepacket signatures are masked by incoherent pressure fluctuations, but filtering by Proper Orthogonal Decomposition (POD) reveals signatures that closely match predictions available from the Parabolized Stability Equations, indicating the presence of wavepackets. A new technique is developed for projecting time-domain pressure measurements onto a statistically obtained POD basis, yielding the time-resolved activity of each POD mode. Correlations between the first POD mode and the far-field pressure indicate that a single POD mode captures the salient near-field–far-field correlation signature; however, the signatures of the other modes also indicate acoustically important near-field behaviour. An existing technique based on the Green's function solution of wavepacket fluctuations is used with the near-field data to obtain far-field predictions, but the agreement with measurements is not good for the jet studied. This is shown to be the result of the appearance of a spurious source artificially introduced by the finite extent of the microphone array used in the measurements, an effect expected to be smaller for higher-Mach-number jets. Despite this shortcoming, the existing technique is extended to provide time-domain far-field pressure predictions. The technique is demonstrated using an artificial dataset, but it will be necessary to treat the problem of the spurious source before meaningful results for experimental data can be obtained.

Third, a structural similarity metric originating from image compression analysis is adapted for time-resolved aeroacoustic signals. When faced with common types of aeroacoustic errors, the new metric outperforms traditional quantitative metrics for comparing the similarity between signals, providing better discrimination between error types while remaining resilient to contamination by random signal noise. Such a metric shows promise for optimization-based development of noise source prediction schemes.

As with most complex problems in engineering research, the developments presented in this thesis have also opened a new set of research questions. Particularly, with the mounting evidence that reduced-order projections can capture the salient acoustically important dynamics of a jet flow, is the detail provided by time-resolved PIV really worth the experimental effort? And further, in the development of noise source prediction schemes, what constitutes a successful noise prediction? Future researchers will need to answer these questions along the road to practical jet noise predictions and—ultimately—practical jet noise reductions.

Acknowledgements

This project was conceived by Prof. John Fitzpatrick, who also guided me in its early stages. I am indebted to John for his insight and experience in navigating the problem of jet noise and the maze of academia. It is only unfortunate that he did not live to see me through to the end. I also thank Dr. Craig Meskell for taking me on as his student after John's death. Craig's careful guidance, creative insight, and patient oversight during the analysis of the data and dissemination of the results, particularly the compilation of this thesis, have benefited me greatly.

From my colleagues in Trinity, I would particularly like to thank Drs. John Mahon, Rayhaan Farrelly, and Shane Finnegan for teaching me experimental techniques. I also thank Miguel Garcia-Pedroche for his help in obtaining the TR-PIV data.

For the work on wavepackets, foremost I thank Drs. Peter Jordan and André Cavalieri, who introduced me to wavepacket analysis. Particularly, I thank Peter for hosting me in the *Centre d'études aérodynamiques et thermiques* (CEAT) in Poitiers, France so that I could perform my experimental campaign. Peter and André also helped in the collection of the pressure data and—perhaps most importantly—included me in their discussions of the mystery of wavepackets and the jet noise puzzle. They also guided me in the analysis of the current data and the development of my wavepacket analysis techniques. I would like to thank Dr. Olivier Léon for providing the code for the statistical predictions of the far-field emissions of near-field wavepackets. I also thank Dr. Daniel Rodríguez and Prof. Tim Colonius for their provision of the Parabolised Stability Equation solutions of the analyzed jet flow.

This work has been primarily funded by Science Foundation Ireland (SFI) within the project "Modelling and identification of turbulent source mechanisms for subsonic jet noise" under contract 09/RFP/ENM2469. I have also been supported throughout this work by the Natural Sciences and Engineering Research Council of Canada (NSERC). The measurements taken at CEAT were obtained in cooperation with the EU–Russian program ORINOCO (FP7-AAT-2010-RTD-Russia; project number 266103) and with *Agence nationale de la recherche* (ANR) through the project Cool Jazz (**CO**ntrol-**O**riented **L**inear and non-linear models for **J**et **A**eroacoustic**ZZ**).

Prior publications

Many of the ideas and figures contained in this thesis have been previously presented in the following publications:

Breakey D & Meskell C (2013) Comparison of metrics for the evaluation of similarity in acoustic pressure signals. *Journal of Sound and Vibration* 332(15):3605–3609.

Breakey DES & Fitzpatrick JA (2012) Time-resolved PIV for aeroacoustic source analysis. In: *16th International Symposium on the Application of Laser Techniques to Fluid Mechanics*, Lisbon, Portugal.

Breakey DES, Fitzpatrick JA, & Meskell C (2013a) Aeroacoustic source analysis using time-resolved PIV in a free jet. *Experiments in Fluids* 54(5):1–16.

Breakey DES, Jordan P, Cavalieri AVG, Léon O, Zhang M, Lehnasch G, Colonius T, & Rodríguez D (2013b) Near-field wavepackets and the far-field sound of a subsonic jet. In: *19th AIAA/CEAS Aeroacoustics Conference*, Berlin, Germany.

Kennedy J & **Breakey DES** (2013) A simple model for the frequency dependence of turbulence length scales in jets. In: *19th AIAA/CEAS Aeroacoustics Conference*, Berlin, Germany.

Contents

List of figures

Chapter 2

List of tables

Nomenclature

Functions and variables

$\gamma^2_{ab}(\omega)$	Coherence function
$\delta(\cdot)$	Dirac delta function
δ_{ij}	Kronecker delta function, $\delta_{ij} = 1$ when $i = j$ and $\delta_{ij} = 0$ when $i \neq j$
θ	Observer angle measured from downstream jet axis
λ	Wavelength
μ	Dynamic fluid viscosity
ρ	Fluid density, mass per unit volume
σ_a	Root-mean-square of a data series, *i.e.* $\sigma_a = \text{RMS}[a(t)]$
τ	Time lag
τ_r	Retarded time lag, $\tau - \lvert\mathbf{x}_o - \mathbf{x}_s\rvert/c_0$
$\Psi(\zeta)$	Wavelet mother function
ω	Angular frequency, $2\pi f$
a, b	Generic time-series variables, *i.e.* $a(t), b(t)$
c_0	Speed of sound in ambient reference conditions
D	Jet diameter
dB	Decibels
f	Frequency
$G_{aa}(f)$	Autospectral density of a
$G_{ab}(f)$	Cross-spectral density between a and b
k	Wavenumber, $2\pi/\lambda$
M	Mach number, U/c_0
p_{ref}	Acoustic reference pressure, $2 \cdot 10^{-5}$ Pa

$R_{aa}(\tau)$	Autocorrelation function of a with time lag τ
$R_{ab}(\tau)$	Cross-correlation function between a and b with time lag τ
Re	Reynolds number, $\rho_J UD/\mu_J$
s	Wavelet scale
t	Time
T_{ij}	Lighthill stress tensor
U	Mean jet velocity at the centre of the nozzle exit
u, v, w	Velocity component in x, y, z direction, respectively
$W_{i,\mathrm{PIV}}$	PIV interrogation window length in the i direction
x, r, ϕ	Spatial coordinates in a cylindrical reference frame anchored at the centre of the jet exit
x, y, z	Spatial coordinates in a Cartesian reference frame anchored at the centre of the jet exit
$\mathbf{x}_o$	Observer location
$\mathbf{x}_s$	Source location

Operators

*	Complex conjugation
$\bar{\ }$	Designates time-averaged part of quantity, *i.e.* $a = \overline{a} + a'$
$'$	Designates time-fluctuating part of quantity, *i.e.* $a = \overline{a} + a'$
$\langle\ \rangle$	Ensemble average

Subscripts

0	Value taken at ambient reference conditions
c	Value for convection quantity
i, j, k	Vector indices
J	Quantity measured at jet exit
o	Denotes observer location
RMS	Root-Mean-Square
s	Denotes source location

Acronyms

ACARE	Advisory Council for Aviation Research and Innovation in Europe
AOI	Area Of Interest
BBSAN	Broadband Shock Associated Noise
CFD	Computational Fluid Dynamics
CSM	Cross-Spectral Matrix
CTA	Constant Temperature Anemometry
CWT	Continuous Wavelet Transform
DNS	Direct Numerical Simulation
DWT	Discrete Wavelet Transform
EPNdB	Effective Perceived Noise Decibels
EPNL	Effective Perceived Noise Level
FOV	Field Of View
FSS	Fine-Scale Similarity
HWA	Hot-Wire Anemometry
ICAO	International Civil Aviation Organization
LDA	Laser Doppler Anemometry
LES	Large Eddy Simulation
LSS	Large-Scale Similarity
LST	Linear Stability Theory
MSE	Mean-Square-Error metric
MSSIM	Mean SSIM
PIV	Particle Image Velocimetry
PNL	Perceived Noise Level
PNLT	Tone-corrected Perceived Noise Level
POD	Proper Orthogonal Decomposition
PSE	Parabolized Stability Equations
RANS	Reynolds-averaged Navier–Stokes
RE	Relative-Energy metric

RMS	Root-Mean-Square
SPL	Sound Pressure Level
SSIM	Structural Similarity Metric
TR-PIV	Time-Resolved PIV
WSSIM	Time–frequency Weighted SSIM
$\mathrm{WSSIM}_{\mathrm{1D}}$	Time-domain Weighted SSIM

Chapter 1

Introduction

1.1 Context for jet noise research

Today, the aviation industry is at the heart of culture and commerce worldwide, connecting communities and businesses to an extent that could not have been conceived of only a century ago. The International Civil Aviation Organization (ICAO) notes that airlines carried 2.3 billion passengers and 38 million tonnes of freight in 2009, and air traffic is expected to grow steadily for the foreseeable future (ICAO-ER, 2010). Such growth generates significant challenges as the aviation industry seeks to adapt to global needs for more sustainable and accessible air transport. One of the most important of these challenges is reducing the noise emitted by aircraft, particularly near airports, where the most significant community opposition to airport expansion and operation arises from noise concerns (ICAO-ER, 2010). In response to this challenge, the Advisory Council for Aviation Research and Innovation in Europe (ACARE) has set an ambitious goal for noise reductions by 2050: a 65% reduction in perceived noise levels relative to the year 2000 (ACARE-SRIA, 2012). Similar goals have also been put in place by similar agencies worldwide.

Since people living or working near airports are those most significantly affected by aircraft noise, takeoff and landing are the most crucial periods for the control of noise emissions. Daytime and nighttime noise limits are put in place by regulatory agencies to protect those affected from the negative health effects associated with noise exposure (WHO-NNGL, 2007), and it is up to the aerospace research community to reduce aircraft noise emission levels to allow the aviation industry to meet the growing global need for air travel while meeting these limits. Aircraft noise can be categorized by the component of the aircraft from which it emanates. At takeoff, when the engines must operate at high power to lift the aircraft off the ground, the most significant contribution to aircraft noise is generated by the mixing of the jet plume exiting the engine with the ambient air (Viswanathan, 2010). This noise component, called *jet noise*, is generated by aerodynamic phenomena rather than mechanical phenomena such as engine vibrations.

The study of the aerodynamic generation of sound—or *aeroacoustics*—began with the foundational work of Lighthill (1952) over sixty years ago. In part due to Lighthill's (1952) work, aircraft today are significantly quieter than those manufactured at that time; however, aircraft noise concerns are just as important as ever, and the source mechanisms of jet noise are not well enough understood to fully incorporate noise concerns into the aircraft design cycle. Noise predictions are possible but difficult to verify before the testing and prototyping stages, and they are highly reliant on empirical constants. Accurate numerical simulations are possible for simple jets, but their computational expense is too great for use as prediction tools, and they do not contribute directly to the understanding of jet noise source mechanisms since they can determine if a jet is louder or quieter but not specifically why. Fledgling noise reduction technologies take decades to incorporate into production aircraft and the noise reductions have been moderate. An adequate theory of jet noise requires the understanding of noise source mechanisms in jets necessary to create accurate, robust noise source models and the predictive power necessary to incorporate noise concerns directly into the aircraft design cycle. Such a theory will pave the way toward significant practical jet noise reductions.

1.2 Project context and overview

1.2.1 Toward time-resolved jet noise source analysis

The development of an adequate theory of jet noise is far from finished. More fundamental research is necessary to determine the nature of the noise source mechanisms in jet turbulence and how their signatures propagate to the far field. Traditionally, this endeavour has been focused on statistically describing an equivalent source and applying an approximate noise propagation model. Recent evidence has pointed to the possibility that real-time dynamics of the sound sources may be important for both prediction and control (Cavalieri *et al.*, 2011; Jordan & Colonius, 2013), and to that end, this thesis focuses on the time-resolved analysis of noise source signatures. Though for regulatory purposes, the only pertinent emission parameters are statistical, analyzing noise sources in the time domain is still appropriate because of the different information apparent from a time-domain perspective and because of the possibility that effective noise control may be achieved by interaction with the jet noise sources in real time.

Though tracking or describing turbulence in real time is not a feasible proposition, like many real-life engineering challenges, practical jet noise reduction may not necessarily result simply from adding more information to jet noise models, but from carefully interpreting the information that is already available using current measurement techniques. This extra understanding available from a time-domain perspective may lead to novel noise reduction devices and strategies that would not have been developed looking only at a statistical picture of a jet's noise emissions.

1.2.2 Objectives

This thesis develops techniques for time-resolved analysis of jet noise sources and far-field sound. The objectives of this project are to

- determine the utility of a space-resolved and time-resolved Particle Image Velocimetry to a low-speed jet and use it to interpret in-flow sound source signatures,
- detect the signatures of large-scale structures in the near-field of a subsonic jet and use the near-field signatures to predict the far-field sound in the time domain,
- and develop a comparison tool for evaluating the similarity between time-domain aeroacoustic signals.

These objectives have been met and the results of each are presented in chapters 3, 4, and 5, respectively.

1.2.3 Progress beyond the state of the art

The feature of this thesis as a whole that sets it apart from other past and current endeavours in jet noise research is the focus on time-domain analysis, giving a different perspective on jet noise sources while remaining in the purview of traditional jet noise measurements. Particularly, in chapter 3, the application of time-resolved Particle Image Velocimetry—a modern measurement technique now frequently used in aeroacoustics—in a traditional cross-correlation source analysis technique represents a step forward, opening the door for space–frequency-domain analysis of jet noise sources while still retaining the space–time information obtained by the recording of each flow realization. For the pressure measurement analysis in chapter 4, the simultaneous recording of both near-field and far-field pressures allows the correlation between near-field and far-field azimuthal modes to be determined, and it allows the projection of these modes onto reduced-order representations in the time domain.

Finally, chapter 5 is the first application of a comparison metric for time-domain aeroacoustic signals that is suitable for use in quantitative comparison of time-domain aeroacoustics signals, which could be used to help isolate acoustically important noise model parameters.

Though this work does not claim to solve the problem of jet noise, following in the footsteps of a long series of gifted researchers, it constitutes another step on the path to a truly adequate theory of jet noise, which will contribute to the achievement of the long-term noise reduction goals of the aviation industry.

1.3 Thesis overview

Chapter 2 describes the theoretical and historical background to this thesis in detail, providing the context necessary to understand and motivate the current work. The analytical and experimental work performed is presented in three chapters representing different strands of the analysis, each aligned with one of the objectives mentioned in § 1.2.2. These describe an aeroacoustic source analysis of a low-speed jet using time-resolved Particle Image Velocimetry (chapter 3), the statistical and time-resolved prediction of far-field sound from near-field wavepackets in a subsonic jet (chapter 4), and the comparison of time-domain aeroacoustic signals through the application of a new similarity metric (chapter 5). Each of these chapters provides extra theoretical and historical context tracing the development of the pertinent techniques for jet noise prediction. Each chapter also ends with a brief summary of the important findings and outlines some potential avenues for further research in each area. Similarly, chapter 6 summarizes the findings of the project as a whole and prescribes directions for future research.

Chapter 2

Background

2.1 Aims of jet noise research

Jet noise emissions are an important aspect of aircraft design, but they are not the only challenge facing aircraft designers. The design process in aeronautics is fraught with compromises, and improvements in one aspect of an aircraft's design frequently have negative impacts on other design concerns. The primary aim of jet noise research is to achieve jet noise reductions with minimum negative impact on other factors of the aircraft design. These factors include aircraft weight, performance (*i.e.* thrust), fuel consumption, and cost. The design modifications necessary to achieve these reductions must not adversely affect the other design concerns beyond an acceptable level. However, the current tools available to jet noise researchers do not allow an accurate prediction of the jet noise emissions of a novel engine design at the concept stage, requiring lengthy iterative testing of new designs, hindering the designer's ability to incorporate jet noise concerns into the design cycle. Therefore, a more complete theory of jet noise is required that has the following characteristics:

Understanding The sources of noise in turbulence should be identified so as to understand what makes a turbulent flow efficient at generating and radiating sound. The propagation of noise through a turbulent flow should also be understood so that the known sound source field can be interpreted as meaningful far-field noise emissions.

Prediction Theory should also lead to an effective, efficient method to predict the noise emissions of novel engine designs. Accurate radiated sound fields should be available to jet engine designers before the prototyping stage. Only when sufficient prediction tools exist will it be possible to fully integrate jet noise emissions into the aircraft design process.

Despite approximately sixty years of jet noise research since Lighthill's (1952) seminal paper, neither of these capacities is close to being adequately fulfilled. Practical jet noise reduction is still largely experimental and iterative, which is expensive and inefficient. As researchers continue to pursue an adequate theory, jet noise promises to be an active field of aeronautical research for many years to come.

Though these criteria have not yet been fulfilled, much progress has been achieved by the jet noise community in the last sixty years. The basic features of jet noise have been identified, as well as many qualitative and quantitative effects. For example, Lighthill's (1952) original paper led to approximate scaling laws showing the sound emissions increase exponentially with jet speed, and new larger-diameter, lower-speed engines have made jets significantly quieter than comparable aircraft from the 1950s and 1960s (see § 2.2.4). Simplified models of the sound sources in jets have also helped identify the importance of various jet design parameters. Also significant is the fact that, through decades of work, a considerable experimental database now exists in the literature evaluating jet designs at many different operational parameters, providing the opportunity for current and future researchers to make robust comparisons across a broad spectrum of jet types.

Finally, it is important to note that practical noise reductions do not require a complete time-resolved description of the far-field sound accurate to the measurement error of sound measurement equipment—such as could be achieved by direct solution of the equations of fluid motion—rather, it is only necessary that aircraft designers have the information necessary to compare jet designs based on their ability to meet regulatory noise limits and that the designers have enough confidence in this information to make informed design decisions. Hybrid solutions that begin by calculating the mean hydrodynamic field, which can be calculated in a reasonable time (*e.g.* Reynolds-Averaged Navier–Stokes (RANS) simulations), and then apply appropriate source models would be nearly as useful—and more practically feasible—to jet designers as complete solutions that require much higher computational cost.

2.2 Introduction to acoustics and aeroacoustics

2.2.1 What is sound?

In a fluid, *sound* can be described as pressure fluctuation that travels as a mechanical wave. For a pressure fluctuation to meet this criterion, it must satisfy the wave equation. The homogeneous wave equation for a pressure fluctuation in a uniform stagnant fluid—also called a quiescent fluid—is given as[1] (*e.g.* Hirschberg, 2001)

$$\frac{1}{c_0^2}\frac{\partial^2 p'}{\partial t^2} - \frac{\partial^2 p'}{\partial x_i^2} = 0, \tag{2.1}$$

where c_0 is the speed of sound in the fluid reference state, p is the local fluid pressure, t is time, x_i is the x-coordinate in the i direction. The $'$ denotes the fluctuating part of the variable[2]. Equation (2.1) applies only when there are no sources of sound in the medium since there is no source term on the right hand side. The importance of the wave equation is that it shows that all sound propagates at c_0. In contrast to sound, *pseudo-sound* (Rienstra & Hirschberg, 2010) is a pressure fluctuation that does not satisfy the wave equation (*i.e.* does not propagate at c_0). Pressure fluctuations due to sound in an otherwise quiescent fluid can therefore all be classified as sound, while fluctuations in a non-quiescent fluid, such as in turbulent regions in a jet, can be made up of both sound and pseudo-sound components. The part of a fluid's motion that is sound is often called the acoustic component, while the pseudo-sound part is the hydrodynamic component. Separating the two components in jet flows is usually non-trivial.

While acoustics is the study of sound in general, aeroacoustics is the study of sound generated by flow phenomena. Whereas acoustic sources arise from external phenomena, aeroacoustic sources are governed by the same fluid dynamical equations as the sound propagation itself. Since aeroacoustic sources are governed by these same equations, the principal difficulty in aeroacoustics is separating the fluctuations constituting an aeroacoustic source from other fluctuations in the flow that do not cause acoustic emissions.

Though the Navier–Stokes equations—which are thought to fully describe both hydrodynamic and acoustic fluid motion—are well known, the complexity of solving the acoustic solution for problems of practical interest is too great. This is complicated by the fact that the acoustic energy emitted by aeroacoustic sources is generally several orders of magnitude lower than that of the hydrodynamic fluctuations, meaning that the precision required in the analysis of aeroacoustic problems is several orders of magnitude finer than comparable aerodynamic problems. This is additionally complicated by the fact that high-frequency flow information, which is of little importance in aerodynamics, is especially important in aeroacoustics.

Though direct solutions of the Navier–Stokes equations can be obtained by Com-

[1] Equation (2.1) can be generalized for a fluid undergoing arbitrary motion as is described by Hirschberg (2001) and in § 2.2.4. It follows that, for a non-quiescent fluid, sound is the component of fluid motion that satisfies this generalized form of equation (2.1).

[2] Any generic time series variable, a, can be decomposed as $a = \overline{a} + a'$, where $\overline{a}$ is its time-averaged value, and a' is its fluctuating component.

putational Fluid Dynamics (CFD) methods, for aeroacoustic problems, the only type of CFD solution that yields far-field emissions directly is Direct Numerical Simulation (DNS), which requires that all spatial and temporal scales of the flow be well resolved over the entire computational domain. This is generally unfeasible for practical problems since the computational domain in practical aeroacoustics problems is large, encompassing far-field observers. This limitation can be overcome somewhat by reducing the size of the computational domain to contain only as much of the jet as necessary to capture the non-linear behaviour and then using linear propagation techniques to find the far-field emissions. Another common approach is to compute a Large Eddy Simulation (LES) rather than a DNS. The LES approach computes only the larger scales directly, leaving the smaller scales to be modelled by a suitable turbulence model. This reduces the computational cost of the solution for practical problems to the order of thousands of processor-hours, which in research settings has meant that LES and DNS solutions have become very important in the solution of benchmark problems for the development of noise source models, allowing those in the aeroacoustics community to compare and evaluate their models on comprehensive datasets free from experimental noise. However, their computational expense still precludes the incorporation of LES and DNS directly into the design cycle.

Since numerical solutions for practical jets are not readily available, experimental measurements are still the standard tool for generating jet noise databases suitable for aiding the development of new jet noise prediction schemes. The use of such experimental techniques has necessitated the development of formalized methods for measuring jet noise.

2.2.2 Noise measurement

In order to reduce jet noise emissions, it is imperative to understand noise measurement for regulatory purposes. Since those affected by jet noise are almost always far enough away that the dominant pressure fluctuations are acoustic, the tools used to measure noise and certify aircraft have mainly been adopted from sound measurement techniques. The human ear is typically sensitive to frequencies between 20 Hz and 20 kHz, but it does not perceive all frequencies equally well. For this reason, noise ratings are typically weighted so that noise at frequencies to which the human ear is more sensitive have a higher penalty than other frequencies during certification. A detailed review of sound measurement is given by Rienstra & Hirschberg (2010), and the techniques for aircraft noise measurements are given in CFR-14 (2011). Only the most pertinent points are repeated here.

Sound is typically measured in decibels (dB) and for certification purposes this measurement is usually based on the overall sound pressure level (OASPL) defined by

$$\mathrm{OASPL} = 20\log_{10}\left(\frac{p'_{\mathrm{RMS}}}{p_{\mathrm{ref}}}\right), \tag{2.2}$$

where p'_{RMS} is the root-mean-square of the acoustic pressure fluctuations and p_{ref} is the acoustic reference pressure of $2 \cdot 10^{-5}$ Pa, which is the pressure minimum detectable by the human ear. More specifically, a frequency-dependent version of the OASPL called the Sound Pressure Level (SPL) is obtained by calculating the OASPL for each of a number of octave bands[3]. These values are then converted into a unit of perceived noisiness called *noy* using a conversion table. Combining the noy values gives the Perceived Noise Level (PNL). Specific tones that are considered more annoying to human observers are given a tone correction factor which is added to the PNL, giving the Tone-corrected PNL (PNLT). The maximum PNLT is then added to a duration correction factor, which yields the Effective PNL (EPNL). The EPNL is the level that is regulated by international standards and is usually given in decibels (EPNdB). These measurements are taken at a number of positions while the plane takes off and lands. Regulating agencies typically set limits for flyover, approach, and sideline values. Additional considerations in the noise certification of aircraft are given by Peart *et al.* (1991).

Clearly, reductions in jet noise emissions cannot focus only on reducing overall sound power. The frequency of the emissions and peaks in the emission spectrum also play an important role. Moving peaks away from particularly annoying frequencies can be just as effective a way to reduce EPNL as reducing total power. Additionally, if it is possible to move sound power to frequencies to which the human ear is insensitive, reductions to EPNL can also be achieved. Also, the possibility to move sound power from the maximum PNLT to other PNLTs may also cause a reduction in EPNL without requiring reductions in overall sound power. Since jet noise measurements are made from the ground, where observers tend to be located, redirecting sound energy so that it primarily radiates away from the ground can also effectively reduce EPNL. These considerations make the aim of jet noise reductions feasible, even while the total power of jet engines continues to increase.

2.2.3 Turbulent jet

Figure 2.1 shows the structure of a typical turbulent jet and the classification of its regions while figure 2.2 shows the sign convections used in jet aeroacoustics for

[3]Traditionally, SPL has been calculated by filtering p' into $1/3$ octave bands and finding the Root-Mean-Square (RMS) for each band, but more modern calculations are based on the autospectrum of the p', which is roughly equivalent.

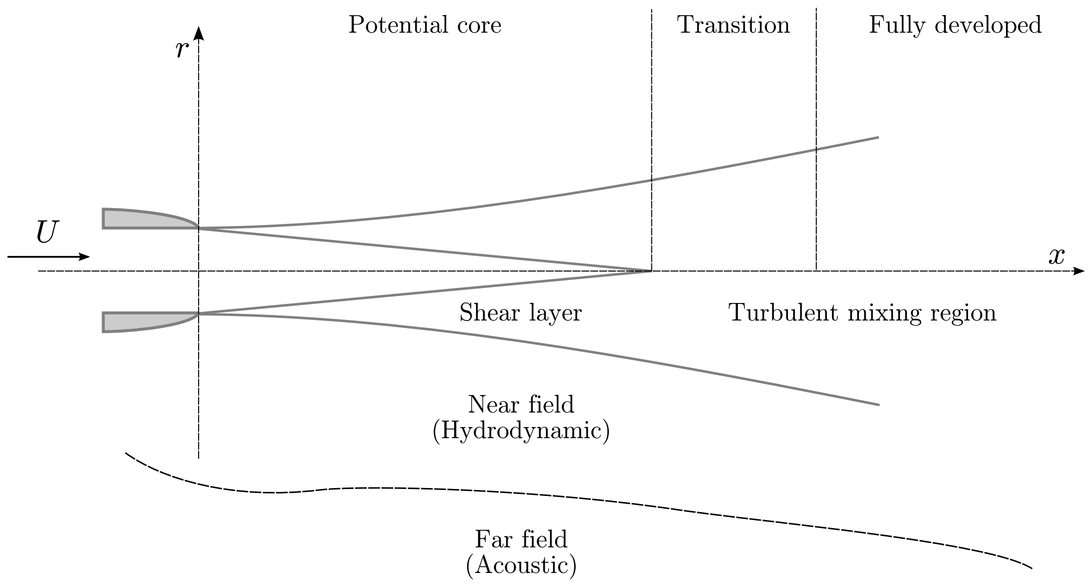

Figure 2.1: Turbulent jet schematic

various coordinate systems, all of which will be used at some point in this work.

For delineating the jet regions, the most important quantity is the instantaneous fluid velocity, $\mathbf{u}$, which is a three-component vector. In Cartesian coordinates, the velocity components in the x-, y-, and z-directions, respectively, are labelled u, v, and w. The *shear layer* is the region of the jet that begins at the lip-line of the nozzle where the fast-moving fluid exiting the jet interfaces with the surrounding fluid. In this region, the fast-moving jet fluid entrains the surrounding fluid and causes intense mixing. The flow in this region is highly turbulent and the mean velocity steadily decreases in the x-direction as the momentum from the jet is transferred to the previously stagnant, entrained fluid. The turbulence of the shear layer is much greater than that of the original jet. The shear layer grows both toward and away from the jet axis. The *potential core* is the region where the flow is still relatively undisturbed from the initial jet flow. It is where the shear layer still has not interrupted the original flow. It is defined as the area where $\overline{u} \geq 0.95U$, where U is the mean jet velocity at the centre of the nozzle exit. Thus the end of the potential core is when the mean centreline velocity is $0.95U$. This is where the shear layers from both sides of the jet join together. The turbulence of the potential core is characteristic of the original jet turbulence. The length of the potential core varies depending on the jet inlet conditions. Typical potential core lengths lie in the range $\approx 4.5 - 8D$, where D is the diameter of the jet (Ashforth-Frost & Jambunathan, 1996). In the *fully developed region*, the flow is completely turbulent and velocity profile broadens until the fluid is again stagnant. The flow in this region, which is highly turbulent, is self-similar because there are no intrinsic length or time scales in this part of the flow (Tam, 1998). The

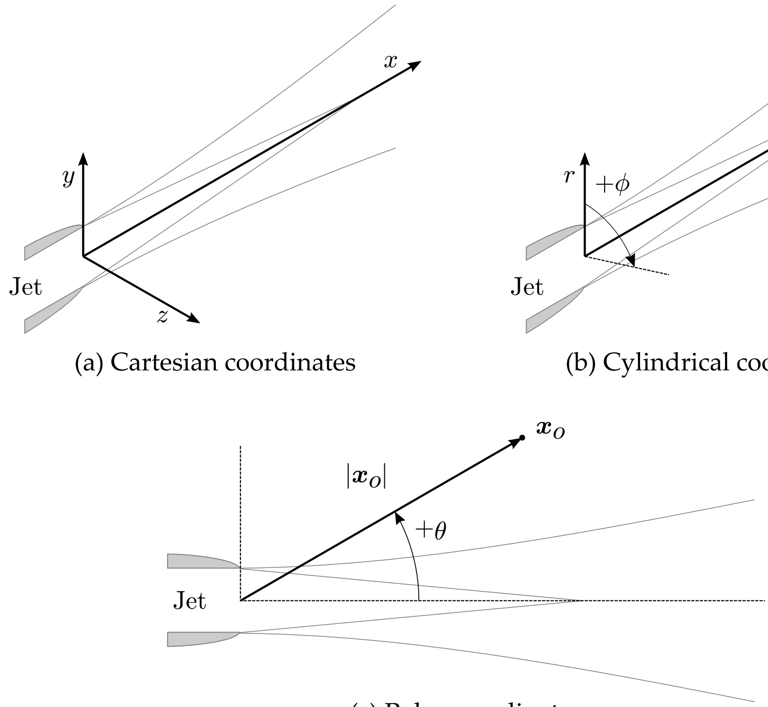

Figure 2.2: Sign conventions for jet noise[4]

transition region exists between the potential core and the fully developed region as the flow transitions to fully developed flow. The transition region is typically the area of greatest turbulence in the flow. The *turbulent mixing region* encompasses all of the flow where turbulent mixing takes place, including the shear layer.

Lighthill (1952) noted the primary term responsible for the amount of noise emitted by a jet is $\rho_0 U^2$, where ρ_0 is the ambient fluid density. However, he also noted the effects of two important non-dimensional parameters, the *Mach number* (M) and the *Reynolds number* (Re). The Mach number ($M = U/c_0$) affects the efficiency of the noise sources, while the Reynolds number—since it represents the dominance of inertial over viscous fluid forces—affects the nature of the sound generation mechanisms. The Reynolds number for a circular jet is given by

$$\mathrm{Re} = \frac{\rho_J U D}{\mu_J}, \tag{2.3}$$

where ρ_J is the fluid density at the jet exit, D is the diameter of the jet, and μ_J is the dynamic viscosity of the fluid at the jet exit. The Reynolds number is important for comparing jets of different sizes and velocities. It is especially useful for comparing

[4]Many experimental studies measure θ from the upstream axis as opposed to the downstream axis, which is the convention in most theoretical studies. The convention used in this thesis is measurement from the downstream axis as indicated.

small model jets to full-scale jets.

The demarcation between the near-field and far-field is not a well-defined physical location. In fact, tests with microphone measurements have shown that the dividing line is frequency dependent. Using the wavenumber[5], k, which characterizes the spatial distribution of the sound waves, and the radial distance from the jet axis, r, Arndt *et al.* (1997) proposed a value of $kr = 2$ for the separation and reported a sharp divide between near-field and far-field behaviour at this location. It is clear that close to the jet, the dominant behaviour is hydrodynamic and far from the jet the dominant behaviour is acoustic. However, in the near field, even though acoustic fluctuations are masked by higher-intensity hydrodynamic fluctuations, they must be present because acoustic fluctuations start in the jet and propagate outward. In contrast to this, only acoustic behaviour is possible far from the jet because the medium is essentially quiescent far from the jet and no non-acoustic stress field associated with the jet can exist.

A further peculiarity of the noise emissions from turbulent jets is that the analysis of the emissions is a story of two different complexities. In the turbulent flow region, the fluctuations satisfy the full non-linear Navier–Stokes equations, numerical solutions of which are now possible in simple cases but not necessarily practical or informative for jet design. In the far field, the pressure fluctuations follow simple linear acoustics equations, which can be easily solved for given boundary conditions (typically a pressure distribution on a surface surrounding the turbulent flow). This reduced complexity of the far field gives hope to researchers that the acoustically important behaviour of jet turbulence can also be captured with a reduced-order model of the jet dynamics (Jordan & Colonius, 2013). This observation forms the basis for the noise source modelling approach pursued in chapter 4.

2.2.4 Origins of jet noise research and the acoustic analogy

The advent of aeroacoustics research was the first part of the pioneering paper of Lighthill (1952), which addressed the production of sound by aerodynamic forces. He released a second part to the paper, which focused on turbulence as a sound source, two years later (Lighthill, 1954). In the first part of the paper, Lighthill introduced what became known as the 'acoustic analogy.' Lighthill's novel idea was to take the Navier–Stokes equations[6], which govern fluid motion, and to rearrange them

[5] $k = 2\pi/\lambda$, where λ is the wavelength of the sound waves.

[6] Although the Navier–Stokes equation is the name of the momentum conservation equation for a fluid flow, the term Navier–Stokes equations typically refers to all three of conservation equations for a fluid flow, balancing mass, momentum, and energy. The energy equation is only necessary when compressibility effects cause significant changes in the internal energy of a fluid element. Lighthill (1952) ignored the energy equation in his initial formulation.

into a general form of the wave equation. In this way, he separated the terms in the equations of motion into those satisfying the wave equation, which represent the observed sound field in a quiescent medium, from all the other terms. All the other terms were collapsed into an externally applied stress field. Setting mass sources and external forces to zero, Lighthill (1952) rearranged the Navier–Stokes equations to obtain[7]

$$\frac{\partial^2 \rho'}{\partial t^2} - c_0^2 \frac{\partial^2 \rho'}{\partial x_i^2} = \frac{\partial^2 T_{ij}}{\partial x_i \partial x_j}, \tag{2.4}$$

where T_{ij} is the instantaneous applied stress at any point. T_{ij} has become known as the Lighthill stress tensor and is given by[8]

$$T_{ij} = \rho u_i u_j + \sigma_{ij} - c_0^2 \rho \delta_{ij}, \tag{2.5}$$

where δ_{ij} is the Kronecker delta function and σ_{ij} is the full stress tensor at the location of the fluid element. Physically, this means that the sound generation and propagation from an arbitrary fluid motion is equivalent to a distribution of appropriate sources. All of these sources are contained in the Lighthill stress tensor. In his own words, Lighthill described T_{ij} in the following way:

> The external stress system T_{ij} incorporates not only the generation of sound, but its convection with the flow (in part of the term $\rho u_i u_j$), its propagation with variable speed and gradual dissipation by conduction (each in part of the difference between pressure variations and c_0^2 times the density variations), and its gradual dissipation by viscosity (in the viscous contribution to the stress system σ_{ij}) (Lighthill, 1952)[9].

In practice, this means that an appropriate model for the Lighthill stress tensor is all that is required to predict the sound field generated by an arbitrary fluid flow. It is important to note that this form of the acoustic analogy contains no approximations; it is exactly equivalent to the original equations of motion. In itself, the analogy is not particularly useful in simplifying the problem of jet noise prediction since calculating the Lighthill stress tensor directly is no easier than solving the original equations of motion; however, the knowledge that the acoustic field of any arbitrary fluid motion is equivalent to a field of appropriate sources is powerful. Lighthill's acoustic analogy

[7]Apart from changing the acoustic variable from p to ρ, the major difference between equation (2.1) and equation (2.4) is the addition of the source term to the right hand side. Aeroacoustics can be defined as the study of flows in which the sound source is this term on the right hand side of equation (2.4) (Hirschberg, 2001).

[8]An alternative formulation for the Lighthill stress tensor can be written in terms of the viscous stress tensor as $T_{ij} = \rho u_i u_j + \delta_{ij}\left(p + \rho c_0^2\right) - \tau_{ij}$.

[9]The notation used in this quotation has been changed slightly from the original paper in order to match the notation used in this work.

provides a starting point for making approximations to the Lighthill stress tensor, which can simplify the problem of jet noise prediction considerably (Hirschberg, 2001).

The first of these approximations was carried out by Lighthill in the same paper. He first argued that the viscosity terms of the stress tensor should be ignored, and he added that for flows at low Mach number ($M = U/c_0$) , where the flow is nearly isothermal, the final term is also largely cancelled by the pressure in the stress tensor. His simplifications led to $T_{ij} \approx \rho_0 u_i u_j$ (Goldstein, 1974). The $\rho u_i u_j$ terms are referred to as the Reynolds stresses, which are considered to be $\rho_0 u_i u_j$ when density fluctuations are neglected. This leads to the conclusion that the Reynolds stresses are the main sources of sound for these flows. Applying this simplification to jets led directly to several scaling laws between observed sound power and characteristics of the jet. The most important of these is the eighth-power scaling law, which states that the observed sound power scales with U^8. This meant that noise could be reduced simply by increasing the diameter of the engine and reducing the jet velocity for the same total thrust output. This improvement was also amplified by the introduction of high-bypass engines. The bypass ratio is the ratio of air flowing into the engine bypassing the engine core to the air flowing through the engine core, so increasing bypass ratio typically increases jet diameter. High-bypass engines not only produce less noise for a given thrust output, but are also more fuel efficient. In fact, high-bypass engines were developed primarily for their fuel efficiency. An additional advantage of high-bypass engines is that the flow bypassing the combustor also partially buffers the more turbulent, sound-producing flow behind the combustor. These advances led to significant jet noise reductions for aircraft since the 1950s (Morris & Viswanathan, 2011). Lighthill's purely theoretical scaling law has been verified experimentally with impressive agreement. It has also led to the development of semi-empirical models to predict jet noise for well-established jet geometries (Self, 2004).

2.2.5 Qualitative properties of jet noise

2.2.5.1 Directivity

Early jet noise measurements quickly indicated that the jet noise emissions were not uniform at all angles of the jet. In fact, Lighthill's original paper argued that the increased sound intensity measured could be accounted for by considering the sources to be moving eddies (Lighthill, 1952). Ffowcs Williams (1963) expanded this idea by modelling the noise sources as acoustic quadrupoles convecting at high speed in the jet. In his work, Ffowcs Williams (1963) used a modified conclusion from Lighthill that the intensity of the sound varied with $|1 - M_c \cos\theta|^{-5}$—where θ is the observation angle from the downstream axis and M_c is the Mach number of the convecting source—to conclude that for very high-speed jets ($M_c > 1$) the sound power scaled with U^3. This result also agreed with many experiments of the time that were indicating that U^8 scaling seemed too high for very high-speed jets. The important result for the directivity suggested by these authors was the direction intensity factor $|1 - M_c \cos\theta|^{-5}$, which gave a basis for understanding the variation of jet noise at different angles. This result became known as 'convective amplification' and is postulated to result from the fact that convection makes cancellation of quadrupole sources less effective, increasing their efficiency (Crighton, 1975). However, evidence for convective amplification is not fully accepted (Crighton, 1975; Morris & Boluriaan, 2004).

Ffowcs Williams (1963) also noted that observed frequencies should be compared at various observer locations only after shifting the sound spectrum by a Doppler factor of $(1 - M_c \cos\theta)$. An important thing to note with these factors, is that for $\theta = 90°$, both the amplification and the Doppler factor are unity. This indicates that for measurements at 90°, no corrections are necessary. For this reason, 90° is often used as the reference point for theoretical models, especially semi-empirical models. These results imply only one source of jet noise, of which the observed directivity is an inherent property. However, the predictions of this method do not always line up with experimental measurements. An additionally compounding factor is that noise directivity relations have also been observed to vary with the frequency of noise considered.

2.2.5.2 Mach number effects

The components of jet noise considered so far can be attributed to the turbulent mixing, a component of jet noise often called *jet mixing noise*. This is the only source of noise for subsonic jets. For supersonic jets, two other sources of jet noise exist (Morris & Viswanathan, 2011). They only occur when the jet is operated under off-design conditions. This is to say that the exit pressure of the nozzle is not equal to the ambient pressure. *Broadband Shock Associated Noise* (BBSAN) is associated with the interactions of turbulent eddies with the shock-cell structure of a non-ideally expanded jet. These interactions cause partially correlated sources. *Screech tones* occur by way of a feedback effect. Eddies forming at the nozzle travel at a certain convection velocity and interact with the shock-cell structure after a corresponding time. This interaction causes a disturbance that travels upstream and causes a new disturbance at the nozzle. This periodic event creates tones at a narrowband frequency. Fisher & Morfey (1982) have described both BBSAN and screech tones in detail. Of these sources, the dominant form of noise depends not only on the Mach number, but also on the frequency and observation direction. In the laboratory, it is possible to isolate the mixing noise even for supersonic jets by operating a converging-diverging nozzle at design conditions. However, this is typically unfeasible in practice. As this work is focused on subsonic jets, only jet mixing noise will be considered.

Apart from these additional noise sources, the Mach number also affects the characteristics of jet mixing noise. Lighthill's original theory led to the result that not only was there more energy in high-speed flows available to be transformed into acoustic energy, but also the conversion became more efficient as the Mach number increased. This helps account for the high exponent in the eighth-power law. The correction introduced by Ffowcs Williams (1963) was related to an assumption that the sources of jet noise were of finite extent, which partly reduced the exponent for his third-power scaling law. For subsonic jets, the main effect of the Mach number is simply this scaling, with only small changes to the shape of the noise spectra. This result is presented, for example, by Viswanathan (2004).

2.2.5.3 Temperature effects

Most jet engines operate at relatively high temperatures due to the combustion of fuel as the power source. For high-bypass engines there is also a large temperature difference between the combustor flow and the bypass flow. Large variations in temperature change the properties of the fluid travelling through the engine and thus have a marked effect on jet noise. Extensive experiments have been carried out to test the effect of temperature on jet noise emissions (Tanna *et al.*, 1975; Viswanathan, 2004). The effect of temperature is not straightforward. The prevailing result is that for low-speed jets, an increased temperature ratio[10] increases noise, while for high-speed jets it decreases noise. The transition between the two regimes has been shown to be close to $M = 0.8$ (Viswanathan, 2004). Viswanathan (2006) proposed a set of scaling laws for which the exponent was a function of temperature ratio. Of course, for an unheated jet ($T_J/T_0 = 1$) at low Mach number, the result was equivalent to Lighthill's eighth-power scaling law. Viswanathan (2004) also noted similarities in the spectral shape of noise emissions for low θ between unheated low subsonic jets and highly heated supersonic jets. However, the full effects of temperature on jet noise are still a subject of intense debate.

2.2.5.4 Sound propagation

Part of the difficulty in understanding where jet noise originates in the jet is associated with the effect of the jet flow on the propagation of sound. In a stagnant medium,

[10]The temperature ratio, T_J/T_0, is the ratio of the jet exit stagnation temperature to the ambient reference temperature.

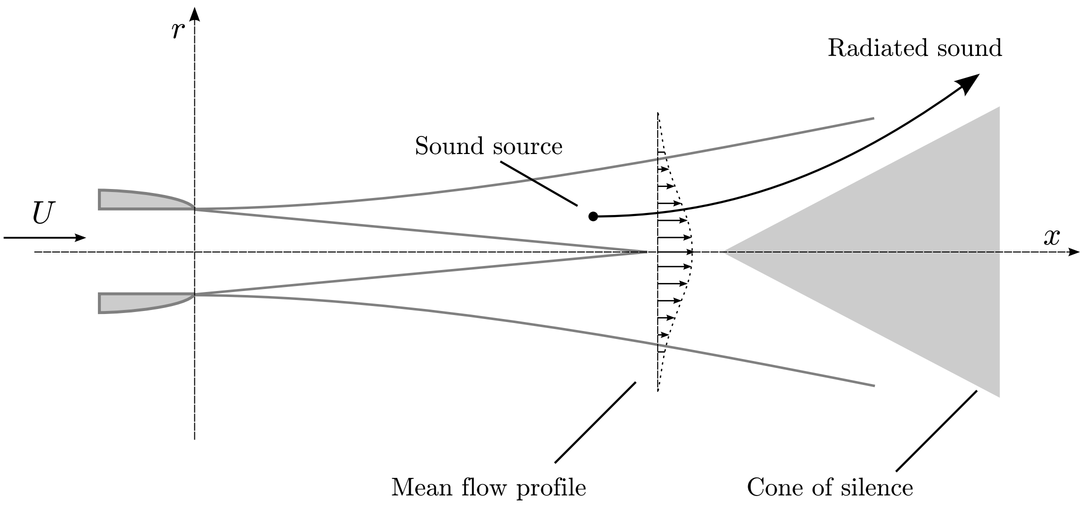

Figure 2.3: Sound propagation through a mean jet flow profile

sound propagates outward evenly in all directions. In a homogeneous two-dimensional mean flow, the difference in velocity—and possibly temperature and density—between adjacent locations causes the sound rays to bend. When the properties of the medium also vary, the sound waves can speed up and slow down according to the local speed of sound, as well as bend and shift according to disturbances in fluid motion. A true prediction of sound propagation in turbulent flow can only be obtained by solving for the turbulent flow field, which is currently impossible for practical flows. Since the sound signals observed from jet noise emissions have fairly constant directionality, there is hope that reasonable estimates of sound propagation can be obtained from mean flow profiles.

The effect of sound refraction in a mean flow is illustrated in figure 2.3. As a wave front propagates in the direction of flow. The velocity difference across the wave front causes the wave to turn outwards. This effect is reversed for wave fronts propagating upstream. This causes a region of reduced sound intensity at emission angles close to the downstream axis known as the *cone of silence*, which is also illustrated in figure 2.3. The reduction in intensity has been observed to be as great as 20 dB by Atvars *et al.* (1966).

Though much of the effect of jet noise propagation can be accounted for by mean flow profiles, the effect of flow fluctuations is still difficult to determine, even in a statistical sense. The complexity of sound propagation in the near-field of the jet makes localization of jet noise sources through acoustic measurements made outside of the jet exceedingly difficult.

2.3 Historical developments in jet noise research

2.3.1 Extended acoustic analogies

Though Lighthill's (1952) acoustic analogy, described by equation (2.4), was the first re-casting of the governing equations of fluid dynamics into a wave equation, it is not the only possible formulation. Acoustic analogies are usually developed in the form

$$\underbrace{L[\rho]}_{\text{Propagation}} = \underbrace{Q}_{\text{Source}}, \tag{2.6}$$

where $L[\cdot]$ is the propagation operator and Q is the source term. In Lighthill's (1952) analogy, the propagation operator is the wave equation in a quiescent medium, and the source is all the other terms in the Navier–Stokes equations. This is the simplest possible formulation for the propagation operator, with the most complicated form for the source term. The benefits of putting more flow physics into the propagation term (left-hand side) is that the source term becomes simpler—making it easier to model—and that the physics of the sound propagation are separated from the physics of the sound generation, allowing a better understanding of what the 'true' source is. However, the disadvantage is the added complexity of solving the equation. While Lighthill's (1952) propagation problem can be solved with a simple free-space Green's function, more complicated forms of the source are not as easy to solve. In the extreme case, where all the physics are placed on the left-hand side, the equations become the same as the Navier–Stokes equations, completely cancelling the advantage of using an acoustic analogy at all.

Lilley (1973) was one of the first to incorporate more flow physics in the propagation term. He incorporated the effect of mean flow refraction (see § 2.2.5.4) into the propagation term by using the Linearized Euler Equations as the wave operator where the equations were linearized about the mean flow of the jet. Lilley's approach was well-received and many subsequent authors expanded on his ideas (Lilley, 1991; Tam, 1998). Over the years, several other variations have been proposed to incorporate various other effects, for example, in Goldstein (2003, 2001) and Phillips (1960). The basic results of these studies have primarily been a greater understanding of jet noise and propagation, but accurate noise predictions based on these techniques that apply to wide ranges of operating conditions and emission directions are still rare (Morris & Viswanathan, 2011).

Since, by definition, all acoustic analogies are exact representations of the Navier–Stokes equations, there is no inherent superiority of one over the other. The strength of each is which flow effects are considered part of the source term and which are part of the propagation term, allowing specific components of the jet noise problem to be considered in each case.

2.3.2 Large-scale and fine-scale noise sources

The earliest understanding of turbulence was as a superposition of uncorrelated random eddies. In the early 1960s, evidence for larger-scale structures began to accumulate. A fuller discussion of the role of large-scale structures in jet noise and the historical developments in their understanding is reserved for chapter 4, in which the role one type of large-scale structure is the focus. However, for the current discussion, it is only necessary to introduce the conceptual separation of large-scale and small-scale turbulence structures.

Unhappy with the poor agreement between the prediction methods of the time, and after analyzing a large experimental database, Tam *et al.* (1996) proposed a division of jet noise into two independent sources. The first source is said to be attributed to the fine-scale structures of the turbulence while the second is associated with the large-scale structures. Corresponding to these sources, Tam *et al.* (1996) introduced two 'similarity spectra,' which are said to be universal for axisymmetric jets. These spectra are termed the Fine-Scale Similarity (FSS) spectrum and the Large-Scale Similarity (LSS) spectrum, respectively. The FSS spectrum seems to characterize the observed emission spectrum of high observer angles ($\theta \gtrsim 80°$) while the LSS spectrum characterizes the spectrum at low observer angles ($\theta \lesssim 40°$, Tam, 1998). Figure 2.4 shows this effect schematically. Despite the compelling experimental evidence for the view proposed by Tam *et al.*, no consensus has been reached as to whether a two-source paradigm of jet noise better reflects the sound generation mechanics than the traditional one-source paradigm.

The shortcoming of the FSS and LSS approach to jet noise prediction is that the scheme lacks predictive power because it is predominantly empirical. Ultimately, the similarity spectra are fitted to experimental data after experimental testing, which means that the model always involves arbitrary constants that are not easy to predict in advance. Also, though the database used by Tam *et al.* (1996) to generate the similarity spectra represents the mechanics of simple circular jets, novel designs that deviate from simple jets cannot necessarily be expected to follow the same trends. The advantage of the approach is the effectiveness with which it explains the seemingly universal characteristics of the noise emissions from circular jets.

Aside from the concerns with the FSS and LSS approach, the identification of large-scale structures as efficient jet noise sources has important ramifications. Again, the details of these ramifications will be discussed in more detail in chapter 4, but one

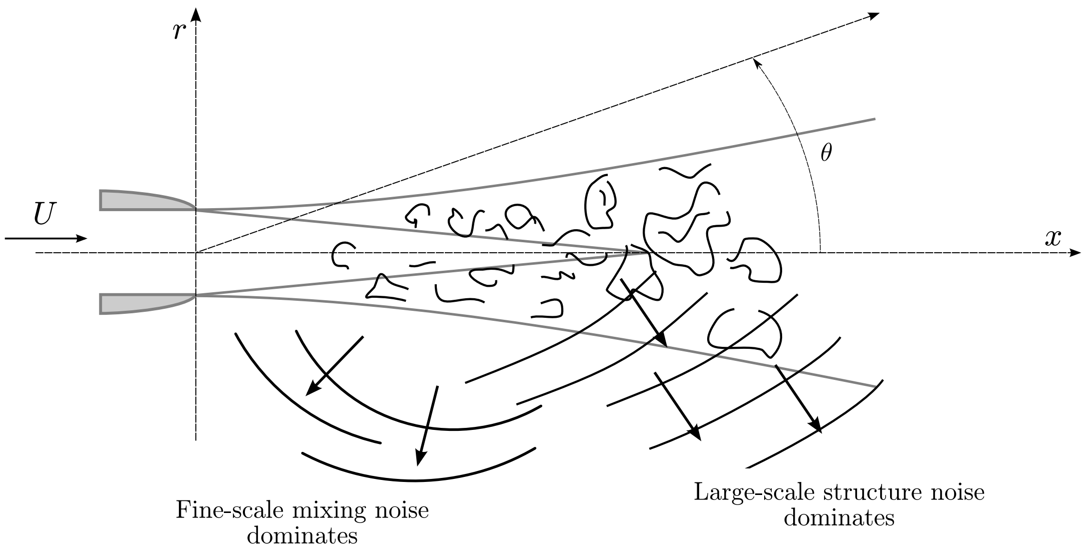

Figure 2.4: Theorized noise components of a jet. Adapted from Tam *et al.* (2008).

important consideration is that significant noise reductions based on noise reduction technologies are more feasible if large-scale structures are the dominant sound source. For example, if the dominant sound source is random turbulent fluctuations evenly distributed everywhere in the jet, the likelihood that a device could be designed to exert significant control authority over all locations at once is quite small. However, if the dominant source is a large fluctuation correlated over a significant portion of the length of the jet, it could more easily be influenced by a device that acts at one specific location, which is a more feasible design goal. Therefore, the discovery of the importance of large-scale structures in jet noise is a promising development in the pursuit of practical jet noise reduction schemes.

2.4 Noise reduction technologies

2.4.1 Introduction

Despite steady progress in the understanding of jet noise in the past several decades, there are only a few techniques that have been introduced that successfully reduce or mitigate jet noise emissions. In fact, recent evaluations of environmental noise around airports indicate that the affected areas are actually increasing, largely because of increased flight movements (European Commission, 2008). Perhaps the biggest challenge hindering the development of jet noise reduction techniques is the lack of an efficient prediction scheme for evaluating new technologies. This lack has forced proposed control schemes into long cycles of model-scale and full-scale testing before knowing even qualitatively if they are effective. Often, schemes that look promising at the model scale may have no effect or even detrimental effects on full-scale jets. Another issue is that while some of these techniques may be effective at one set of flight conditions, at different periods during flight they may have negligible or negative effects. Nevertheless, advances have been made and some examples of the major technologies are discussed here.

There are two main categories for noise reduction technologies: *passive control* and *active control*. Passive control is the traditional approach to jet noise reduction. It utilizes time-invariant design changes, such as fixed flow control devices and jet geometry modifications, which attempt to influence the mean statistics of the turbulence or control the growth of the shear layer, for example. Modern techniques have begun to employ active control, incorporating time-varying influences on the jet flow to target specific flow phenomena, such as those associated with dominant peak frequencies in the jet noise spectrum.

2.4.2 Passive control

The best example of a passive control technique that has led to significant noise reductions is the introduction of the high-bypass turbofan engine described in § 2.2.4. The reduction arises from the decrease in exhaust speed for a given thrust requirement when the jet diameter is increased, which reduces noise according to Lighthill's (1952) eighth-power scaling law. This is a rare example of where aeroacoustic and aerodynamic performance were both improved with a single design change. However, there are both theoretical and practical limits to the possible increase of the diameter of a turbofan engine. Ffowcs Williams & Gordon (1965) noted that as the exhaust speed decreases, an additional source of noise appears, which is normally concealed by jet noise and in addition to other typically observed noise components. Jet engines can also not be made arbitrarily large because of the practical limitations of manufacturing fan and turbine blades of sufficient size and strength.

A second prediction that Lighthill (1962) made was that decreasing the turbulence intensity generally in the jet or shortening the mixing region could lead to reductions in overall jet noise. To this end, a number of passive control techniques have been devised to change the mixing characteristics of the jet. These include mixing devices placed in the exhaust flow (Bridges *et al.*, 2003; Gliebe *et al.*, 1991; Lighthill, 1962), *inverted-flow engines* (Gliebe *et al.*, 1991; Morris & Viswanathan, 2011), and *chevron nozzles* (Bridges & Brown, 2004; Herkes *et al.*, 2006). The most common of these devices is chevron nozzles, which feature chevron-shaped cutouts along the perimeter of the nozzle exit. The benefits of chevrons are that they can increase mixing and decrease the length of the potential core. Most mixing devices result in thrust penalties, which may be a more important design consideration than noise reductions. The effect of chevrons is generally a reduction in low-frequency noise with an accompanying increase in high-frequency noise, but the overall impact is usually positive. The parameters for chevron nozzle design include chevron number, length, penetration, and asymmetry. Parametric testing has been carried out by Bridges & Brown (2004), who concluded that the relationships between these parameters are complex but that trends are apparent. Flight tests have yielded promising results and now Boeing has even included chevrons in the design of its recently released 787 (Herkes *et al.*, 2006). A database of information on the effects of chevrons has been growing (Bridges, 2002; Kennedy, 2010), recording the effect of chevrons on the hydrodynamic field of the jet both from the perspective of flow statistics (Kennedy, 2010) and in a time-resolved full-field manner (Scarano *et al.*, 2010), but aside from the concept of 'enhanced' mixing, their true mechanism of noise reduction is yet to be clearly understood.

Passive control techniques suffer from the inability to respond to different performance requirements at different stages in flight. For example, noise reductions are most important at takeoff when the engines are at full power and regulatory noise limits are in place. At cruise, thrust penalties are more important since there are no ground-based observers affected by the aircraft's noise emissions. Additionally, while mixing devices can often be tuned to reduce noise at some flight conditions, they may actually increase noise at different conditions, limiting their effectiveness.

2.4.3 Active control

Broadly speaking, active control techniques are those that require a power source to operate, and can therefore be activated, deactivated, or modified during aircraft operation. Some passive controllers have active analogues. For example, an alternative to physical nozzle inserts is *fluidic nozzle inserts* (Powers *et al.*, 2013), and an alternative to chevrons is *fluidic chevrons* (also *microjets* or *fluidevrons*; Henderson, 2009; Laurendeau *et al.*, 2008; Martens & Haber, 2008). Both systems seek to reproduce the advantages of their passive counterparts while obtaining the benefits of active control by injecting fluid into the jet stream, affecting the momentum of the mixing region in a similar way to their passive counterparts. The principal advantage of these systems is that they can be deactivated when unnecessary or adjusted for different flight conditions, reducing potential aerodynamic performance penalties when noise reductions are less important.

Additionally, some active controllers allow for unsteady operation, creating the ability to target unsteady phenomenon in the jet. For example, microjets can be operated in pulsed or periodic mode if they are attached to suitable actuators. This allows, for example, forcing of the jet at various frequencies (Maury *et al.*, 2011, 2012), or unsteady forcing caused by steady rotation of a microjet (Kœnig *et al.*, 2011, 2013) either of which can influence the jet noise emissions. Though these types of devices can be tuned to cause noise reductions under certain flight conditions, they are *open-loop controllers*; that is, they do not use feedback from the system to control their operation. The newest generation of development in active jet noise control is currently pursuing the use of *closed-loop controllers*, which use real-time measurements obtained during operation coupled with dynamic models of the jet mechanics to detect and influence 'noisy' structures (Jordan & Colonius, 2013).

In order to implement these types of controllers, it is necessary to have an understanding of the noise source mechanics that can predict both the statistical and time-domain noise emissions. Such a technique is developed in chapter 4 while a time-domain error metric—necessary to implement traditional closed-loop control schemes—is developed in chapter 5.

Non-periodic unsteady forcing suitable for use in closed-loop control can be achieved by employing actuators with a faster response time, such as plasma actuators (Kastner *et al.*, 2006; Samimy *et al.*, 2004). Though closed-loop active control of jet noise may never be feasible on a production aircraft, the insight gained from a successful application in a lab setting would be a boon to the understanding of jet noise sources. Regardless of the effectiveness of a closed-loop control system to reduce the total noise level for regulatory purposes, if a control system coupled with a suitable dynamic exerted significant control authority over the jet noise emissions, it would greatly increase the aeroacoustics community's understanding of jet noise source mechanics.

2.5 Conclusion

Over sixty years after Lighthill (1952) laid the foundations of aeroacoustics, research in the field is as active as ever. Each new development leads to more questions surrounding the nature of jet noise sources and potential techniques to mitigate jet noise emissions.

Since then, the understanding of jet noise sources has slowly but significantly developed. Of the developments contributing to this understanding, the most noteworthy for the current investigation are knowledge of the basic structure of the turbulent jet, the mathematical basis for approximate jet noise predictions, the effects of several experimental parameters, and the importance of large-scale structures. Though this understanding is far from sufficient to fully incorporate jet noise considerations into the aircraft design cycle, many advances have been made, and jets are significantly quieter than they were in the 1950s and 1960s. However, much of this progress has been obtained only indirectly with other jet design innovations (*e.g.* high-bypass engines) or at the expense of large experimental campaigns and many years of testing. Even a technology as simple as chevron nozzles has taken decades to finally be incorporated into production jets, and the contribution of chevrons to noise reductions is moderate.

Today, the aeroacoustics community broadly understands the salient features of jet noise, and many of its characteristics have been well documented. However, modern noise prediction techniques still lack the predictive power necessary to incorporate noise concerns into the aircraft design cycle, and design changes still require significant testing before they can be shown to be beneficial. Practical jet noise reductions are as important as ever because the continued expansion of the airline industry—seeking to connect more people and places around the world—is accompanied by continued growth in community opposition concerned with the negative effects of jet noise.

Building on the foundation set by the researchers of the last six decades, the next stage of jet noise research will require numerous advances contributing to the understanding necessary to incorporate jet noise concerns into the aircraft design cycle, each advance addressing a subset of the subtle features of the jet noise problem. Among the required advances is the development of a more fundamental time-resolved understanding of how jet noise sources appear and develop within the jet and ultimately how their sound propagates. The contribution to this advance pursued in this work is the investigation of the time-resolved dynamics of source structures in subsonic jets. This contribution consists of an analysis of noise source localization in subsonic jets using time-resolved Particle Image Velocimetry (chapter 3), the comparison of large-scale wavepacket structure predictions in the near field of subsonic jets and their propagation to the far field (chapter 4), and the development of a metric for comparing the similarity of two time-domain signals (chapter 5). This work represents another small step along the journey started by Lighthill (1952) over sixty years ago.

Chapter 3

Source analysis using time-resolved Particle Image Velocimetry

3.1 Introduction

Jet noise source localization techniques involving the correlation of in-flow fluctuations to far-field pressures have been used extensively since their introduction by Siddon (1970) and Lee & Ribner (1972). A key advantage of the technique is that the measured cross-correlation can be related analytically to a source term using Lighthill's acoustic analogy (1952; and see § 3.4.1). Early investigations (Lee & Ribner, 1972; Rackl, 1973) relied on intrusive probes such as those used in Hot-Wire Anemometry (HWA, see § 3.2.1) to measure time-resolved velocity fluctuations and microphones to measure the far-field pressure. The advantage of using HWA is the high sample rates that are possible, which can well resolve the time scales of the turbulence. However, HWA provides information at a single point, meaning that large flow fields can only be recorded by traversing the probe and making several recordings, which are only correlated in time statistically. A second drawback is that introducing an intrusive probe into the flow field can also introduce a new source of sound. This source may be weak in comparison to the sound of the flow, but it will be highly correlated to the velocity fluctuations at the velocity probe, which can lead to erroneous correlation measurements (Richarz, 1978). The intrusive aspect of HWA was relieved in the 1970s by the introduction of the Laser Doppler Anemometry (LDA) at the expense of reduced time-resolution and a sample record that is intermittent. Despite early technological gains, correlation measurements were largely set aside until recently, with the introduction of more modern non-intrusive measurement techniques such as molecular Rayleigh scattering (Panda, 2005). The technique has also been carried out in the frequency domain and combined with beamforming for the pressure measurements (Papamoschou *et al.*, 2010) and to data from numerical simulations (Bogey & Bailly, 2007).

The introduction of Particle Image Velocimetry (PIV, see § 3.2.2) for spatially resolved flow measurements has largely revolutionized the acquisition of data from flow experiments (Raffel *et al.*, 2007), allowing large flow fields to be measured simultaneously. Perhaps the bright future for PIV is best indicated by the rapid extension of the technique to fully volumetric, three-component velocity measurements by a variety of techniques (Elsinga *et al.*, 2006; Hinsch, 1995). These techniques have even been applied to transitional jets to consider the development of flow structures (Violato & Scarano, 2011). A fullness of flow information is now available that likely could never have been imagined by early aeroacoustics researchers. Until recently, this extensive spatial information has been obtained at the expense of time-domain resolution with maximum PIV acquisition rates reaching only a few frames per second.

The advent of Digital PIV (Willert & Gharib, 1991) started a rapid escalation toward higher acquisition rates, and recent developments in laser and camera technology have led to the introduction of Time-Resolved PIV (TR-PIV, see § 3.2.3), where the acquisition rate is high enough to temporally resolve the flow field. The acquisition rate necessary to resolve a particular flow is dependent on the time scales of the events to be resolved, and for turbulence, the required acquisition rates are very high. Current equipment in common use is limited to acquisition rates around 10 kHz, while some limited tests have been carried out as high as 25 kHz (Bridges & Wernet, 2007; Wernet, 2007b) with reduced Fields Of View (FOVs). These increased acquisition rates, as well as creative applications of low-speed PIV equipment have led to a number of PIV investigations of aeroacoustic flows (Morris, 2011; Schröder *et al.*, 2004; Seiner, 1998). Despite these high data rates, the discrete nature of PIV measurements introduces the problem of temporal aliasing because the measurement of the flow velocity and the discrete sampling cannot be separated. This is because the PIV algorithm works by comparing two discrete images so there is no continuous signal to which an anti-aliasing filter can be applied. This aliasing of high-frequency information into lower frequencies limits the accuracy of TR-PIV measurements in the frequency domain. This aliasing effect has been noted by previous investigators (Bridges & Wernet, 2007; Wernet, 2007b), although its effect on the determination of the space–time correlation, $R_{u'p'}(\mathbf{x}_s, \mathbf{x}_o, \tau)$, and the frequency-domain equivalents has not been investigated.

The advantage of TR-PIV over traditional PIV for correlation measurements lies not in the calculation of time-domain correlations, but in the ability to record individual flow realizations and calculate frequency-domain statistics. With traditional PIV, it is also possible to resolve the time-domain correlation coefficient between flow fluctuations and far-field pressure at the sampling rate of the far-field microphone, and TR-PIV offers no direct benefits. Traditional PIV has been used by Henning *et al.* (2008, 2010a,b) in a number of flow configurations including a cylinder in cross-flow and a cold jet. This was achieved by coupling 5000 PIV measurements with a long series of high sample rate microphone measurements lasting over 30 minutes. In fact, § 3.5.2 describes how the traditional PIV approach is superior to TR-PIV when considering the contribution of each velocity measurement to the statistical significance of the correlation estimate. However, because correlation is ambiguous in the direction of causation, it is often necessary to observe the full development of a fluctuation in real time to determine how it originated and became an efficient sound emitter. TR-PIV's ability to record individual flow realizations enables a connection to be made between the development of each flow fluctuation and its contribution to the flow statistics, which may not be apparent in the averaged flow development animated by mapping the correlation coefficient. From a control perspective, this translates to a more concrete ability to see what fluid events caused a fluctuation, making it possible to propose schemes to counteract that source activity. The calculation of frequency-domain statistics such as coherence also provides another useful perspective in source analysis. Specifically, the calculation of the coherence is the first step toward the application of multiple input/output source identification analysis (Fitzpatrick & Rice, 1988). Also, since the introduction of TR-PIV-based time-domain sound field prediction techniques (Haigermoser, 2009; Koschatzky *et al.*, 2011), comparison of the correlation and coherence features between the measured flow and the measured and predicted sound fields may yield useful insight. In the present thesis, however, since this work represents the first step toward using TR-PIV-based correlation in these applications, the discussion is limited to the ability of TR-PIV to reproduce the space–time correlation value, $R_{u'p'}(\mathbf{x}_s, \mathbf{x}_o, \tau)$, and the space–frequency coherence, $\gamma^2_{u'p'}(\mathbf{x}_s, \mathbf{x}_o, f)$.

The separation of a turbulent flow into components that are important for sound generation and components that are not has been an elusive goal of jet noise researchers for many years. The earliest understanding of turbulence viewed it as a collection of independent, uncorrelated eddies each producing its own sound field and correlated only over a length comparable to the integral turbulence scale, but a more modern understanding recognizes the importance of coherent structures that may in fact be responsible for many observed jet noise characteristics (Jordan & Gervais, 2007). This development gives hope that a jet flow can be separated into two parts: one consisting of acoustically important fluctuations and the other consisting of acoustically unimportant fluctuations, where the acoustically important part may be considerably simpler than the full flow. The importance of this separation is that the prediction or computation of the full complexity of full scale jet turbulence and its noise generation is unfeasible even with the most modern available resources. The identification of a reduced-order, more easily computable flow skeleton that can still lead to accurate noise predictions is a highly cherished goal in the aeroacoustics community. Although a formal definition of what constitutes acoustically important and acoustically unimportant components has not been agreed on, empirical guidelines have been developed to filter pressure signals measured in the hydrodynamic field into those considered to be related to sound propagation and those associated with the flow hydrodynamics. The implicit assumption in this separation is that signals propagating at the sound speed c_0 (the 'acoustic' component) can be then traced back to the original source location. One such criterion in common use is that of Arndt *et al.* (1997) based on kr where k is the wavenumber, and r is the distance from the centre-line at which the measurements is taken.[1] The criterion predicts that for $kr < 2$, the signals are hydrodynamic and for $kr > 2$ the signals are acoustic. Although this has proved to be a valuable rule of thumb because the strength of the hydrodynamic fluctuations decays rapidly as r increases and this decay is more rapid for higher frequencies, there is no firm connection between the criterion and the behaviour defining acoustic propagation, namely a propagation velocity of c_0.

A separation technique has been developed recently by Grizzi & Camussi (2012) that attempts to make a firmer connection between the propagation velocity criterion and the separation technique by using the propagation velocity (albeit indirectly) in the signal separation. Fuller details of Grizzi & Camussi's (2012) method are given in § 3.4.2. The current work uses this separation technique as a pre-conditioner for the microphone signals to allow the microphone measurements to be taken closer to the flow.

3.2 Velocity measurement principles

3.2.1 Hot-Wire Anemometry (HWA)

The measurement of velocity component in a fluid flow within a jet is exceedingly difficult. Any probe placed in the flow will have an effect on the flow itself. The motivation behind HWA is to have the smallest probe possible, thereby minimizing the effect of the probe on the flow. The HWA probe is made up of a small conducting wire (diameter $\approx 5\ \mu$m, length ≈ 3 mm) that acts as a resistor. A voltage is applied across the wire such that it reaches a set temperature, often higher than 250 °C. When the wire is placed in the flow, forced convection causes the wire to lose heat. The greater the flow velocity, the faster the heat loss. In the most common configuration, the probe is set up

[1] Though Arndt *et al.* (1997) called this term kr, others sometimes use ky since r and y are equivalent in a 2-dimensional coordinate system.

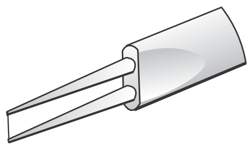

(a) 1-wire probe

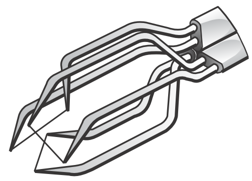

(b) 3-wire probe

Figure 3.1: Hot-wire anemometry probes. Images reproduced from DANTEC-HWA.

for Constant Temperature Anemometry (CTA). The CTA circuit balances the current such that the temperature of the probe remains constant. This is possible because the resistance of the wire is temperature-dependent. The circuit only has to balance the resistance of the probe branch of the circuit. When balancing the resistance, the voltage across the branch changes with the flow velocity. The CTA is then calibrated so that the voltage measurement can be converted to a velocity measurement. A standard probe, such as the one pictured in figure 3.1(a), measures one component of the velocity, but adding additional wires to a probe in different orientations allows the recording of two or three velocity components on different measurement channels. An example of such a multi-wire probe is pictured in figure 3.1(b). However, it is important to note that if only one or two components of a three dimensional flow are measured, the unmeasured components cause an error in the recorded measurements because the extra components can increase convection and cause a bias toward higher values.

For very high-speed flows and for flows in liquids, hot-film anemometers are typically used. These are similar to HWA probes except that the resistor is film deposited on a solid insulator. The solid insulator adds structural integrity to the probe, making the system more resilient.

HWA probes are typically calibrated using a dedicated calibration unit with adjustable flow velocity. Since the relationship between flow velocity and voltage is non-linear, it is necessary to calibrate the velocity in the specific velocity range of interest in an environment that is as close to the experiment environment as possible. A distinct advantage of the hot-wire system is its high frequency response. Laboratory-grade HWA systems are sensitive to fluctuations up to 100 kHz. Since the signal is analogue, it can be filtered and sampled at whatever rates are suitable for analysis without significant aliasing. HWA does suffer from several drawbacks. First, the heat transfer to the fluid is temperature dependent so the temperature of the flow must remain relatively constant and be well known. The temperature can be recorded simultaneously, and the voltage can be corrected if the probe has been calibrated for temperature effects, but when the flow temperature fluctuates rapidly, the uncertainty of the measurements increases. With a single probe, there is also no way to differentiate between a temperature fluctuation and a velocity fluctuation, for high-Mach-number jets and heated jets, where the temperature fluctuations can be large, this is a significant issue. HWA probes are extremely fragile and a broken probe not only must be fixed, but also re-calibrated. A comprehensive introduction to hot-wire anemometry is given by Bruun (1995).

Early experimental studies almost exclusively used HWA for in-flow velocity measurements (Lee & Ribner, 1972; Schaffar, 1979) as it was the only time-resolved velocity measurement technique available. More modern studies still also use them as well, especially for the measurement of cross-correlation length scales useful for noise source models (Kennedy, 2010; Kerhervé & Fitzpatrick, 2010; Morris & Zaman, 2010). However, the significance of the intrusiveness of HWA probes on the jet flow cannot be ignored in aeroacoustics. This is especially true when correlating in-flow velocity measurements to far-field acoustic measurements. As was noted by Richarz (1978), though the noise introduced by the probe may be completely masked in the total jet noise emissions, the induced source is highly coherent with the local perturbations, which will artificially increase correlation measurements. This can easily be imagined by noting that the unsteady forces acting on the hot-wire create an acoustic dipole that is directly linked to changes in the local velocity. This means that the measured acoustic signal will be highly correlated to the artificial sound source introduced by the probe. This fact has driven the development of several non-intrusive velocity measurement techniques Panda (2005). This is particularly important for correlation measurements made between in-flow and far-field microphones.

3.2.2 Particle Image Velocimetry (PIV)

A modern technology for in-flow velocity measurement that does not suffer the same intrusiveness drawback as HWA is PIV[2]. PIV operates by seeding the flow with small particles and illuminating them with laser light. The unique aspect of PIV over more traditional laser-based measurement techniques like LDA is that the PIV technique uses a laser sheet instead of a laser beam, illuminating an entire sheet of particles and then taking an image of the particles illuminated by it, recording spatial information.

[2]A number of acronyms have become associated with PIV and slight variations exist in the literature. As initial PIV methods used film-based image acquisition, early authors associated DPIV (Digital PIV) with the corresponding digital camera-based implementation. As digital cameras have widely replaced film cameras, PIV now more commonly refers to both implementations. LSV (Laser Speckle Velocimetry) refers to the same concept except that the seeding density and particle size are such that individual particles cannot be discerned. PTV (Particle Tracking Velocimetry) is used when the particles are large enough and sparse enough to be tracked individually between images, obviating the need for interrogation windows. LIF (Laser Induced Fluorescence) is the same as PIV except that the laser induces the particles to fluoresce and the re-emitted light is observed, typically filtering out the original laser wavelength.

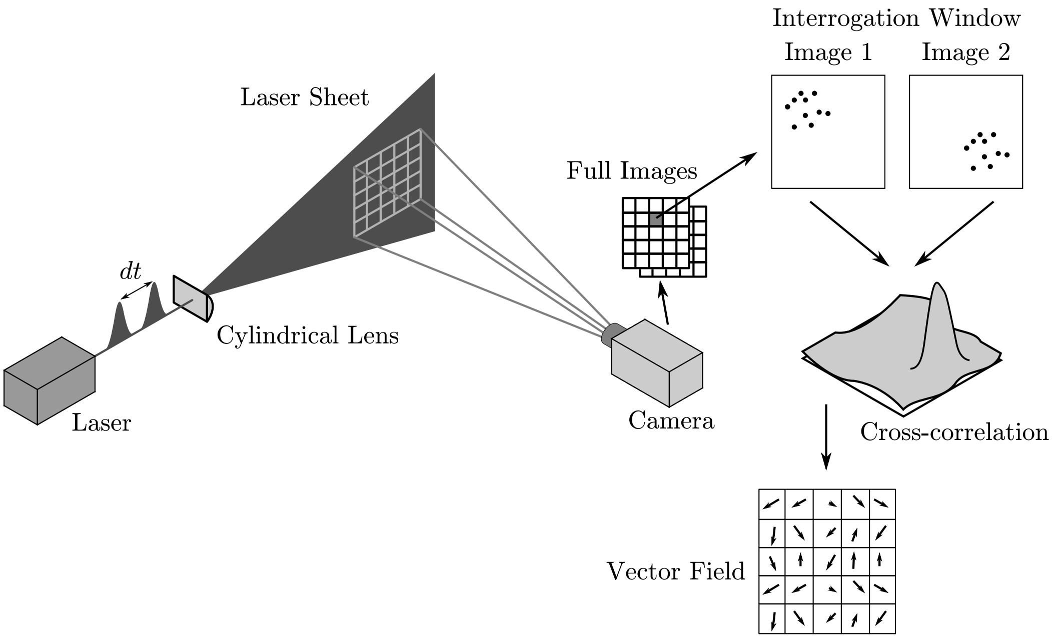

Figure 3.2: Schematic of the Particle Image Velocimetry technique. Image based on DANTEC-PIV.

In order to obtain velocity information, the laser is pulsed twice with a small time step, dt, between the two pulses. The distance between the location of a particle during the first and second pulses (pixel shift) divided by the time step is the local mean flow velocity during the time step. A typical PIV setup showing an outline of the vector field computation procedure is given in figure 3.2. An extensive practical guide to PIV has been prepared by Raffel *et al.* (2007).

The images are usually broken into a grid of interrogation windows of size $N \times N$, where N depends on the specific setup, but common interrogation windows range between 16×16 pixels to 64×64 pixels. Each interrogation window from the first pulse is then correlated to the corresponding correlation window for the second pulse. A PIV system can be operated either in *double-frame* or *single-frame* mode. In single-frame mode, both laser pulses are exposed on a single image frame, and the correlation that is used is an autocorrelation of each frame. One immediate problem with single-frame PIV is that a large peak will exist at zero displacement so it may be difficult to discern peaks that represent small pixel shifts. Secondly, autocorrelation techniques have a directional ambiguity because it is unclear which particle images correspond to each exposure of the frame. Thus either *a priori* knowledge of the flow direction is required or complex mechanical tools can be used (Raffel *et al.*, 2007). A more effective approach is to use double-frame mode where each laser pulse is exposed on a separate frame and the frames are cross-correlated. In double-frame mode, both the high peak at zero displacement and the directional ambiguity are removed. The double-frame technique does double the amount of memory required to store each time step and can thereby decrease the maximum recording rate. However, double-frame PIV has quickly become the standard PIV technique and most modern systems are packaged with cameras that are capable of shooting image pairs with small time steps. PIV lasers typically contain two separate cells for allowing dt to be shorter than the time required to recharge one cell for a second pulse.

In order for the correlation to work, the dt value must be set so that most of the particles do not leave the interrogation window between the two frames, otherwise no peak will exist. It has been shown by Willert & Gharib (1991) that setting dt such that particles travelling at the mean flow velocity shift $N/3$ pixels between frames optimizes the signal-to-noise ratio. However, the more conservative $N/4$ rule, or *one-quarter rule* (Keane & Adrian, 1990), has become widely accepted.

The original PIV correlation algorithm yields only integer pixel displacements, which cannot resolve the continuum of velocities present in real flows. In response to this, peak-fitting algorithms are used that fit a suitable analytical curve (often a 3-point Gaussian) to the points of the correlation values and then calculate the location of the curve peak from the analytical equation. This increases velocity resolution considerably. A residual effect of the integer pixel sensitivity called *peak locking* remains after this process. Peak locking refers to a bias error toward integer values for each calculated component of the vector displacements (Willert & Gharib, 1991). The magnitude of this error mainly depends on how large the particles appear on the sensor. It can be greatly reduced by ensuring the particles have a mean diameter slightly larger than the pixel size. Under certain circumstances, using different peak-fitting schemes can also improve results. The typical way to detect peak locking is to plot the data as a histogram of displacement components and ensure there are not peaks near the integer displacement values. Recent analysis by Nogueira *et al.* (2011), however, has shown that this is not always a sufficient criterion and that peak locking can in fact operate either toward or away from integer values. The authors suggest peak locking can have a more pronounced effect than anticipated, especially when comparing RMS quantities. The effect is not necessarily readily apparent and a careful approach must be used. Despite this difficulty, careful acquisition of the data followed by scrutinization of the PIV statistics—especially comparison to other measurement techniques—allows PIV data to be interpreted with confidence.

Various algorithms are commonly applied to increase the quality of PIV results including multi-pass interrogation, grid refinement, and image deformation. Full descriptions of the these algorithms and the concerns associated with each one are given by Raffel *et al.* (2007). Post-processing techniques and data validation are also important considerations discussed extensively by Raffel *et al.* (2007).

The main advantage to PIV measurements is that they provide spatially resolved velocity information. PIV can take simultaneous measurements at a large number of locations, which would either not be possible or not feasible with traditional equipment. Entire flow fields can now be visualized with this technique, greatly expanding the available analysis for data. The spatial data also allows the approximate calculation of higher-order quantities such as vorticity, circulation, and shear stresses, which allow for higher level analysis. These values are especially relevant in aerodynamic applications. Because of this, PIV has rapidly become a dominant method for flow measurement in industry. As with LDA, the system is non-intrusive, but visual access to the flow is still required. PIV systems can be very expensive, but prices have dropped steadily in recent years. The system setup is also more complicated than in HWA or LDA.

3.2.3 Time-Resolved PIV (TR-PIV)

Fundamentally, TR-PIV is the same procedure as PIV. The only difference is that the acquisition rate—defined by the delay between each subsequent image pair—is high enough to at least partly resolve the flow fluctuations in time. The definition of 'time resolved' in turbulence measurements is not straightforward, which is why some investigators prefer the term High-Speed PIV (HS-PIV). For a flow phenomenon such as vortex shedding that occurs in a narrow part of the frequency spectrum, it is possible to claim that the flow is time resolved when the Nyquist frequency of the acquisition is well above that of the flow phenomenon, but turbulence is a broadband phenomenon with a slow energy decay up to very high frequencies, making claims that the turbulence is time resolved dubious. However, in a more general sense, a flow can be considered time resolved when the acquisitions are not statistically independent, allowing analysis in the frequency domain. That is the sense in which 'time resolved' is used in this work. Determining the cut-off at which this frequency-domain analysis becomes invalid (*i.e.* the time resolution limit) is one of the key objectives of this study.

There are several limitations to implementing TR-PIV systems. For example, as the repetition rate of the laser equipment increases, the available laser power decreases considerably, reducing the signal-to-noise ratio of the system because the particles are not as clearly illuminated in the images. Also, TR-PIV measurements often acquire tens of thousands of frames in a number of seconds, requiring large amounts of computer memory and very fast storage media. Over time, especially in the last decade, as camera and laser technology has advanced, these limitations have become much less restrictive, finally making TR-PIV a feasible (and popular) technique. Recent applications of TR-PIV to jet noise have performed double-frame PIV at repetition rates of 10 kHz (Wernet, 2007a), with at least one study performing a limited number of tests at 25 kHz (Bridges & Wernet, 2007; Wernet, 2007b). These values are starting to approach the traditional sample rates of analogue techniques such as HWA and the mean data rate of LDA systems.

The other issue affecting TR-PIV measurements is the relationship between spatial resolution and temporal resolution. Since high-frequency fluctuations occur on very small length scales, they may not be detectable on a TR-PIV recording even if the acquisition rate is high enough. A separate issue is the spatial averaging caused by the finite size dimensions of the interrogation window. This effect filters high-frequency fluctuations in the signal. In convecting flows, the filter has been described by Henning & Ehrenfried (2008) in terms of the interrogation window size in the convection direction, $W_{x,\mathrm{PIV}}$, as $\mathrm{sinc}^2(\pi f W_{x,\mathrm{PIV}}/U)$. In such cases, the effect can be removed directly by applying the inverse of the filter.

3.3 Motivation for current experiments

The end aim of this work is to apply the direct correlation technique with TR-PIV to a free jet setup, but the poorly understood nature of sound sources in a jet, which are broadband and distributed, make it difficult to determine the performance of the technique and how the limitations of TR-PIV affect the results. It was therefore necessary to use a baseline test case to first judge the method before deriving firm conclusions from the jet measurements. To this end, a baseline case consisting of a tandem cylinder configuration in a cross-flow was first investigated. This setup was chosen because the tandem cylinders create a narrowband, tonal sound source that remains fixed in a known location in the flow. These factors make the judgment of the performance of the technique more feasible.

For correlation measurements in the time domain, the primary difference between tonal and broadband sources is that tonal sources have a broad cross-correlation signature, and many periods of the signal will appear in the space–time cross-correlation plot with a slowly decaying envelope, while broadband sources will have a more distinct, temporally localized signature at the time lag corresponding to sound propagation. However, in the frequency domain, the opposite is true. Tonal sources have a distinct peak in their spectra, and their similarity to an observer signal can be compared directly by calculating the coherence at that frequency. On the other hand, broadband sources appear distributed across the spectrum, and coherence is more difficult to interpret. The performance metric used here for the TR-PIV is a comparison to correlations and their frequency-domain equivalents measured with traditional HWA. Despite the concerns raised by Richarz (1978) noted in § 3.1 that HWA probes can corrupt noise source measurements by their introduction of a sound source in the flow, this effect will be minimal in the cylinder test case because the cylinder sound source has a strong tonal frequency that will be quite different from any flow resonance of the HWA. For example, in the current experiment the tandem cylinder resonance peak was measured at 1.9 kHz while the two likely hot-wire resonances would be the probe support and the mounting tube, which—based on a resonance Strouhal number for a cylinder of 0.2—would be expected to be $\approx$ 17 kHz and $\approx$ 2.8 kHz, respectively. While the 2.8 kHz value could have been more problematic for the jet case, the results in § 3.6.3 do not show any indication of a spurious peak.

The analysis method consists of two parts: a pre-conditioning of the pressure signals by the wavelet separation technique of Grizzi & Camussi (2012) and the application of the direct correlation. In a facility with anechoic treatment and low background noise, the wavelet separation technique would be unnecessary for these tests because the hydrodynamic component of the fluctuations could be eliminated by placing the microphones in the far-field. Since the total noise output for this relatively low-speed jet is small and the background noise is relatively high, it was better to keep the microphones close to the jet where the signals (both hydrodynamic and acoustic) are stronger.

It will be shown in § 3.6.3 that the results from the free jet test case indicated an extended, convecting source signature, which motivated a simple simulation based on an analytical wavepacket source.

3.4 Theory

3.4.1 Direct correlation technique

The direct correlation technique seeks to quantify a relationship between the velocity fluctuations in a flow (the 'cause') and the observed pressure outside of the flow (the 'effect'). Lee & Ribner's (1972) approach started with the acoustic analogy of Lighthill (1952), which describes the far-field sound emissions of a jet flow as a volume integral of a stress tensor T_{ij} (now called the Lighthill stress tensor):

$$p'(\mathbf{x}_o, t) = \frac{1}{4\pi} \int \frac{1}{|\mathbf{x}_o - \mathbf{x}_s|} \frac{\partial^2 T_{ij}(\mathbf{x}_s, t - |\mathbf{x}_o - \mathbf{x}_s|/c_0)}{\partial x_i \partial x_j} d\mathbf{x}_s, \tag{3.1}$$

where p' is the fluctuating component of the pressure; c_0 is the ambient sound speed; and $\mathbf{x}_s$ and $\mathbf{x}_o$ are the positions of the source and observer, respectively. Lighthill's (1952) assumptions for an incompressible, isothermal jet allow the tensor components to be simplified to $T_{ij} = \rho_0 u_i u_j$, where ρ_0 is the ambient fluid density. Lee

& Ribner (1972) then applied the simplification of Proudman (1952), which reduces this tensor to a single term $\rho_0 u_r u_r$, where u_r is the fluid velocity component in the direction of the observer. Since the observation is in the far field, the $1/|\mathbf{x}_o - \mathbf{x}_s|$ term can be moved outside the integral by assuming a compact source region, and the spatial differentiation can be converted to a time differentiation by a multipole expansion. Multiplying the simplified integral by p' allows the autocorrelation of the far-field pressure to be written as

$$R_{p'p'}(\mathbf{x}_s, \tau) = \frac{\rho_0}{4\pi c_0^2 |\mathbf{x}_o - \mathbf{x}_s|} \int \frac{\partial}{\partial \tau^2} R_{u_r u_r;p'}(\mathbf{x}_s, \mathbf{x}_o, \tau) d\mathbf{x}_s, \tag{3.2}$$

where[3]

$$R_{u_r u_r;p'}(\mathbf{x}_s, \mathbf{x}_o, \tau) = \langle u_r u_r(\mathbf{x}_s, t - |\mathbf{x}_o - \mathbf{x}_s|/c_0 + \tau) p'(\mathbf{x}_o, t) \rangle, \tag{3.3}$$

$\langle \cdot \rangle$ is the ensemble average, and $R_{ab}(\tau)$ is the cross-correlation function with time lag τ between two arbitrary time series a and b. In the frequency domain $R_{p'p'}$ is the power spectrum, which fully characterizes the far-field pressure statistically. This shows that the importance of equation (3.2) is that high correlation between velocity fluctuations in the jet and the far-field pressure are connected by more than just conjecture, which is the basis for most 'black box' applications of correlation methods to system analysis. There is a physical link between the velocity and the far-field sound. Lee & Ribner (1972) used a further breakdown of the source term by invoking $u_r = \overline{u}_r + u'_r$, showing that the source can be divided into two parts, one corresponding to linear velocity fluctuations (u'_r) termed 'shear noise', and the second corresponding to quadratic fluctuations ($u'_r u'_r$) termed 'self noise':

$$R_{u_r u_r;p'}(\mathbf{x}_s, \mathbf{x}_o, \tau) = \underbrace{2\overline{u}_r R_{u'_r;p'}(\mathbf{x}_s, \mathbf{x}_o, \tau)}_{\text{Shear noise}} + \underbrace{R_{u'_r u'_r;p'}(\mathbf{x}_s, \mathbf{x}_o, \tau)}_{\text{Self noise}}. \tag{3.4}$$

The conclusion of this formulation is that mapping regions of high correlation between any of the 'source' terms and the observed pressure is equivalent to mapping the sources for a particular observation location. A final caveat will be well known to those familiar with Lighthill's (1952) analogy. Though the analogy is an exact result for the flow equations, the effects of both sound generation and propagation are embedded in the $R_{u_r u_r;p'}$ term and interpretation of sources is not as straightforward as finding correlation peaks, but rather the source signature should be evaluated in the context of an appropriate idea of what a suspected source is. Further, the maximum correlation should be observed when the time lag, τ, is equal to propagation time of sound from the source location to the observer location, or rather that the retarded

[3]The semi-colon indicates that $u_r u_r$ is taken as a single quantity and correlated to p'.

time, $\tau_r = \tau - |\mathbf{x}_o - \mathbf{x}_s|/c_0 = 0$. This result assumes that the flow is quiescent and that the sources are compact (Lighthill's assumptions, 1952). Because the propagation paths of the sound will be slightly refracted by the mean flow, a small deviation in the peak location should be expected, but considerable deviations would indicate other factors are at work.

This investigation will focus on the shear noise component, $R_{u_r'p'}$, which has been observed to dominate low-angle emissions (Schaffar, 1979). The results presented in this work will be for the simplified term $R_{u'p'}$ based on the axial velocity fluctuation. This simplification was based on several considerations. First, historical measurements of the fluctuations on the centre-line showed that the turbulence intensity of the axial fluctuations is more than 60% higher throughout the jet (see appendix A.1). Second, u and v are strongly correlated by the continuity equation, further reducing the need to include both. And since the observations were taken at a low downstream angle, u_r is also weighted toward u for most of the measurement zone. Ultimately, both $R_{u'p'}$ and $R_{u_r'p'}$ were computed and gave nearly identical correlation traces, but $R_{u_r'p'}$ gave a slightly noisier signal. The reason for this is likely that the v' signal is noisier because the PIV window displacements were optimized for the axial flow component.

The correlation function, $R_{u'p'}$, is typically normalized by the energy of both u' and p' and called the correlation coefficient, $R_{u'p'}/\sigma_{u'}\sigma_{p'}$, where σ is the root-mean-square (RMS) of the data series. For discrete data series at two different acquisition rates, such as the case in this investigation, it is necessary to write the correlation as (Chatellier & Fitzpatrick, 2005)

$$R_{u'p'}(\mathbf{x}_s, \mathbf{x}_o, k\Delta\tau) \approx R_{u'p'}[\mathbf{x}_s, \mathbf{x}_o, k] = \frac{1}{N}\sum_{n=1}^{N} u'[n]p'\left[\frac{f_{s,p}}{f_{s,u}}n + k\right], \tag{3.5}$$

where the ratio between between the pressure sample rate and the velocity sample rate, $f_{s,p}/f_{s,u}$, must have an integer value. The time resolution of the correlation comes from the higher data rate signal, while the number of ensembles averaged for each time lag (N), which influences the signal-to-noise ratio, comes from the lower rate signal. For a maximum contribution of each acquisition to the significance of the $R_{u'p'}$ estimate, each data point must be statistically independent, which will not be the case for TR-PIV (see § 3.5.2 for more detail). The frequency-domain equivalent to the cross-correlation coefficient is the coherence, which is defined as

$$\gamma^2_{u'p'}(f) = \frac{|G_{u'p'}(f)|^2}{G_{u'u'}(f)G_{p'p'}(f)}, \tag{3.6}$$

where $G_{u'p'}(f)$ is the cross-spectral density between u' and p', and $G_{u'u'}(f)$ and $G_{p'p'}(f)$ are the autospectral densities of u' and p', respectively.

3.4.2 Wavelet-based pressure signal separation

A technique proposed recently by Grizzi & Camussi (2012) uses wavelets to separate pressure measurements taken in the near field into hydrodynamic and acoustic components. Full details are presented in their paper, but a brief description is included here. Earlier attempts to separate the two components have been based on the wavenumber parameter of Arndt *et al.* (1997, see § 2.2.3), which has been established empirically. In practice, for measurements at a given location, this implies that all information above a specified frequency is acoustic and all information below that frequency is hydrodynamic. However, this approach does not allow for analysis of the potential sources across the frequency range of the flow. The method of Grizzi & Camussi's (2012) is an extension of the wavelet de-noising technique used by Ruppert-Felsot *et al.* (2009). In this, the signal is filtered into a 'coherent' and an 'incoherent' part based on the magnitude of the wavelet coefficients of a Discrete Wavelet Transform being above a certain threshold. The refinement of Grizzi & Camussi (2012) is that the threshold level, having been estimated by the method of Ruppert-Felsot *et al.* (2009), is incremented and determined iteratively while monitoring several convergence criteria. These criteria are (a) the correlation peak of the hydrodynamic signal must correspond to a propagation velocity less than or equal to the flow velocity, (b) the correlation peak of the acoustic signal must correspond to a propagation velocity greater than or equal to the ambient sound speed, and (c) the peak ratio between the first and second peak of the hydrodynamic signal must be greater than a prescribed value representative of the signal to noise ratio.

The validity of wavelets to separate the two behaviours is not certain *a priori*. However, the unique aspect of this technique is that in addition to a simple wavelet coefficient threshold for the separation, the apparent propagation velocity of the resulting signals is used in the separation criteria. This is important because acoustic behaviour in a flow, as considered in § 3.1, can be defined based on the propagation velocity. Therefore a technique that incorporates this convection property in the separation seems to be the best separation method currently available. Of course, the true validity can only be affirmed if the signals exhibit behaviours that correspond to those expected for each component, which is true for the results presented by Grizzi & Camussi (2012). Particularly interesting is their observation of the 'cone of silence' in the low emission angles of the near field. These results lend support to the validity of the use of this separation technique in these tests. Also, since the acoustic fluctuations decay with observation distance, this separation technique should allow higher signal-to-noise ratios because acoustic measurements can be taken closer to the jet. This is particularly important when testing subsonic jets that have low overall noise emissions.

The technique, however, does suffer drawbacks. The first of these being that it becomes less efficient when the energies of the acoustic and hydrodynamic fluctuations are similar in magnitude so that the threshold does not necessarily clearly separate the two behaviours. The second is that the technique becomes inefficient as the speed of the jet approaches or exceeds the sound speed. When this occurs, there is no clear distinction between the acoustic propagation speed and the hydrodynamic convection speed, which makes separating the two behaviours difficult. For the current setup, neither of these drawbacks poses a significant problem.

3.5 Experimental setup

3.5.1 Test facility

The experiment consisted of two setups with a base flow provided by a free jet facility consisting of a 5.5 kW centrifugal blower attached to a settling chamber and jet nozzle. This facility has been previously qualified and described by Chatellier & Fitzpatrick (2005) and Kerhervé *et al.* (2010). In the first setup, a tandem cylinder pair was inserted into the jet flow as a stationary, high-volume sound source. The purpose of this was to test the technique with a relatively simple sound source distribution. The second setup applies the same technique to a standard free jet. A full schematic of each setup is provided in figure 3.3. The diameter of the jet, D, was 50.8 mm while the diameters of the cylinders, D_{Cyl}, were both 6 mm. The centre of the second cylinder was used as the coordinate reference and located at $1.46D$ from the nozzle lip. In both cases, the jet was operated at $U = 85$ m/s. The measurements were carried out at a number of relevant Areas Of Interest (AOIs). For the cylinders, this was one AOI around the cylinders, and a second in their wake. For the jet, AOIs with a 5 mm overlap extended from the nozzle lip to $6.6D$, extending beyond the end of the potential core, which ended at $5.5D$. The microphones were located at $x = 3.54D, y = 2.5D$ for the tandem cylinders and $x = 7D, y = 4D$ for the jet. In both cases, the centre-to-centre separation distance of the microphone sensing elements was 21 mm, and the microphones were inclined at an angle of 10°. The dominant vortex shedding frequency of the tandem cylinder pair was 1.9 kHz, which was considered to be well-resolved by the TR-PIV measurements obtained at 7.5 kHz. The TR-PIV for the free jet case was obtained at 9 kHz. 9 kHz was chosen over the 10 kHz allowed by the laser to give a slightly larger AOI based on the framing rate limit of the camera. This rate was considered sufficient to resolve the main instability of the jet (close to 1000 Hz), but was not expected to fully resolve the high-frequency decay of broadband jet turbulence. Discovering the effect

Table 3.1: Summary of experimental parameters

Tandem cylinders	Free jet
$D_{\mathrm{Cyl}} = 6$ mm	$D = 50.8$ mm
$(x, y)_{\mathrm{Mic}} = (3.54, 2.5)D$	$(x, y)_{\mathrm{Mic}} = (7, 4)D$
$f_{s,\mathrm{PIV}} = 7.5$ kHz	$f_{s,\mathrm{PIV}} = 9$ kHz
$\mathrm{Re} = 3.5 \times 10^4$	$\mathrm{Re} = 2.9 \times 10^5$
$f_{\mathrm{Peak}} = 1.9$ kHz	–
$N_{\mathrm{Images}} = 12\,148$	$N_{\mathrm{Images}} = 10\,914$
$f_{s,\mathrm{Mic}} = 30$ kHz	$f_{s,\mathrm{Mic}} = 27$ kHz
$U = 85$ m/s	
$f_{s,\mathrm{HW}} = 30$ kHz	
PIV window size $= W_{x,\mathrm{PIV}} = W_{y,\mathrm{PIV}} = 2.2$ mm	
PIV vector spacing $= \Delta x_{\mathrm{PIV}} = \Delta y_{\mathrm{PIV}} = 1.1$ mm	

of this time resolution limitation was one of the aims of the current investigation. The Reynolds numbers of the cylinders based on cylinder diameter and the jet based on jet diameter were 3.5×10^4 and 2.9×10^5, respectively. These parameters are summarized in table 3.1. The lip-line turbulence characteristics of this jet have already been studied extensively (Kennedy, 2010; Kennedy & Fitzpatrick, 2010), and a presentation of the jet flow profile and space–time correlations for this jet facility is also available (Kerhervé *et al.*, 2010). A brief comparison between these historical data and the current TR-PIV and HWA measurements is also given in appendix A.1.

The TR-PIV system employed for these tests included a Quantronix Darwin Duo (15 mJ/pulse @ 1 kHz) dual-cavity laser capable of repetition rates of up to 10 kHz per oscillator. A LaVision HighSpeedStar 6 camera with 8 GB of on-board memory capable of 5400 fps at full frame (1024 px $\times$ 1024 px). PIV processing was carried out using LaVision DaVis 7.2 software using a multi-pass approach with a final window size of 32 $\times$ 32 pixels and 50% overlap. This gave a final vector spacing of $\approx$ 1.1 mm for both tests. The evaluation also used a 3-point Gaussian peak fit and the window deformation technique (Raffel *et al.*, 2007). To obtain a higher framing rate, it was necessary to reduce the FOV as indicated in figure 3.3. The camera memory allowed the storage of 12 148 image pairs per AOI for the cylinder case (test duration $\approx$ 1.6 s) and 10 914 image pairs for the jet (test duration $\approx$ 1.2 s). Oil-based seeding was provided by a Pea Soup PS31ST smoke machine with a nominal particle diameter of 0.25 μm. This small particle size ensured good tracking of the fluid motion but it meant that the particle image size, limited by optical diffraction effects, was approximately 0.3 pixels. Despite the small particle image size, no significant peak locking (see § 3.2.2)

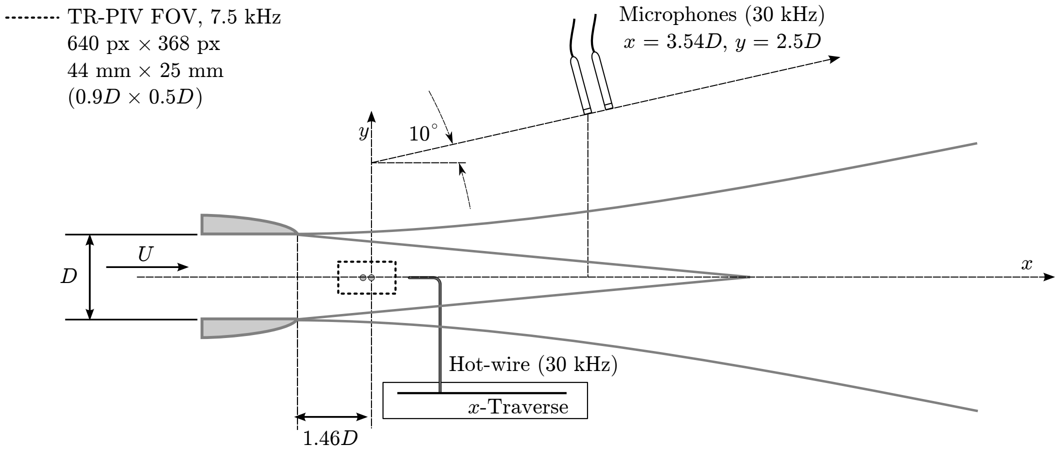

(a) Tandem cylinder pair setup

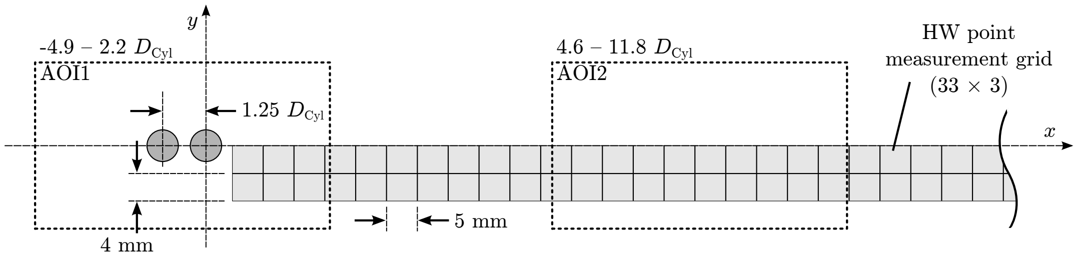

(b) Close-up of tandem cylinder pair velocity measurements

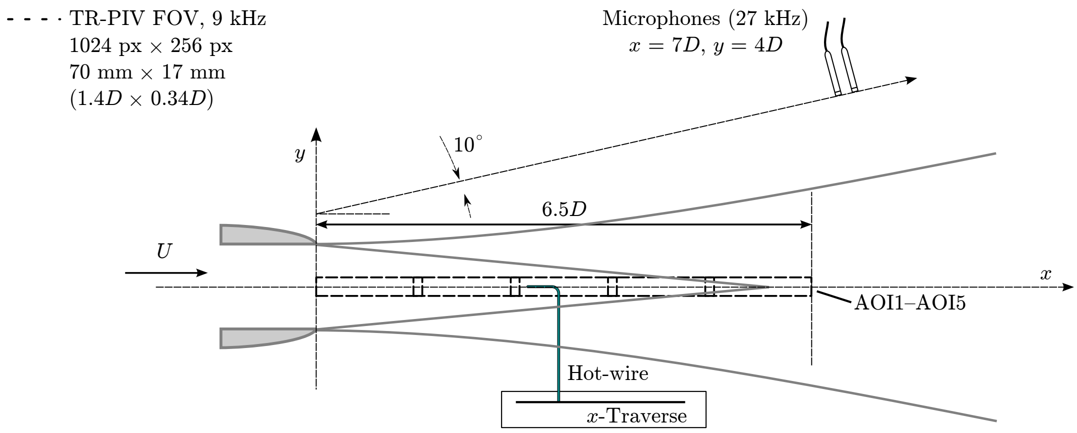

(c) Free jet flow measurements

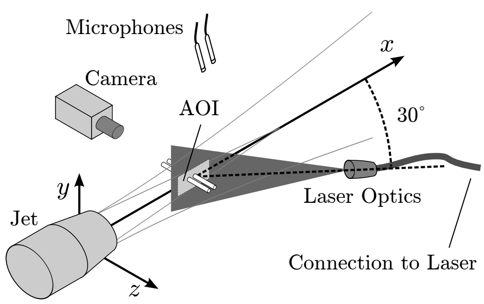

(d) Overall tandem cylinder PIV arrangement

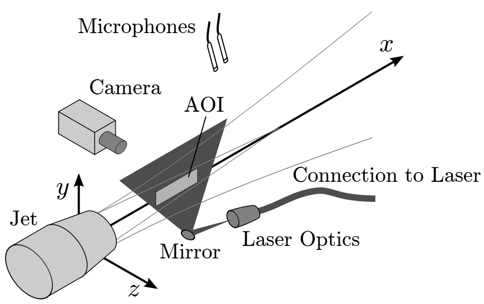

(e) Overall free jet PIV arrangement

Figure 3.3: Experimental setup

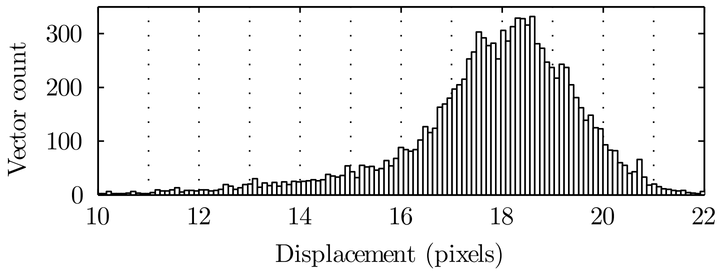

Figure 3.4: Example u signal histogram at $y = 0D, x = 5.5D$

was detected in the resulting velocity signals. This is clear from figure 3.4, which shows an example histogram of the axial velocity component on the jet centre-line at the end of the potential core at 5.5D, and from the close agreement between the RMS values with the historical data presented in appendix A.1. The seeding was primarily introduced at the blower intake, but to ensure adequate seeding in the entrained fluid, the tests were performed only after the entire test facility was filled with smoke.

The microphone system used GRAS components including two 1/4" 40BH microphones connected to 26AC preamplifiers and a 12AN power module. These microphones have a flat (±2dB) frequency response from 10 Hz to 20 kHz. The HWA measurements were made with a Dantec 90C10 constant temperature anemometry module using a single-component probe (type 55P11) oriented so that it measured the axial component of the flow velocity. The analogue signals were sampled with LabVIEW software using an NI PXI-4472B card, which has built-in anti-aliasing filters set to a cut-off of 0.48 f_s. Synchronization between the PIV system and analogue DAQ system was achieved by using a common trigger signal provided by an external source; however, each system had its own system clock. Over the short acquisition time, clock drift was considered insignificant, but it was necessary to check for consistency in the absolute time lag between the first data point for each system. The maximum absolute lag between systems was then $1/f_{s,\mathrm{PIV}}$, but the maximum relative lag between AOIs could be reduced to $1/f_{s,\mathrm{Mic}}$ by comparing the correlation peak lag between subsequent AOIs and adding an integer multiple of $1/f_{s,\mathrm{Mic}}$, where the integer is limited to $f_{s,\mathrm{Mic}}/f_{s,\mathrm{PIV}} - 1$. The microphone signals were sampled at $f_{s,\mathrm{Mic}} = 30$ kHz for the tandem cylinders and $f_{s,\mathrm{Mic}} = 27$ kHz for the jet case, while all HWA measurements were sampled at $f_{s,\mathrm{HWA}} = 30$ kHz. The duration of the HWA measurements was also increased to 10 s giving better statistics. The HWA measurements in the free jet test were made from 2 – 4D in increments of 0.2D as a means to compare the PIV results with the HWA. This span was limited by the length of the traverse used to move the HWA. The PIV and HWA measurements were not carried out simultaneously.

To reduce random noise, outlier PIV vectors that deviated more than 3σ from the mean of the time series at each location were replaced with values spatially interpolated from the neighbouring points. Typically, fewer than 0.5% of the vectors were replaced. The cross-correlations and power spectra were obtained using blocks of 256 points with 25% overlap, yielding 63 averages for the cylinder case and 56 for the free jet. According to equation (3.5), each block of 256 PIV acquisition rate points corresponded to 1024 and 768 points for the tandem cylinder and free jet cases, respectively. The corresponding frequency resolutions for the two cases were 30 Hz, and 35 Hz, respectively. For the HWA measurements, using 1024 points gave the same 30 Hz frequency resolution as the tandem cylinder case and the longer sample time allowed 340 averages in both cases. In the presented spectra and coherences, two iterations of 3-point Hanning smoothing were also applied. No smoothing was performed on the cross-correlations.

3.5.2 Experimental limitations and error

A main disadvantage of TR-PIV over traditional PIV for correlation statistics is the reduced number of statistically independent samples. Each low-speed PIV image pair will be a separate realization of the flow, allowing the greatest contribution to the significance of the measurement statistics, but for TR-PIV only those samples separated by more than the flow's characteristic time scale are independent. For the current tests, the characteristic time scale was estimated for the jet case by finding the $1/e$ decay time of envelope of the autocorrelation of the HWA signal at $x = 3D$. This was found to be $t_c = 0.92$ ms, implying that the number of independent samples is $N_{\text{Ind}} \approx 1300$. The minimum 95%-confidence significant difference for values of the correlation coefficient is thus

$$\frac{t_{95\%}\sigma_R}{\sqrt{N_{\text{Ind}}}} = \frac{1.96(1)}{\sqrt{1300}} \approx 5\%,$$

where $t_{95\%}$ is the t-statistic for 95% confidence, and σ_R is unity since both u' and p' have zero mean and R is already normalized by the signal energy. The poor statistical power of this test is a significant shortcoming of the TR-PIV measurements. If all the image pairs were independent, this difference would be less than 2%. However, in § 3.6.3, it is clear that this statistical power still proves sufficient to draw meaningful conclusions.

The space–time resolution of the PIV measurements is limited by the vector spacing (1.1 mm) and the acquisition rate (7.5 kHz and 9 kHz). The spatial resolution limit can be compared to the turbulence length scales by invoking the frequency-dependent Taylor microscale presented by Kerhervé & Fitzpatrick (2010): $T_\lambda(f) = U_c/2\pi f$, where U_c is the convection velocity of the turbulence, which is determined in § 3.6.3. Kerhervé

& Fitzpatrick (2010) showed that for jet turbulence at high frequency, there is a near universal frequency-dependent fixed-axis length scale associated with the fluctuations. The implication for these measurements is that the spatial resolution corresponds to the length scale of the turbulent fluctuations at $U_c/2\pi\Delta x_{\mathrm{PIV}} = 8.6$ kHz. In the cylinder case, the temporal resolution can be compared to the frequency of vortex shedding $f_{\mathrm{Peak}} = 1.9$ kHz, yielding ≈ 4 velocity data points per oscillation, while in the jet case, the temporal resolution can be compared to the flow's characteristic time scale ($t_c = 0.92$ ms), showing each characteristic time is resolved by ≈ 80 velocity data points. However, in each case the temporal resolution of the correlation coefficient comes from the microphone data rate, giving 16 data points per oscillation in the cylinder case and 250 points per characteristic time in the jet case.

Also, as discussed in § 3.2.3, the spatial and temporal resolutions of TR-PIV are not independent, a finite spatial resolution has an effect on the frequency spectrum described by the filter $\mathrm{sinc}^2(\pi f W_{x,\mathrm{PIV}}/U)$. The inverse of this filter can be applied to the spectra as a correction; however the greatest deviation from unity of this ratio for these measurements is less than 10%, which is barely perceptible on a log scale, so no correction was performed. This filter effect is more pronounced for flows with lower convection velocities and measurements at higher frequencies.

The error of the entire PIV evaluation chain is difficult to assess. PIV experiments generally obtain a precision of ≈ 0.1 pixels (Raffel *et al.*, 2007), which is ≈ 0.5 m/s for these tests (4% of the peak turbulence intensity in the jet). A convenient way to estimate the precision error for TR-PIV time series is to calculate the peak cross-correlation between two neighbouring PIV vectors. The maximum correlation value should be nearly unity if there is no random error. This does not account for error that is spatially correlated. As a check with the jet data, in AOI3 for two neighbouring vector locations on the jet centre-line at the centre of the AOI and at the upstream edge of the AOI, the cross-correlation peaks are 0.97 and 0.87, respectively, indicating that the RMS error at the AOI centre is less than 3% of the signal energy, but it is significantly greater at the AOI edges. Since this error is uncorrelated with the flow fluctuations, the effect on the correlation measurements will be a reduction in the magnitude of $R_{u'p'}$ for all time lags. A second way to check for excessive error is by direct comparison to the HWA measurements. The close agreement between both the RMS and mean HWA and PIV measurements presented in appendix A.1 shows that the total error is low. The effect of the precision error on the frequency-domain measurements will be the presence of a noise floor in the autospectra and a reduction of the coherence over all frequencies. These issues become apparent in the results in §§ 3.6.2 and 3.6.3.

3.6 Results and discussion

3.6.1 Wavelet separation

Figure 3.5(a) shows the ability of the wavelet algorithm to separate the components of the pressure signal. The spectra match the expected shapes for the separation with the signal above a certain cut-off dominantly appearing as acoustic while below the cut-off the energy is dominantly hydrodynamic. For reference, the empirically derived cut-off of Arndt *et al.* (1997) is plotted for each case. Contrary to the criteria of Arndt *et al.* (1997), the non-dominant signal can be retrieved even though its energy is orders of magnitude below the dominant signal beyond the cut-off. The location of the cut-off from the wavelets corresponds well with the criteria of Arndt *et al.* (1997). This result is similar to those reported by Grizzi & Camussi (2012) when they introduced this technique.

Pertinent to the current analysis is the comparison between the correlations obtained by using the filtered and unfiltered signal shown in figure 3.5(b). The correlation signal from the filtered acoustic signal is significantly higher than from the total signal. This results in an increase in signal-to-noise ratio when using this technique. Additionally, the hydrodynamic component of the signal is barely correlated with the velocity fluctuations. This is especially useful for the current jet investigation because the total sound output from such a low-speed jet is relatively low. Figure 3.5(c) also gives an indication of the time–frequency content of each signal component by plotting the modulus of the coefficients of a Continuous Wavelet Transform (CWT) of each signal component (Torrence & Compo, 1998). The CWT plot is easier to interpret than a visualization of the discrete transform used in the wavelet separation technique. The plots show that the separation makes a clear distinction between pressure fluctuations associated with the resonance peak and the lower-frequency fluctuations.

3.6.2 Tandem cylinders

Figure 3.6 presents a summary of the time and space resolution for the TR-PIV in the tandem cylinder test case. Figure 3.6(a) shows that the correlation map in the wake of the cylinder is characteristic of vortex structures, a result consistent with the vortex shedding behind the cylinders at the same frequency as the sound source from the cylinders. Since the fluctuating forces acting on the cylinders are associated with this vortex shedding, the dominant sound source is of dipole nature, and the shed vortices are well correlated to the sound. It can be clearly seen that the TR-PIV shows the same underlying structure as the HWA measurements but with better spatial resolution. Figures 3.6(b) and (c) compare the power spectra obtained at two x-locations behind

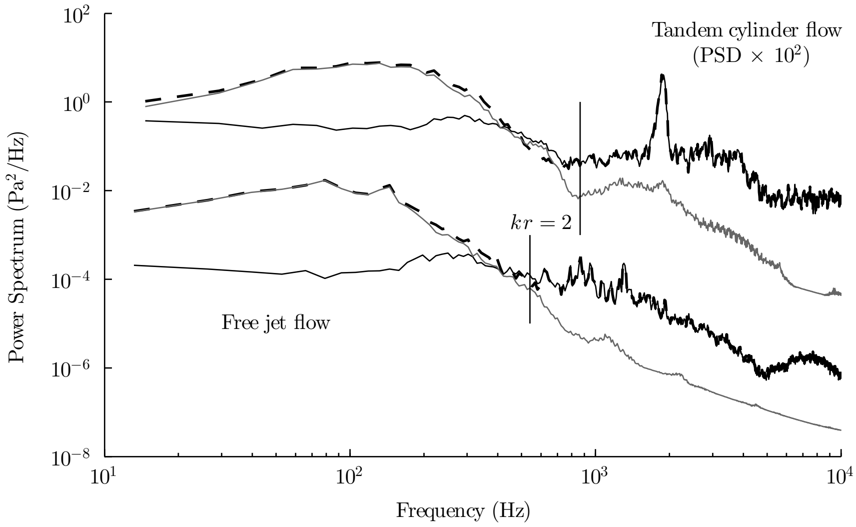

(a) Pressure spectra of each pressure component (p'). $ky = 2$ is indicated for each microphone location. The tandem cylinder curve is shifted up by a factor of 10^2 for clarity.

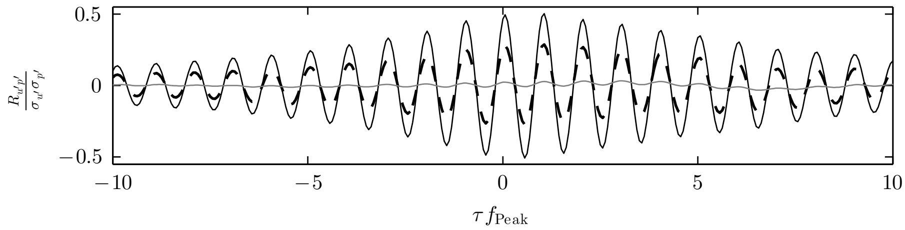

(b) Comparison between correlations of u' (HWA) and each p' component behind tandem cylinders at $x = 1.9D_{\mathrm{Cyl}}, y = -1.3D_{\mathrm{Cyl}}$. ($f_{\mathrm{Peak}} = 1.9$ kHz.)

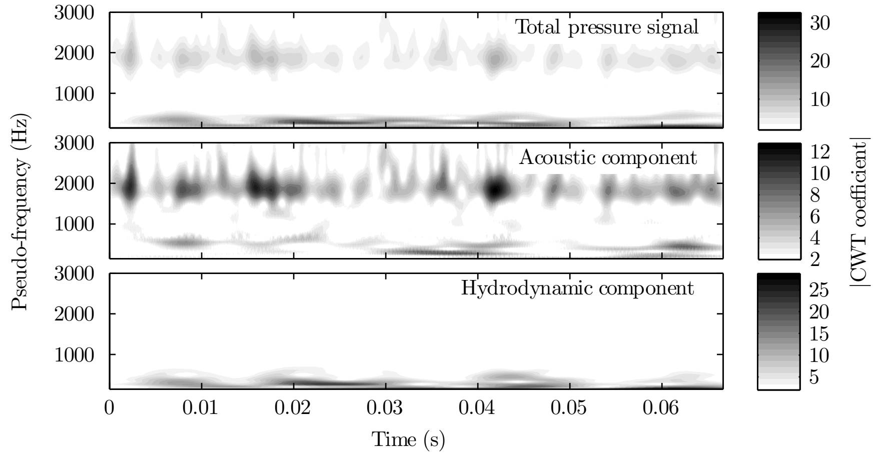

(c) Example p' microphone signal time–frequency contours for tandem cylinder flow.

Figure 3.5: Wavelet filtering of microphone signals in jet near field. – – – Total pressure signal, ——— Acoustic component, ——— Hydrodynamic component.

the cylinders, and there is good agreement for the peak corresponding to the vortex shedding frequency, but the agreement is not so good at higher frequencies where the TR-PIV seems to overestimate the spectrum. This can be associated with either temporal aliasing or a PIV measurement noise floor. It is difficult to differentiate between these two error types, but regardless of the origin of the error, the effect will be to reduce the coherence estimate. The onset of this error occurs well below the Nyquist frequency of 3.75 kHz and represents the high-frequency limit of the usefulness of the TR-PIV measurements.

For the time-domain results in figures 3.6(d) and (e), there is very good agreement in shape, amplitude, and phase of the curves, even when error is present in the frequency domain. This indicates that despite the TR-PIV error evident in the frequency domain, TR-PIV can still reproduce the correlation features available from HWA and traditional PIV. Figures 3.6(f) and (g) show that the TR-PIV error reduces the coherence, and the error is quantified in figures 3.6(h) and (i), which plot the coherence error, here defined as

$$\varepsilon_{\gamma^2} = |\gamma^2_{\mathrm{HW}} - \gamma^2_{\mathrm{PIV}}|. \tag{3.7}$$

This error is highest near the edges of the coherence peak where the PIV signal energy approaches the level of the error. Unfortunately, in the frequency range where the error dominates (2 kHz–3.5 kHz), the investigated source is not highly coherent, making it is impossible to determine if the PIV can still capture coherence here. Because of these observations of reduced coherence in the frequency domain, the interpretation of the correlation features for the free jet case will be limited to the time domain. This result is disappointing because it negates one of the principal advantages of TR-PIV over traditional PIV: the availability of a coherence estimate.

3.6.3 Free jet

Figure 3.7 shows the TR-PIV velocity spectra of u' measured along the jet centre-line and compared to HWA. The maximum fluctuation energy is found near the end of the potential core, and within the potential core a distinct frequency peak exists around 1000 Hz. However, close to the nozzle no fluctuations are resolved, and a noise floor is evident. As noted in § 3.6.2, this floor is likely associated with the accuracy of the PIV measurements and the fact that the fluctuation intensity near the nozzle is very low. For all x considered, the spectrum levels out at high frequencies rather than decaying continuously, indicating that the frequency limit of the useful range of the TR-PIV measurements is much lower than the Nyquist frequency of 4.5 kHz. Snapshot time series of the jet flow are presented in figure 3.8 for AOI3 (middle of the

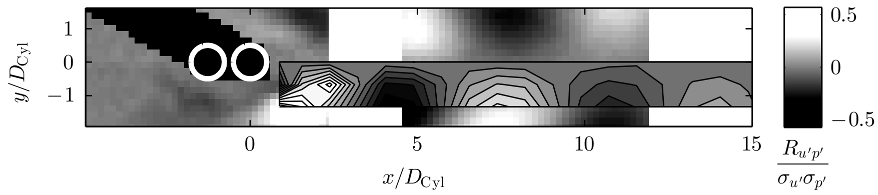

(a) Snapshot of cross-correlation between u' and p' at $\tau f_{\mathrm{Peak}} = 1.13$. (HWA measurements are boxed section.)

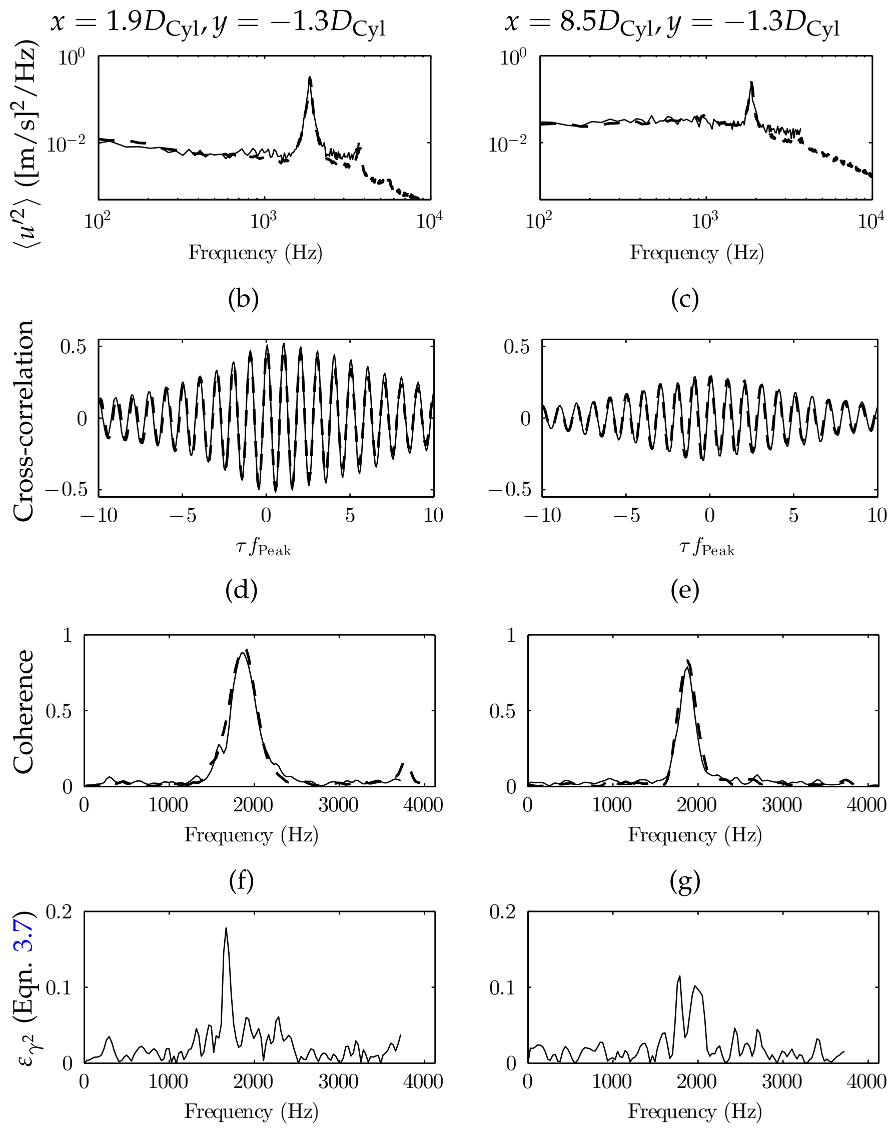

(b) (c)

(d) (e)

(f) (g)

(h) (i)

Figure 3.6: Comparison between space–time resolution of TR-PIV and HWA-based $u'p'$ correlation quantities. For (b)–(g) ——— TR-PIV, – – – HWA. For (d) and (e) $f_{\mathrm{Peak}} = 1.9$ kHz.

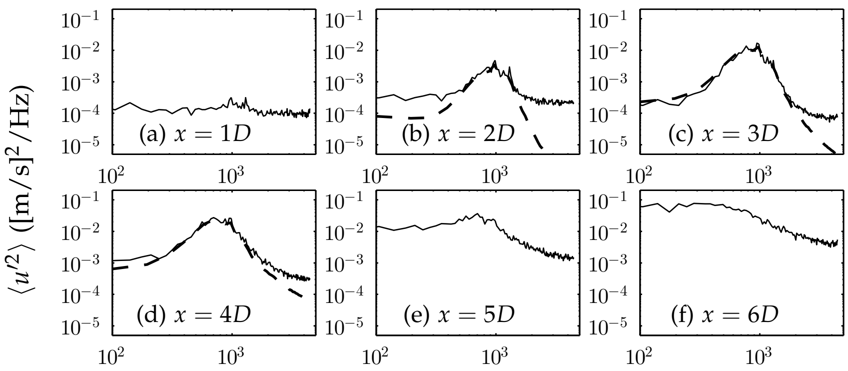

Figure 3.7: Free jet axial velocity spectra (u'). ——— TR-PIV, – – – HWA. (HWA spectra available only for $2 - 4D$.)

potential core). The dominant feature in the series is a well-defined train of higher and lower velocity regions. The distance between each successive peak is $L \approx 1.2D$. The corresponding frequency of this structure can be estimated by $f = U_c/L$, where the convection velocity, U_c, was obtained from the slope of the peaks of the space–time correlation of u' yielding $U_c = 0.7U$, a quantity unavailable from traditional PIV measurements. This leads to $f = U_c/L = 0.7U/1.2D \approx 990$ Hz, which is clearly associated with the frequency peak visible in figures 3.7(c) and (d). Figure 3.9(a) indicates the time-domain correlation signature measured on the centre-line of the jet is characterized by a dominant oscillation frequency of 1190 Hz corresponding to a Strouhal number based on a convection velocity of $fD/U_c \approx 1$. This frequency is close to the peak energy of u' and represents the dominant instability of the jet in the potential core. The space–time correlation peaks are also extended over an axial extent of $\approx 4D$. This distance is significantly greater than the centre-line integral hydrodynamic length scale of $0.9D$ reported for this jet by Kerhervé *et al.* (2010). The location of $\tau_r = 0$ is indicated in figure 3.9(a) by a thin solid line and represents the expected time lag for the correlation peaks if a Lighthill-type model of sound production by uncorrelated eddies was applied. However, here the peaks fall on a common line with a negative slope. Henning *et al.* (2010b) reported similar results previously and explained the peak signature by assuming that the main sound source is at the nozzle lip and observed that peaks downstream only represent correlation to the lip source rather than independent sound production. For the case of downstream fluctuations correlated to an upstream source, the time lags of the correlation peak can be predicted by modelling the system as in figure 3.10. Here, an upstream fluctuation $q_{s1}(t)$ originates somewhere in the jet flow and is then convected downstream at U_c. After some time, η/U_c, the fluctuation is $q_{s2}(t - \eta/U_c)$. If q is measured at both

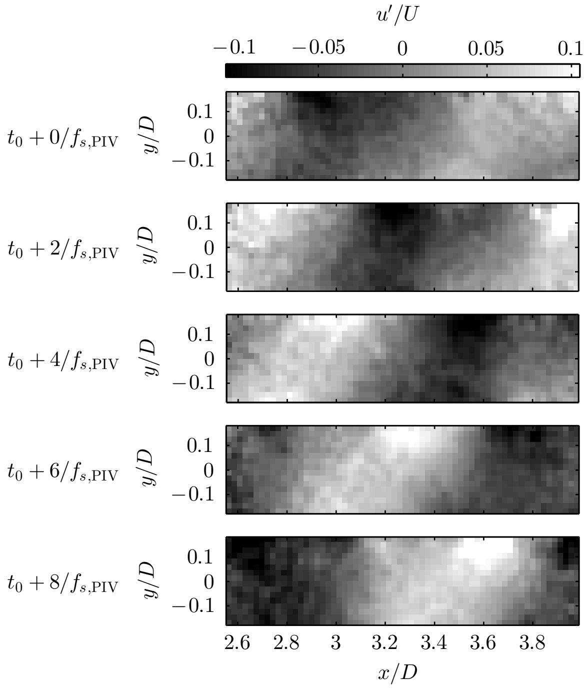

Figure 3.8: Example TR-PIV time series of u' for the free jet flow. Only every second snapshot is shown.

locations, there will be a significant correlation between q and p at both x-locations. The geometry of the model gives the expected peaks at:

$$\tau_{r,\mathrm{Peak}} = \tau_{s1,p} - \tau_{s2,p} - \eta/U_c, \tag{3.8}$$

where η is the distance between the sources, U_c is the convection velocity, and $\tau_{s1,p}$ and $\tau_{s2,p}$ are the propagation times from q_{s1} and q_{s2} to the observer location. The line from equation (3.8) is plotted as a thick dashed line in figure 3.9(a) with $x_{s1} = 0$, and the agreement is evident.

However, this correlation signature does not prove that the lip fluctuation is the dominant noise source, and true source localization is ambiguous. A simple numerical simulation with an analytical sound source can illustrate this. Consider a line source representing a distribution of correlated monopoles on the axis of the jet that has a strength per unit length described by[4]

$$q(x,t) = \frac{\partial^2}{\partial x_i \partial x_j} T_{ij}(x,t) = A\cos\left[2\pi f\left(t - \frac{x}{U_c}\right)\right]\exp\left[-\left|t - \frac{x}{U_c}\right|/t_c\right], \tag{3.9}$$

where A is the amplitude, f is the oscillation frequency, x is the axial position, t_c is a characteristic time scale of the source, and U_c is the convection velocity. The so-called

[4] $q(x,t) = \delta(y)\delta(z)q(\mathbf{x}_o,t)$ where $\delta(\cdot)$ is the Dirac delta function.

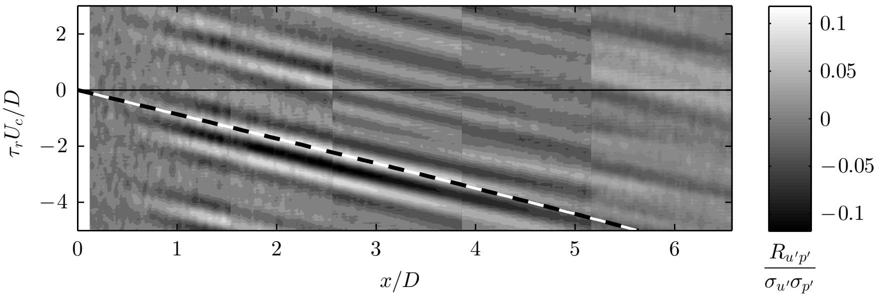

(a) Experimental free jet centre-line correlations

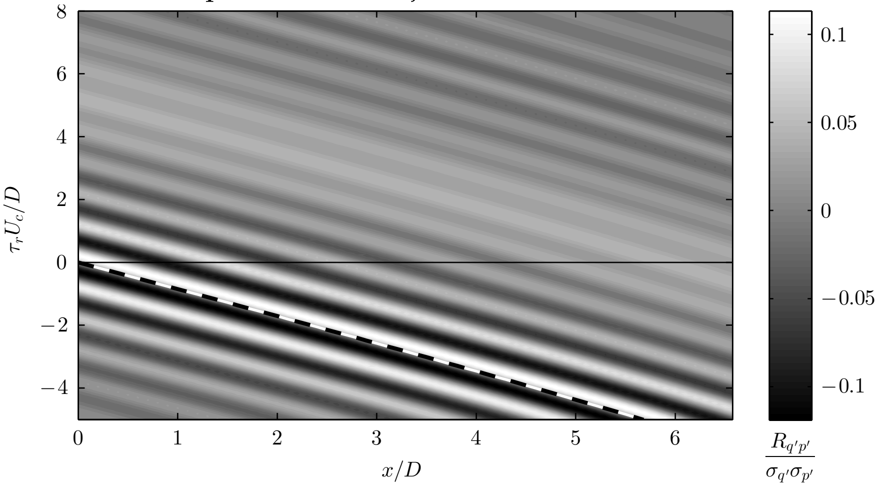

(b) Simulated correlation trace

Figure 3.9: Cross-correlation coefficient between u' (q' for simulation) and the acoustic part of p' separated by the wavelet method. ——— $\tau_r = 0$ and – – – equation (3.8).

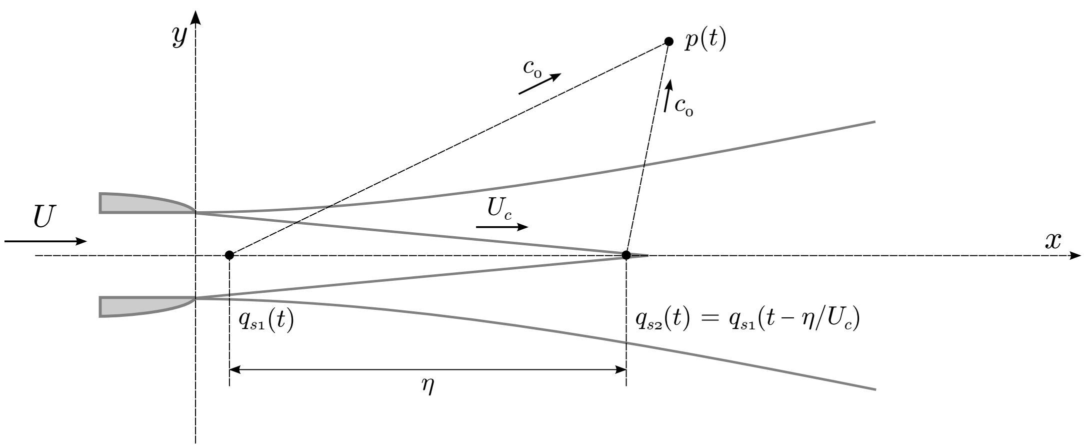

Figure 3.10: Source model for correlation simulation

Table 3.2: Summary of source simulation parameters

$A = 1$	$B = C/10$	$C = 1$
$b = 2D$	$c = 2D$	$(x, y)_{\text{Mic}} = (7, 4)D$
$f = 1190$ Hz	$t_c = 0.001$ s	$U_c = 0.7U = 59.5$ m/s
$x_{s1} = 0D$	$x_{s2} = 6D$	$dx = D/10$
$\lvert t\rvert < 18D/U$	$0 < x < 10D$	$f_s = 27$ kHz

Lighthill stress tensor is given by $T_{ij}(x, t)$. Such a source is similar to, for example, a convecting instability wave, or wavepacket as described by Cavalieri *et al.* (2011). Now, assume that the received emissions at an observer location are somehow damped and this damping is dependent on the source position. This could be possible if there was a region of high sound absorption between the source location and observer, or if some of the acoustic energy were refracted away from the particular observation location by the mean flow. This damping envelope was proposed in this case as the sum of two separated Gaussians:

$$D(x) = B \exp\left[-(x - x_{s1})^2/b^2\right] + C \exp\left[-(x - x_{s2})^2/c^2\right]. \tag{3.10}$$

The parameters for the simulation were selected to mimic the current experiment and are presented in table 3.2. x_{s1} was chosen as the nozzle lip, and x_{s2} was a location near the end of the potential core.

To simulate strong source activity at x_{s2} and weaker activity at x_{s1}, C was 10 times greater than B. The true local source strength (in the sense of sound received by the observer) is then $q_t\,(x, t) = \; q\,(x, t)\, D(x)$. The observed sound can be calculated by Lighthill's analogy (1952) using a free-space Green's function as

$$p(t) = \frac{1}{4\pi} \int_0^\infty \frac{1}{r} q(x, t - r/c_0) D(x) dx. \tag{3.11}$$

$q\,(x, t)$ and $p\,(t)$ can now be correlated directly. Since the correlation is normalized by the local signal strength and the modulation $D\,(x)$ is constant in time, the result is the same as that obtained using $q_t\,(x, t)$. Time series of $q\,(x, t)$ were created for each point on a one-dimensional grid with a spacing of dx and a sample rate of f_s. The oscillation frequency, f, was chosen to correspond to the main oscillations in figure 3.9(a). A contribution to the far-field pressure for each grid point was then calculated independently by shifting each $q\,(x, t)$ by $|\mathbf{x}_o - \mathbf{x}_s|/c_0$ and multiplying by $1/4\pi r$. The shift was effected by passing $q\,(x, t)$ into the frequency domain, multiplying by $e^{-2i\pi f \phi |\mathbf{x}_o - \mathbf{x}_s|/c_0}$, and returning to the time domain. The observation location was that of the first microphone from the experiment ($x = 7D, y = 4D$). Each contribution was then multiplied by $D(x)$ and all the contributions were summed and multiplied by dx at each time step.

Figure 3.9(b) indicates the similarity between the experimental correlations and the simulated ones with the peaks of the correlation still predicted by equation (3.8). The result is consistent with the presence of axially extended, coherent structures as the sound source in the jet, but the time-domain correlation cannot prove this unambiguously. It should be noted for the simulation that the dominance of the correlation beginning at the nozzle depends partly on the truncation of the spatial domain at $x = 0$, which inhibits the source's self-cancellation, but this truncation is warranted by the fact that all real jets do have a nozzle, which will affect the source radiation. An evaluation of the effect of the nozzle is beyond the scope of this work. It is clear, however, that the fluctuations on the centre-line related to the emitted sound have a correlation length much longer than the traditional centre-line integral hydrodynamic length scale ($0.9D$, Kerhervé *et al.*, 2010). When the correlation is dominated by a single frequency and the source is correlated over a large axial extent, the cross-correlation technique fails to uniquely locate the strongest source activity.

3.7 Implications for noise source identification and control

The possibility of extended, coherent structures as prominent sound sources in jets has several implications for attempts to predict and control jet noise. The observation of these structures and the recognition of their importance in the generation of far-field emissions in jets is not new. The earliest observations of such structures date back to the 1960s. In fact, experimental evidence for such wavepacket-type sources was also observed early on (Crighton, 1975; Crow & Champagne, 1971; Mollo-Christensen, 1963, 1967). However, the general ambiguity of the direct correlation technique for noise source localization of these types of sources has not been considered before, nor has the consistency between a theoretical wavepacket-type source's correlation pattern and that of an experimental jet been presented.

The first implication of the presence of such large-scale structures was already identified in § 3.6.3 as the ambiguity of the direct correlation technique. The technique cannot isolate a region that can be considered the dominant source region, disallowing the development of targeted noise reduction schemes. A second implication is that the traditional noise source models used in Lighthill-type acoustic analogies (§ 2.2.4) that use the compact-source assumption in their definition of the source term cannot accurately predict the sound emissions. However, when it comes to developing sound reduction techniques, the large-scale nature of the sources is an advantage, since it reduces the number of degrees of freedom that must be controlled to influence the source. Trying to achieve meaningful control authority over a field of random turbulence is unfeasible, while influencing individual large-scale structures may prove to be a simpler task.

The wavepacket-type source used in the simulation in § 3.6.3 was not an arbitrary choice. Evidence for the dominance of this type of sound source has been mounting in the past several decades. Chapter 4 focuses primarily on the properties of wavepackets in the jet near field, showing evidence for their dominance in this region and also taking steps to predict the far-field sound directly from experimentally obtained wavepacket representations. A fuller description of wavepackets and their properties will be reserved for that chapter.

The earliest investigations of wavepackets relied on establishing order in the jet by periodic forcing in order to investigate the properties of wavepackets, and it was in these jets that evidence for their existence was first discovered. More recent experiments and simulations have also been able to detect wavepackets in unforced jets, particularly at high Mach number (Kerhervé *et al.*, 2012; Reba *et al.*, 2010). As a complement to these earlier studies, the evidence obtained in this chapter relies on no prior assumptions about the spatial extent of the sound sources or orderliness of the jet flow, establishing a plausible argument for the presence of wavepackets in lower-Mach-number, unforced jets. Though the results in § 3.6.3 are not definitive evidence for the presence of wavepackets, they show that a wavepacket hypothesis is consistent with the results available from the direct correlation technique.

3.8 Conclusion

3.8.1 Summary

TR-PIV has been shown to be an effective tool for identifying the same correlation features available with traditional PIV and single-point measurement techniques such as HWA. The advantage of TR-PIV in this case is that the results are resolved both in time and space for each flow realization as opposed simply to ensemble averages. This will enable future efforts to focus on how individual flow realizations contribute to sound emission, an essential component of noise reduction schemes.

Error at high frequencies is an important consideration in TR-PIV turbulence measurements. This error is thought to arise from two sources, the precision error of TR-PIV and temporal aliasing, but a clear distinction is not possible with the current data. A tandem cylinder configuration in a jet flow has shown that this error does not significantly affect the calculation of the time-domain correlation coefficient, but it does affect the estimation of all turbulent properties in the frequency domain, especially at higher frequencies. This represents a significant shortcoming of the TR-PIV technique because the availability of a coherence estimate is a principal theoretical advantage of TR-PIV over traditional PIV. It may be possible to use the coherence function as a correction for the high-frequency error, but this will require further study.

The results for the cross-correlations in the free jet case indicate that the localization of sound sources is complicated by the mutual correlation of fluctuations, which appear to convect with the flow. A simple model was implemented and validated for how axially extended, convected flow fluctuations originating at the nozzle can explain the observed correlation signature without requiring the main source location to be at the nozzle lip. The high correlation values observed far downstream indicate that the traditional hydrodynamic integral length scale appears to underestimate the correlation length of the sound-generating components of the flow, which may only account for a small portion of the total flow energy. It also remains to be seen exactly what the effect of error across the flow field has had on these 'surprising' results.

Though the results show that the correlation technique does not constitute definitive proof of the nature of the sound sources, they are consistent with the presence of axially extended wavepackets.

3.8.2 Outlook

As the technique is further refined, the spatial nature of TR-PIV may yield critical information about the distribution and behaviour of aeroacoustic sound sources. In order to achieve this, it will be necessary to develop techniques to extract the acoustically important components of the raw velocity signal and to treat the problem of high-frequency error.

The ability to investigate individual flow realizations will become more crucial as noise prediction techniques develop toward time-domain predictions (see chapters 4 and 5). This may enable the development of a better understanding of the relationship between noise sources and their far-field sound emissions, allowing for more effective noise reduction schemes to be proposed.

Further evidence for the presence of wavepackets in subsonic jets and their causal relationship to the far-field sound emissions is presented in chapter 4. The current results add to the mounting evidence supporting the wavepacket description of jet noise sound sources as a useful framework for jet noise predictions.

Chapter 4

Near-field wavepackets and time-resolved far-field sound

4.1 Background

4.1.1 What is a wavepacket?

The earliest conceptions of turbulence (prevalent in the 1950s, and still the basis of many jet noise models today) considered it to be made up of a superposition of stochastic eddies, each fluctuating and generating sound on its own. It was under this assumption that Lighthill (1952) was able to derive his important scaling laws. In the early 1960s, the discovery of coherent structures in turbulence—that is, structures that extend or interact beyond the typical turbulent eddy length scale—signalled the beginning of a new era of turbulence research. Since it was known that a coherent sound source is much more efficient than a random one, the presence of such structures in turbulent jets hinted that they may play an important role in jet noise emissions (Armstrong *et al.*, 1977; Mollo-Christensen, 1963). The role of coherent structures in turbulence and noise production has been a topic of intense research ever since. Mollo-Christensen (1967) considered such a coherent source structure as a 'semi-infinite antenna for sound.' This construct is now referred to as a *wavepacket*, the emission properties of which are consistent with many of the observed features of jet noise (Cavalieri *et al.*, 2012a). A wavepacket (illustrated schematically in figure 4.1) is an axially convecting disturbance coherent over a significant length with a particular frequency, f, and wavenumber, k. Wavepackets appear as spatially modulated sinusoidal disturbances that convect in the flow, *growing* in amplitude from the jet exit, *saturating* at a maximum amplitude at some point, and finally *decaying*. The amplitude envelope described by this growth, saturation, and decay does not convect. The wavepacket may be observable in any of the flow variables,

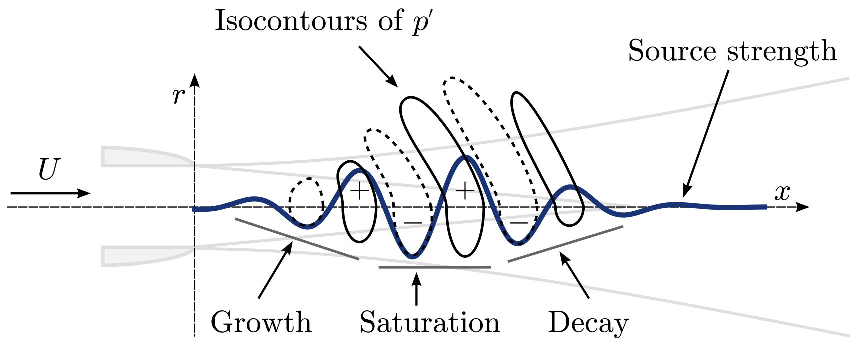

Figure 4.1: Schematic representation of a snapshot of a wavepacket and its sound radiation in a jet. The thick solid curve represents the source strength distribution, and the isocontours of p' represent the pattern of the wavepacket's sound emissions.

and is manifest as fluctuations about the mean flow, which constitute a source in Lighthill's (1952) analogy. The oscillatory shape of the wavepacket means regions of positive and negative source strength (see figure 4.1) partially cancel and only some of the fluctuation energy 'escapes' to the far field. The relative efficiency of these emissions is dependent on several factors, which are discussed in § 4.1.3.

Forerunners such as Mollo-Christensen (1963, 1967), Crow & Champagne (1971), and Crighton (1975) made early observations of these signatures and developed the mathematical basis for their sound production and prediction. Jordan & Colonius (2013) have presented a comprehensive review of the developments in wavepacket-based jet noise research, presenting the state of the art in wavepacket-based jet noise predictions. A brief description of the more important features of wavepackets is presented here to motivate and explain the current work. A wavepacket description of the noise sources in a jet constitutes an *Ansatz*: an educated guess about a useful paradigm for predicting jet noise. The wavepacket model does not claim to capture all of the jet dynamics, and it can only be confirmed as useful by comparing wavepacket predictions to real measurements. In all likelihood, wavepackets will not tell the whole story of jet noise emissions, but they do appear to account for many of the salient features, especially at low emission angles (Cavalieri *et al.*, 2012a; Jordan & Colonius, 2013).

The attraction of a wavepacket description of jet noise sources is that it has a relatively low-order structure compared to the full non-linear jet dynamics. However, beyond simply reducing the complexity of source modelling, this lower-order source structure also corresponds to the observation in real jets of the lower-order structure of the far-field jet emissions compared to the in-flow jet dynamics, an observation discussed in § 2.2.3. This leads to the possibility that describing the important jet dynamics for noise emissions is a lower-order problem than describing the full jet flow dynamics. In fact, there is some evidence that the full high-order non-linearity of the unsteady in-flow mechanics of the jet simply creates a mean base flow, disturbances about which are responsible for sound generation (Gudmundsson & Colonius, 2011). From this perspective, it may be possible to predict the mean flow with traditional numerical tools and then obtain sound predictions with a separate analysis that predicts only particular sound-related disturbances about the mean flow.

4.1.2 Wavepackets and flow stability

4.1.2.1 The stability problem

The physical basis for the appearance of wavepackets in a jet arises from a stability analysis of the shear layer. The concept of stability in fluid mechanics describes the growth of disturbances (linear or non-linear) about a steady mean flow. For jets, the stability analysis predicts the streamwise growth of disturbances in the shear layer. The first step in the stability analysis is a reformulation of the Navier–Stokes equations into a steady part (mean flow) and an unsteady part (the disturbances; see Herbert, 1997). The particular restrictions used in selecting the mean flow for the decomposition differentiate the different types of stability analysis. *Linear Stability Theory* (LST) requires that the flow be parallel, while the *Parabolized Stability Equations* (PSE; see Herbert, 1997) allow for a slowly spreading mean flow, which is better suited to the analysis of jets (Gudmundsson & Colonius, 2011). PSE can be performed in either a linear or non-linear framework. The stability solutions—calculated on an azimuthal mode-by-mode, frequency-by-frequency basis—correspond to the unstable modes[1] of the jet base flow in either case. Good agreement between the stability predictions and the measured fluctuations verifies the presence of wavepackets in the jet, providing a basis on which to build wavepacket noise prediction schemes.

4.1.2.2 Mathematical solutions: Parabolized Stability Equations (PSE)

Purely analytical stability solutions are rarely tractable for flows of practical interest, but the solutions can be calculated numerically with very little computational expense. In comparison to an LES simulation, which could take thousands of processor-hours for a jet like the one considered in this work, the PSE solutions are calculated in a matter of minutes on a standard desktop computer. This is an important consideration because, as discussed in § 2.1, for a particular jet noise prediction scheme to be integrated into the engine design cycle, it must be possible to recalculate solutions

[1] An unfortunate duplication of terminology in the literature allows 'mode' to refer either to modes from an azimuthal Fourier decomposition, or to spatial modes corresponding to eigensolutions of the flow equations about a mean flow. Both terms will be used in the following discussion, but azimuthal Fourier modes will be referred to as 'azimuthal modes' whenever the interpretation is ambiguous.

based on design changes in a reasonable amount of time. PSE-based prediction schemes fulfill this criterion.

Herbert (1997) has given a full description of the development and application of PSE, and recent developments in the application of PSE to the near-field statistics of jet flows have been described by Gudmundsson & Colonius (2011). In addition, the PSE computations used in this chapter for comparison to the experimental results—which are limited to linear PSE—were already presented by Cavalieri *et al.* (2012b). This section therefore includes only the level of detail necessary to motivate the current work.

The stability computation begins with either a measured or calculated mean flow profile. For design purposes, this profile could even be calculated by a RANS simulation, which could be integrated into a rapid design cycle. The stability computation takes this mean flow and gives solutions for the disturbances that correspond to a number of shape functions with corresponding growth rates and oscillation frequencies in each dimension. For jet calculations, a PSE solution is obtained taking the LST solution at the nozzle exit as a boundary condition and then marching the solution downstream to solve for the shape functions throughout the whole jet flow. This is possible due to the parabolization of the equations, with each step independent of the solution downstream (Gudmundsson & Colonius, 2011). The outputs of the stability analysis are the amplitudes and relative phases of the flow variable fluctuations in the jet ($u', v', w', p', \rho', T'$) for a given frequency and azimuthal mode. In the linear framework, each mode amplitude includes a free constant that must be chosen after comparison with one of the flow variables. With the present jet, these constants have already been obtained by comparison with u' measured on the jet centreline (Cavalieri *et al.*, 2012b).

4.1.2.3 Experimental solutions: Proper Orthogonal Decomposition (POD)

Stability theory predicts fluctuations in the jet that are coherent over a large axial extent. In regions of the jet dominated by small-scale turbulence, the axially coherent fluctuations may be masked by these uncorrelated fluctuations. To compare the stability results to the axially coherent fluctuations in the jet, Proper Orthogonal Decomposition (POD, Berkooz *et al.*, 1993) is typically used to isolate the most energetic coherent fluctuations (the lowest POD modes). POD acts in a similar manner to a Fourier series decomposition in that it decomposes a signal into a set of orthogonal basis functions. The difference is that instead of using predefined basis functions (*e.g.* sinusoids for the Fourier series), POD uses the data itself to determine a set of optimized basis functions (modes) that reflect the energy distribution in the data. By definition, POD yields a set of orthogonal modes of which each successive mode contains the greatest possible amount of remaining energy in the decomposition. Thus POD modes are guaranteed to capture the greatest portion of the signal energy in the fewest modes. The object is to reduce the system into the fewest possible degrees of freedom while retaining the maximum possible energy.

Here, the POD kernel is integrated in the axial direction (details presented in § 4.4.1), returning a statistical picture of the flow fluctuations that dominate the fluid motion that is coherent along the jet axis. Since POD is a statistical tool, the result yields a description of the dominant fluctuations only on average as opposed to their real-time mechanics, but since the wavepacket *Ansatz* makes precisely this assumption—that wavepackets dominate the coherent fluctuations—POD is sufficient to demonstrate the existence of wavepackets in the jet. If the wavepacket *Ansatz* holds—that is, that the dominant axially coherent fluctuations can be predicted from stability—the POD modes constitute experimentally derived wavepackets, and there will be close agreement between the first POD mode (most energetic coherent fluctuation) and the stability solution. This agreement has already been demonstrated in the velocity field of the present jet (Cavalieri *et al.*, 2012b; and see § 4.2), and in the pressure field of similar and higher-Mach-number jets (Gudmundsson & Colonius, 2011); however, questions still remain as to the reasons for disagreement beyond the end of the potential core as well as a firm relationship between the near-field wavepackets and the far-field sound (see § 4.2). This work addresses these questions.

The POD application here uses a formulation that returns complex-valued POD modes containing spatial amplitude and phase information along the jet axis for each frequency and azimuthal mode. These modes can be compared directly to the PSE predictions for the envelope and phase of the unstable modes. Full details of the analysis procedure used in the application of POD here are presented in in § 4.4.1.

4.1.3 Far-field emissions from wavepackets

Crow (1972; see Crighton, 1975) was the first to show that the sound emissions from simple wavepacket sources could be calculated analytically, and more recent work has noted the effect on sound emissions of several wavepacket parameters including the spatial envelope (Crighton & Huerre, 1990), temporal growth and decay (Sandham *et al.*, 2006), and intermittency (Cavalieri *et al.*, 2011). Early experimental work in analyzing wavepackets focused on forced jets because measurements could be phase-locked to an external trigger, but recent work has also found evidence of wavepackets in the velocity fields of natural jets (Cavalieri *et al.*, 2012b) and provided a technique for educing a simplified wavepacket structure from numerical simulation data (Kerhervé *et al.*, 2012).

The pertinent parameters for describing a wavepacket are the wavenumber, k; frequency, f; and spatial envelope. Together, k and f prescribe the convection speed, $U_c = 2\pi f/k$, of the wavepacket, which can be subsonic ($U_c < c_0$) or supersonic ($U_c > c_0$) depending on the jet's Mach number[2]. U_c is the key parameter in determining the efficiency of the conversion of wavepacket fluctuations into propagating sound emissions. This is because only the part of a wavepacket's k–f spectrum that is supersonic radiates to the far field (Crighton & Huerre, 1990; Jordan & Colonius, 2013). This effect is illustrated schematically in figure 4.2, in which it is clear that a subsonic wavepacket with no spatial envelope is silent, while the same wavepacket convecting supersonically has strong Mach-wave emissions. In order for a subsonic wavepacket to emit sound at all, it must have a finite spatial envelope, which causes part of the k–f spectrum to 'leak' into the radiating zone, resulting in escaping sound emissions. In general, the higher the convection speed of the wavepacket, the more efficient the source. This implies that wavepacket sound sources will be more dominant for higher-Mach-number jets.

The spatial envelope is determined by the wavepacket's growth, saturation, and decay (introduced in § 4.1.1) as it convects in the jet. This is the envelope that is predicted by a stability analysis or a POD decomposition, which reiterates the utility of accurate statistical wavepacket descriptions. The particular shape of the wavepacket influences the portion of the fluctuations that radiate, and therefore the wavepacket efficiency.

Both the average convection speed and spatial envelope are statistical quantities amenable to comparison to POD or stability analyses. Recent work has determined the influence of unsteady parameters such as temporal growth and decay (Sandham *et al.*, 2006) and intermittency (Cavalieri *et al.*, 2011). In both cases, the effect of unsteadiness was shown to be an increase in the wavepacket's efficiency. Since neither stability nor POD analyses account for these effects, their ability to predict the far-field emissions will depend on the degree to which these unsteady factors increase the efficiency. This is likely to be more important for low-Mach-number jets where little of the wavepacket energy is already radiating. For higher-Mach-number jets, where most of the energy already radiates, the effect is likely to be smaller. The possibility of time-domain effects is considered in the analysis in § 4.4.

4.1.4 Evidence for wavepackets as a jet noise source structure

Exact and approximate solutions to the far-field emissions from wavepackets are in themselves elegant solutions to an interesting problem, but in the context of jet noise

[2]The wavepacket can also be sonic ($U_c = c_0$), but this case is not practically different than the supersonic case.

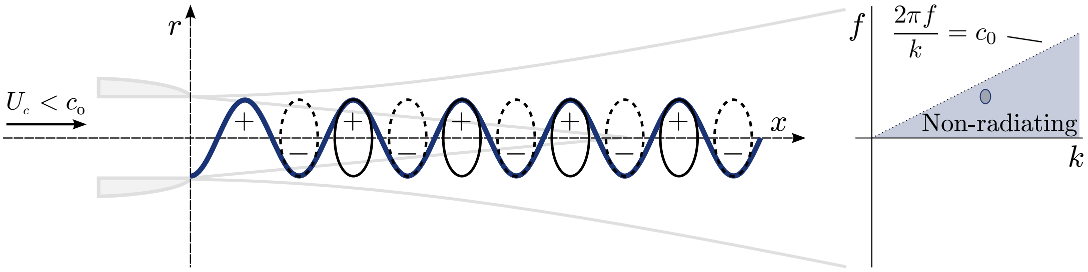

(a) Subsonic wavepacket with no sound emissions

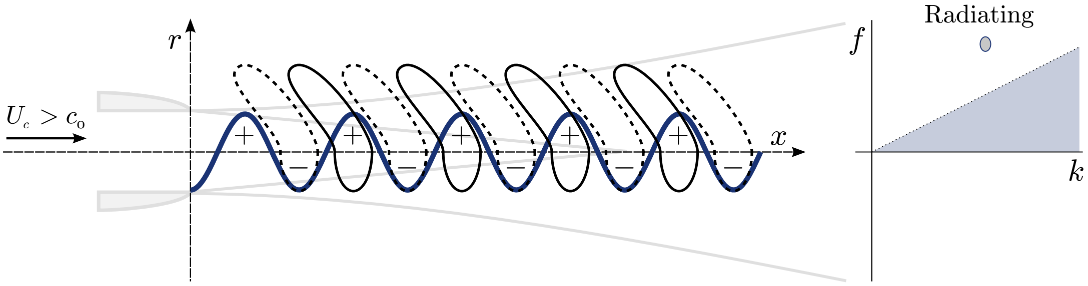

(b) Supersonic wavepacket with Mach wave radiation

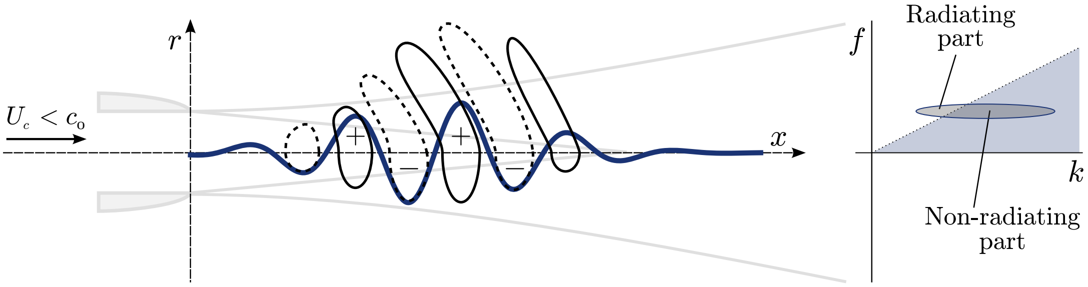

(c) Subsonic wavepacket with sound leakage

Figure 4.2: Schematic representation of wavepackets at different convection velocities (left, see figure 4.1 for explanation) and their corresponding k–f spectra (right) showing sound radiation in a jet (Jordan & Colonius, 2013).

prediction, they are only useful if wavepackets are indeed a dominant jet noise source mechanism. Evidence that wavepacket-type sources do dominate far-field emissions—at least at low θ—has been steadily mounting in recent years. In particular, the lower-order azimuthal structure of the far-field sound compared to the more complex near-field fluctuations has been interpreted as evidence for a lower-order sound production mechanism (Brown & Bridges, 2006; Tinney & Jordan, 2008). Cavalieri *et al.* (2012a) have also demonstrated experimental evidence for *superdirectivity*—an exponential decay of directivity with θ typical of wavepacket sources and predicted by Crighton & Huerre (1990)—in the present jet. Others (Kerhervé *et al.*, 2008, 2012; Tinney & Jordan, 2008; see also chapter 3) have also shown by a variety of filtering and data reduction techniques that near-field signatures corresponding to low-order structures that are hidden in the jet flow are related to the far-field sound.

4.2 Motivation for current experiments

4.2.1 Context

Despite recent favourable agreement demonstrated between PSE predictions and both in-flow and near-field flow fluctuations (Cavalieri *et al.*, 2012b; Gudmundsson & Colonius, 2011), as well as wavepacket predictions and far-field pressure statistics (Cavalieri *et al.*, 2012a; Léon & Brazier, 2011), several questions remain unanswered about wavepackets and sound emissions in jets. For example, Cavalieri *et al.* (2012b) found that the agreement between stability predictions and experimental data deteriorated beyond the end of the potential core. Also, a clear relationship has not yet been determined between time-domain wavepacket fluctuations and far-field sound emissions. To this end, the objectives of this chapter are to determine if wavepackets are still present beyond the potential core and to determine if experimental wavepacket signatures can be related to the observed far-field sound. Though the pressure measurements in this work allowed the recording of the azimuthal modes $m = 0$, 1, and 2, the analysis presented here considers only the axisymmetric azimuthal mode ($m = 0$), both in the near and far fields. This mode has been shown to be dominant in the far-field emissions at low θ (Cavalieri *et al.*, 2012a).

Cavalieri *et al.* (2012b) analyzed the velocity field of the currently studied jet for the presence of wavepackets using the PSE approach and found strong evidence that up to the end of the potential core for St $\gtrsim 0.3$ the velocity fluctuations are dominated by wavepacket activity. Some of these results are reproduced in figures 4.3 and 4.4. The close agreement up until $x/D \approx 5$ indicates the effectiveness of PSE for predicting flow fluctuations in this region, but the deterioration in agreement further downstream

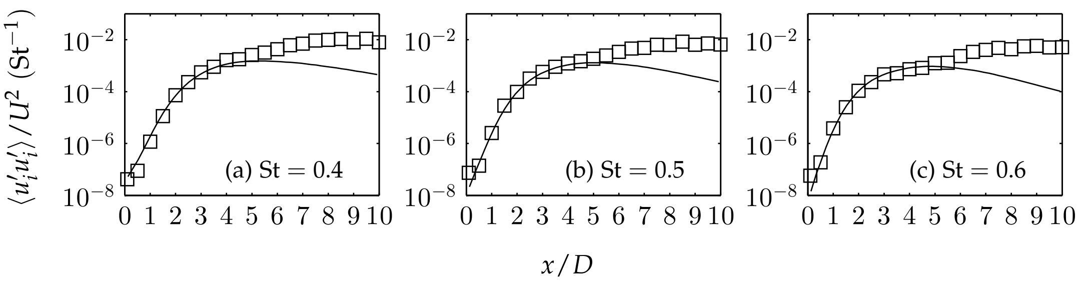

Figure 4.3: Comparison between linear PSE predictions (———) and measured u' (□) for the axisymmetric mode on the jet centreline for $M = 0.4$ and $0.4 \leq \mathrm{St} \leq 0.6$. Data from Cavalieri *et al.* (2012b).

remained unexplained. Cavalieri *et al.* (2012b) proposed three possible hypotheses to explain this:

H1. Downstream of the end of the potential core non-linear effects become significant in the development of wavepackets, invalidating any linear instability-wave model;

H2. Linear instability waves persist for high x, but account only for a small part of the azimuthally coherent overall energy;

H3. The instability-wave *Ansatz* no longer applies to describe velocity fluctuations in this region: downstream of the potential core the wavepackets degenerate into turbulence.

The dataset available at the time did not allow the identification of the dominant effect. This work aims to further this investigation by examining the pressure field to clarify the fate of wavepackets downstream and by providing an opportunity to test these hypotheses. It is important to note that these hypotheses are not necessarily mutually exclusive, and any combination of them could be responsible for the observed deviation, but in any case the present study should help isolate the dominant phenomenon.

This chapter reports the analysis of data obtained from a ring array of microphones in the jet-far field and by a conical array of microphones in the part of the near pressure field of the jet labelled the linear hydrodynamic region (Suzuki & Colonius, 2006). In this region, the pressure fluctuations are dominated by waves with subsonic phase speed in the axial direction. These fluctuations are thus mostly of hydrodynamic nature, but they do not exhibit the rotational, turbulent nature of the fluctuations within the jet flow. The near-field array used in these experiments is similar to that used by Suzuki & Colonius (2006) and Gudmundsson & Colonius (2011) in their similar investigations.

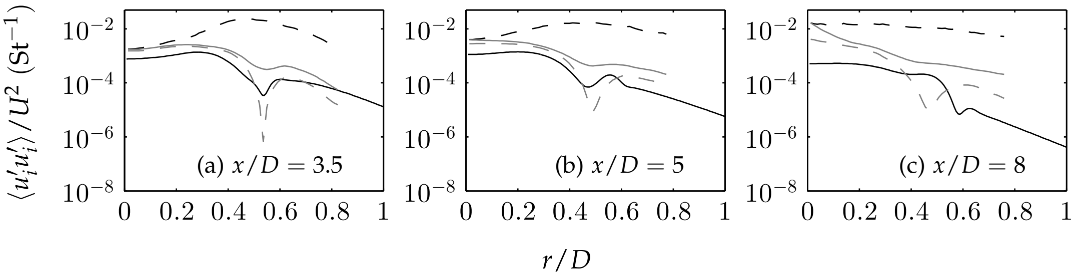

Figure 4.4: Comparison between linear PSE predictions and measured u' for $M = 0.4$ at three axial stations. ——— PSE, – – – Experimental u', ——— Axisymmetric mode of u', – – – First POD mode of axisymmetric mode of u'. Data from Cavalieri *et al.* (2012b).

4.2.2 Unique aspects

The unique aspect of this work is the simultaneous measurement of the far-field pressure, enabling analysis of the causal link between the near-field wavepackets and the emitted sound. The measured data are used to establish a relationship between the near-field fluctuations and the far-field pressure by means of correlation analysis and to characterize the wavepacket behaviour in the near field in terms of wavepacket parameters. A Green's function tailored to the geometry of the conical microphone array is used to propagate the recorded near-field wavepacket signatures to the far field using both statistical and time-domain analysis. This method follows the approach of Reba *et al.* (2010), and the statistical calculations used the code already developed and validated by Léon (2012) and Léon & Brazier (2013) for far-field sound estimates from PSE predictions. The time-domain Green's function predictions were obtained by modifying Léon's (2012) code to retain the pertinent information.

4.3 Experimental setup

The experiments were carried out in an anechoic free jet facility with a cut-off frequency of 200 Hz at the *Centre d'études aérodynamiques et thermiques* (CEAT), Institut Pprime, Poitiers, France. Two experimental campaigns obtained measurements in the pressure field generated by a jet with nozzle diameter $D = 50$ mm and Mach numbers in the range $0.4 \leq M \leq 0.6$. The corresponding Reynolds number range was 4.2×10^5 to 5.7×10^5. A carborundum trip placed $2.7D$ upstream of the nozzle lip ensured the boundary layer was turbulent at the jet exit. Both the acoustic far field (Cavalieri *et al.*, 2012a) and the velocity field (Cavalieri *et al.*, 2012b) of this jet have been previously examined, and more details are available in the cited papers. The potential core length of the jet ranged between $5 \leq x/D \leq 5.5$.

In both of the current campaigns, far-field pressure measurements were recorded by

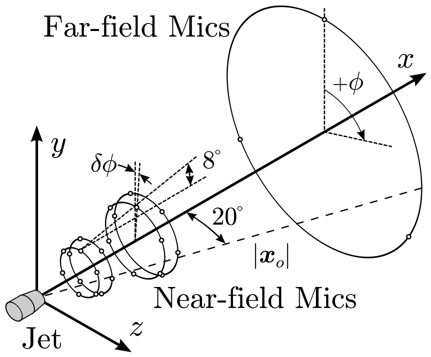

(a) Overview

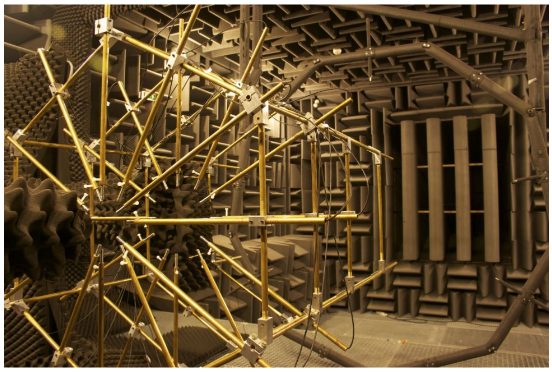

(b) Installed rig

Figure 4.5: Overview of 4-ring setup

Table 4.1: Experiment conditions for both experimental campaigns

Campaign	X/D	$X_{\max}/D$	r_A/D	$\Delta X/D$	M
7 Ring	1.25	5.75	0.8	0.75	$0.4, 0.45, \ldots, 0.6$
	2	6.5	0.7		
	2.75	7.25	0.6		
4 Ring	0.5	8.9	0.8	0.4	0.6

an azimuthal ring array of three equispaced 1/4″ GRAS 40BP microphones at $\theta = 20°$ and $|\mathbf{x}_o|/D = 47.1$. The far-field array was limited to three microphones because the sound field of this jet at $\theta = 20°$ has been shown to be dominated by fluctuations in the axisymmetric mode ($m = 0$, Cavalieri *et al.*, 2012a), making resolution of higher azimuthal modes unnecessary for the Strouhal number range investigated here. The near-field array was made up of a number of azimuthal ring arrays. Azimuthal arrays were used to enable decomposition of the pressure signals into azimuthal Fourier modes, enabling azimuthal mode-by-mode analysis consistent with the azimuthal mode-by-mode calculation of the linear PSE solutions. An overview of the test setup is illustrated in figure 4.5 for one of the campaigns, and the experimental conditions for both campaigns are tabulated in table 4.1.

The focus of the first campaign was a simultaneous measurement of as much of the near field as possible to enable a time-domain comparison to the near-field fluctuations and the far-field sound. To that end the near-field array comprised seven azimuthal rings, each with six microphones distributed azimuthally. A schematic of the setup is given in figure 4.6. There were a total of 42 microphones in the near-field cone. Two types of microphones were used in the near-field array because there was a limited number of high-quality precision microphones available. The first three

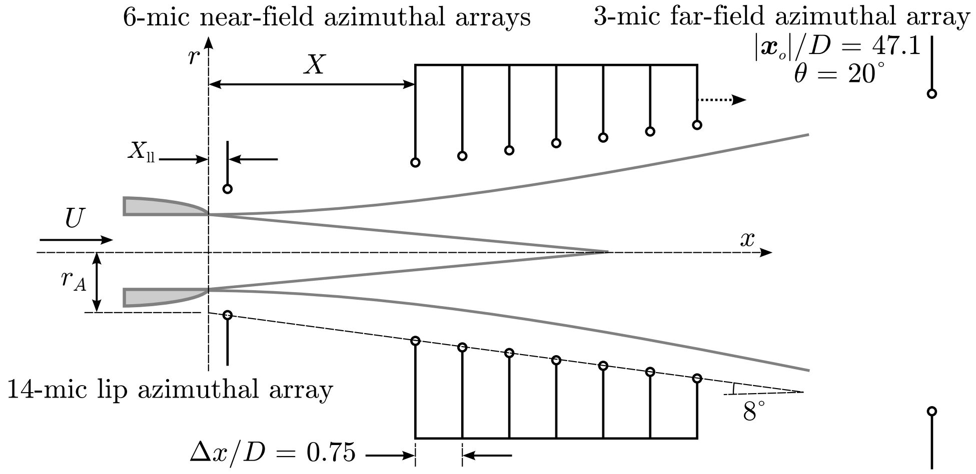

Figure 4.6: 7-ring near-field azimuthal array setup (7pt correlation)

rings used inexpensive 1/4″ electret microphones, while the last four rings used 1/4″ GRAS 40BP precision microphones. The frequency response of the electrets was found to closely match the GRAS microphones up to about 9 kHz (St $\approx$ 2.2 for $M = 0.6$). The half-angle of the cone, $\alpha = 8^\circ$, matched the expansion of the jet so that each microphone measured pressure amplitudes of the same order of magnitude. The conical surface intersected the jet nozzle plane at radial distance labeled r_A, which was set between 0.6 and $0.8D$ depending on the test configuration. The entire array was mounted on a traverse, which allowed the rings to span different portions of the jet near field ranging from X to X_{max}. In this campaign, the radii of the rings were not adjusted when X was changed, meaning that each X corresponded to a different r_A as well as different axial coverage of the jet. Since the axial spacing was $0.75D$, shifting X in multiples of this amount gave measurements at the same axial locations on different conical surfaces, allowing a partial evaluation of the radial decay of the near-field fluctuations. At each axial position, measurements were obtained in the velocity range $0.4 \leq M \leq 0.6$ in increments of 0.05. An additional ring of 14 microphones was included close to the nozzle lip in order to investigate the relationship between nozzle fluctuations and downstream activity. These data have not been examined here.

The second campaign, illustrated in figure 4.7, was designed to provide finer-resolution measurement of the statistics of the near-field fluctuations. This array consisted of four rings of six 1/4″ GRAS 40BP microphones that could be moved independently in the axial direction. This setup does not allow the monitoring of the space–time structure of the near-field pressure, but it does allow the statistical shape and energy of the modes to be determined via two-point correlations, allowing the construction of the Cross-Spectral Matrix (CSM) describing the jet statistics. To ensure that all the measurements fell on the same conical surface ($r_A/D = 0.8$), the

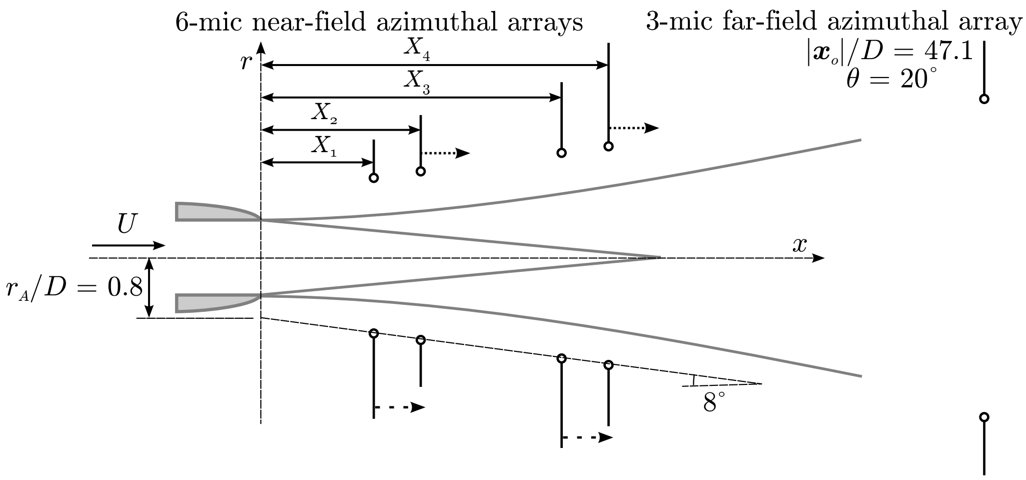

Figure 4.7: 4-ring near-field azimuthal array setup (2pt correlation)

radial positions of the microphones were adjusted every time a ring was moved axially. The use of four rings—instead of the minimum two—simply reduced the number of acquisitions required to span the whole jet length. The final axial resolution of the measurements was $0.4D$, and the measurements were made in the axial range $0.5 \leq x/D \leq 8.9$ for $M = 0.6$. Again, these parameters are summarized in table 4.1.

4.4 Analysis and results

4.4.1 POD mode analysis

First, the pressure signals are decomposed by Fourier series into azimuthal modes and frequency components as

$$\tilde{p}_m(x,t) = \tilde{p}(x,m,t) = \int p'(x,\phi,t)e^{\mathrm{i}m\phi}d\phi, \tag{4.1}$$

$$P_{m,\omega}(x) = P(x,m,\omega) = \int \tilde{p}_m(x,t)e^{-\mathrm{i}\omega t}dt, \tag{4.2}$$

where ω is the angular frequency. Again, for the present results, only the axisymmetric mode ($m = 0$), which has been shown to dominate the low-angle emissions (Cavalieri *et al.*, 2012a; see also § 4.2), is considered. The 2-point CSM, $\mathbf{R}_{m,\omega}(x,x_2)$, is then formed as

$$\mathbf{R}_{m,\omega}(x,x_2) = \langle P_{m,\omega}(x)P^*_{m,\omega}(x_2)\rangle, \tag{4.3}$$

where * indicates complex conjugation, so that the POD problem on the cone surface is represented by the Fredholm integral equation

$$\frac{2\pi}{\cos\alpha}\int \mathbf{R}_{m,\omega}(x,x_2,r,r_2)\xi_{m,\omega}(x,r_2)r_2 dx_2 = \lambda_{m,\omega}\xi_{m,\omega}(x,r), \tag{4.4}$$

with $r = (x - X_0)\tan\alpha$, where X_0 is the virtual origin of the antenna array and α is the cone half-angle. $\lambda^{(i)}_{m,\omega}$ and $\xi^{(i)}_{m,\omega}(x)$ are the eigenvalues and eigenvectors of the matrix $\mathbf{R}_{m,\omega}(x,x_2)$, respectively. The kernel $r_2\mathbf{R}_{m,\omega}(x,x_2,r,r_2)$ is not Hermitian, but following Jung *et al.* (2004) and Cavalieri *et al.* (2012b), it can be made Hermitian by multiplying equation (4.4) by $\sqrt{r}$ and considering the kernel $\sqrt{rr_2}\mathbf{R}_{m,\omega}(x,x_2,r,r_2)$ with the eigenvector $\sqrt{r}\xi^{(i)}_{m,\omega}(x)$. The constant in front of the integral can also be absorbed into the eigenvalues. Now that the kernel is Hermitian and positive semi-definite, the eigenvalues are real and greater than or equal to zero while the eigenvectors are complex-valued. In practice, small errors in the CSM can result in some negative eigenvalues, which are considered to be zero. In the discrete case, the matrix has dimensions $I \times I$, where I is the number of axial observation locations. The calculation is performed separately for each combination of frequency and azimuthal mode. An individual POD mode is obtained by

$$POD^{(i)}_{m,\omega}(x) = \sqrt{\lambda^{(i)}_{m,\omega}}\xi^{(i)}_{m,\omega}, \quad i = 1,\ldots,I. \tag{4.5}$$

By construction, each set $\{\xi^{(i)}_{m,\omega}(x), i = 1,\ldots,I\}$ forms a complete basis for $\tilde{p}_m(x,t)$, but including only those modes for which $\lambda^{(i)}_{m,\omega} > 0$ has the added advantage of reducing the span of the basis to the span of the realizations that were used to create the eigenvectors (Berkooz *et al.*, 1993), forcing all relevant boundary and physical constraints to be met automatically in any reconstruction. Figure 4.8 shows the energy distribution of the various POD modes at selected frequencies obtained with the high-resolution 4-ring array measurements. Most of the energy of the axisymmetric mode (45-65%) is captured in its first POD mode, and this proportion is lowest for higher St. This first POD mode is the focus of the comparison to PSE, but higher POD modes are also considered in the correlation results of §§ 4.4.2 and 4.4.3.

Figures 4.9 and 4.10 compare the PSE predictions of the azimuthal mode with the measured amplitude and phases of both the original signal and the first POD mode for different frequencies. For the current computations, the number of points used in the discrete Fourier transform corresponded to $\Delta\mathrm{St} = 0.1$, which was the same resolution as the PSE predictions, which are taken from Cavalieri *et al.* (2012b). The data from the 7-ring array are also included to show that the same amplitudes and mode shapes are obtained for the coarser-resolution array. The reported amplitudes

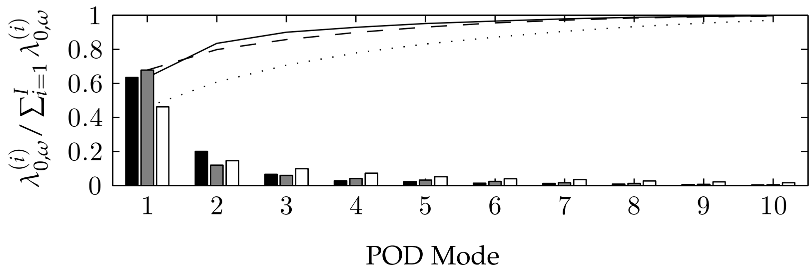

Figure 4.8: Energy distribution (bars) and cumulative sum (lines) for the first 10 POD modes of $P_{m,\omega}$ for $m = 0$ from the 4-ring array measurements. St $= 0.2$ ▬ and ——, St $= 0.5$ ▬ and – – –, and St $= 0.8$ ▭ and ······.

are scaled estimates of $\langle P_{m,\omega}(x) P^*_{m,\omega}(x) \rangle$, and the phases are obtained using

$$\text{Phase angle} = \arg(P_{m,\omega}(x)) - \arg(P_{m,\omega}(x_{\phi\text{ref}})), \tag{4.6}$$

where the phase reference location is $x_{\phi\text{ref}}/D = 2$. The scale factors applied to the PSE amplitudes to match the measurements were obtained already from the hot-wire measurements of Cavalieri *et al.* (2012b); however, it was necessary to apply an additional factor of 10 to the PSE estimates to produce the current plots. The reason for this discrepancy is uncertain, but it likely results from an inconsistency in scaling between the calculation of the hot-wire results and the current results.

In figure 4.9 for all cases, the PSE predictions beyond the end of the potential core underestimate the fluctuation intensity, but for St ≥ 0.3 the first POD mode matches the PSE prediction nearly exactly. For St ≥ 0.7, this agreement breaks down at a distance well beyond the potential core length ($x/D \approx 5$). The coarser 7-ring array also captures this behaviour. For the phase estimates in figure 4.10, the agreement is also striking for St > 0.1. Again, for St ≥ 0.7 there is a breakdown well beyond the potential core, but the agreement is otherwise excellent. The good agreement between the 7-ring and 4-ring measurements in figure 4.10 also shows that the phase response of the electret microphones used in the first three near-field azimuthal rings is sufficient to provide accurate measurements. The implication of this downstream agreement is that linear wavepackets do persist in this region. Since POD is efficient at filtering spatially incoherent fluctuations, the good collapse downstream with just the first POD mode shows that incoherent fluctuations are responsible for the high downstream magnitudes observed before POD is applied. Thus the PSE predictions accurately estimated the coherent part of the fluctuations verifying the presence of linear wavepackets downstream. This is in contrast to the results of Cavalieri *et al.* (2012b) that are reproduced in figure 4.4, particularly in subplot (c), in which the POD did not collapse well to the PSE estimate at $x/D = 8$. A possible explanation for this

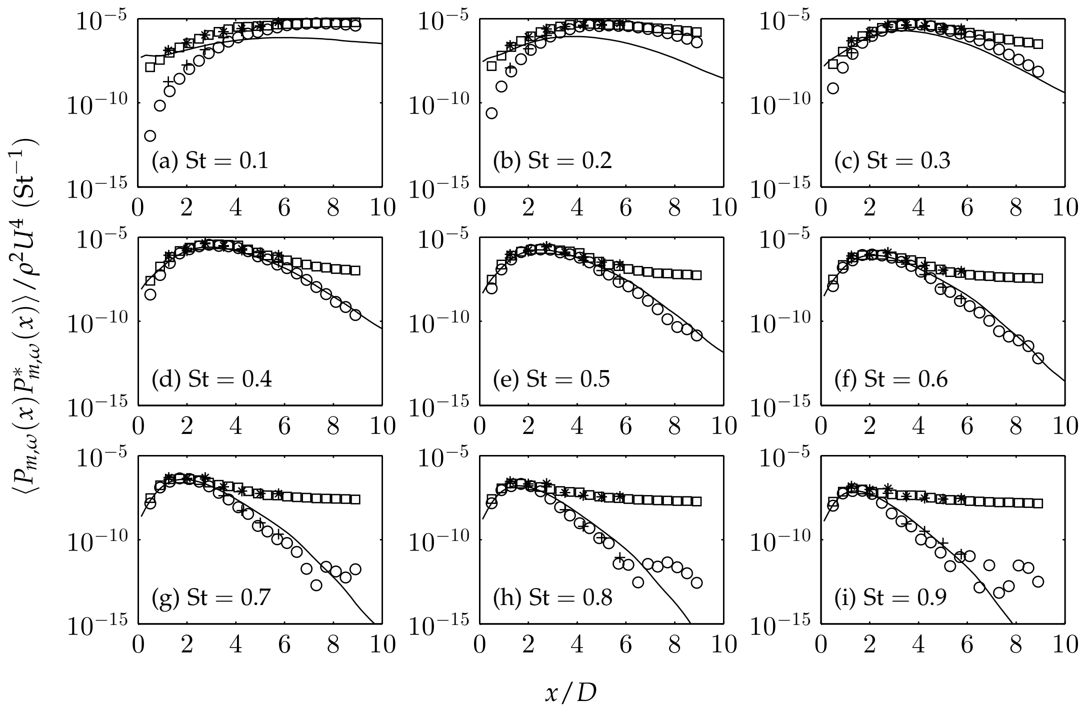

Figure 4.9: Comparison of PSE estimates and measured autospectra magnitudes of $P_{m,\omega}$ for $m = 0$ and $M = 0.6$. ——— PSE, □ 4-ring full signal, ○ 4-ring first POD mode, $*$ 7-ring full signal, + 7-ring first POD mode

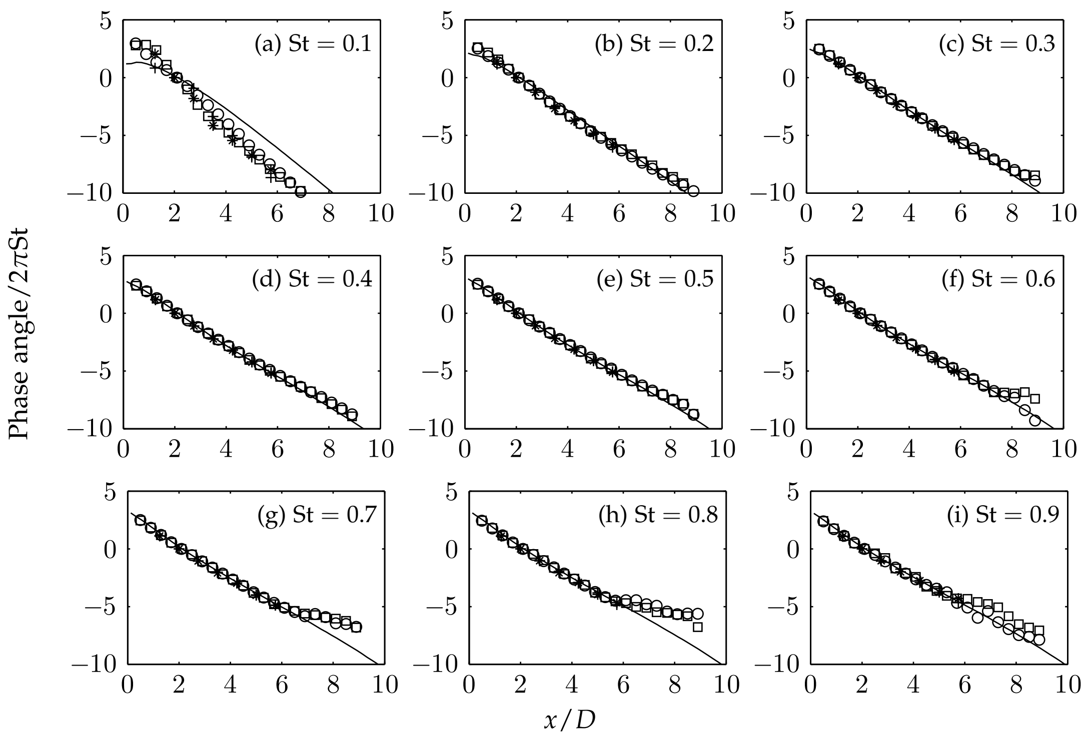

Figure 4.10: Comparison of PSE estimates and measured autospectra phases of $P_{m,\omega}$ for $m = 0$ and $M = 0.6$. Phase reference is $x/D = 2$. See figure 4.9 for legend.

is that the incoherent in-flow velocity fluctuations are much greater than the coherent wavepacket-related fluctuations for POD to efficiently isolate them. This explanation corresponds to Cavalieri *et al.* (2012b) hypothesis H2 reproduced in § 4.2. The current results make it difficult to accept hypothesis H3, because the wavepackets—though not apparent in the velocity field—are still observable in the pressure field measurements.

4.4.2 Projection of time signals onto POD modes

Since the POD modes form a complex-valued orthonormal basis for the measured pressure fluctuations (Berkooz *et al.*, 1993), complex-valued coefficients of each POD mode, $b^{(i)}_{m,\omega}$, can be determined by projecting the Fourier-transformed time signals of the azimuthal coefficients, $P_{m,\omega}(x)$, onto the basis

$$b^{(i)}_{m,\omega} = \int P_{m,\omega}(x)\xi^{(i)*}_{m,\omega}(x)dx. \tag{4.7}$$

A low-order estimate, $\hat{\tilde{p}}_m(x,t)$, of the time-domain signal for an azimuthal mode m can then be formed by the inverse Fourier transform as

$$\hat{\tilde{p}}_m(x,t) = \frac{1}{2\pi}\int \left[\sum_{i=1}^{J} b^{(i)}_{m,\omega}\xi^{(i)}_{m,\omega}(x)\right] e^{\mathrm{i}\omega t}d\omega, \tag{4.8}$$

where $\hat{\tilde{p}}_m(x,t) = \tilde{p}_m(x,t)$ when $J = I$ or at least the number of $\lambda^{(i)}_{m,\omega} > 0$. For discrete computations, equations (4.7) and (4.8) can be applied sequentially to blocks of data where the number of points in each block should be the same as in equation (4.2). For consistency, when calculating ensemble averages with the reconstructed data, the blocks should be the same as in the reconstruction.

In principle, for a full time-domain reconstruction using a particular POD basis, it is necessary to have simultaneous measurements at all the original ring locations used for obtaining that basis. This means that a time-domain decomposition of all 22 POD modes available (per azimuthal mode) using the 4-ring array is not possible, and only statistical information is available. However, since the 7-ring and 4-ring setups measure the same jet, the POD modes are the same and the 7-ring data can be projected onto the higher resolution basis. To determine $b^{(i)}_{m,\omega}$, the 4-ring basis must be re-sampled at the same locations as the 7-ring data. Both the re-sampled basis and the original basis should be scaled by the same factor such that $|\xi^{(i)}_{m,\omega}(x)| = 1$ for the re-sampled basis. This rescaling ensures that fluctuation energy is conserved—barring small errors—in the projection. In practice, since the 7-ring data have fewer degrees of freedom and modes higher than 7 will be aliased into the lower modes causing discrepancies in the modes obtained by 4-ring and 7-ring arrays, this technique is only valid to the extent that the obtained POD modes have the same shape. Figure 4.11 shows that this is valid over the frequency range of interest for the first POD mode and that the validity is reasonable but deteriorating for the next two POD modes. These modes account for nearly all of the flow energy as indicated by figure 4.8. Figure 4.12 shows an example of the reconstruction for $m = 0$ using just the first POD mode in comparison to the full 7-ring signal in retarded time coordinates to align with the far-field pressure. For the POD reconstruction in figure 4.12, the block size for the Fourier transform was $N = 2440$ points ($\Delta \mathrm{St} = 0.01$).

The resulting space–time plots are presented in figure 4.12 as a comparison between the raw 7-ring full signal and the projection using POD mode 1. Also plotted is the far-field $\hat{p}_0$ as a line plot in subplot (a). The time scale is plotted as retarded time $\tau_r = \tau - |\mathbf{x}_o - \mathbf{x}_s|/c_0$ so that the far-field signal fluctuations are aligned with the fluctuations that are expected (by a first estimate) to have caused them. Here τ is measured from an arbitrary reference time within the signal.

In evaluating the effectiveness of the projection, the striking feature of the plots in figure 4.12 to consider is the similarity between subplots (b) and (c). Visually, the first POD mode estimate captures all the salient dynamics of the full signal. The difference is that the projection has a higher spatial resolution, and—as can be seen in subplot (d)—it spans a greater spatial extent than the recorded signal, which is a direct result of the basis used in the projection. Within the span covered by the 7-ring basis, all the peaks and troughs of the signal align in the two plots and have the same magnitude. Statistically the agreement between these two signals is expected to be as good as the agreement in figure 4.9 between the full signal and POD mode 1 curves. Knowing this, it is expected that beyond the end of the potential core, the POD mode 1 signal will deviate significantly from the full signal in the same manner that it does statistically in figure 4.9. The projection could also be performed onto the PSE basis, for which the result is expected to be similar.

Beyond simply evaluating the projection technique, the results in figure 4.12 highlight the wavepacket structure of the near pressure field, which is not only present statistically—as previously shown by Suzuki & Colonius (2006) and Tinney & Jordan (2008)—but also in the time domain. This is clear from interpreting the features of the POD subplot. Clearly visible is a dominant feature that oscillates regularly and convects in the jet. The amplitude rises (growth region), levels out (saturation region), and decreases (decay region) beyond the potential core. This is the expected behaviour of a wavepacket. Also of great interest is the fact that the wavepacket parameters do not stay constant throughout the time signal. Though the convection speed seems relatively constant, the wavepacket amplitude and spatial extent fluctuate intermittently. This indicates that intermittency may indeed be important in wavepacket sound predictions.

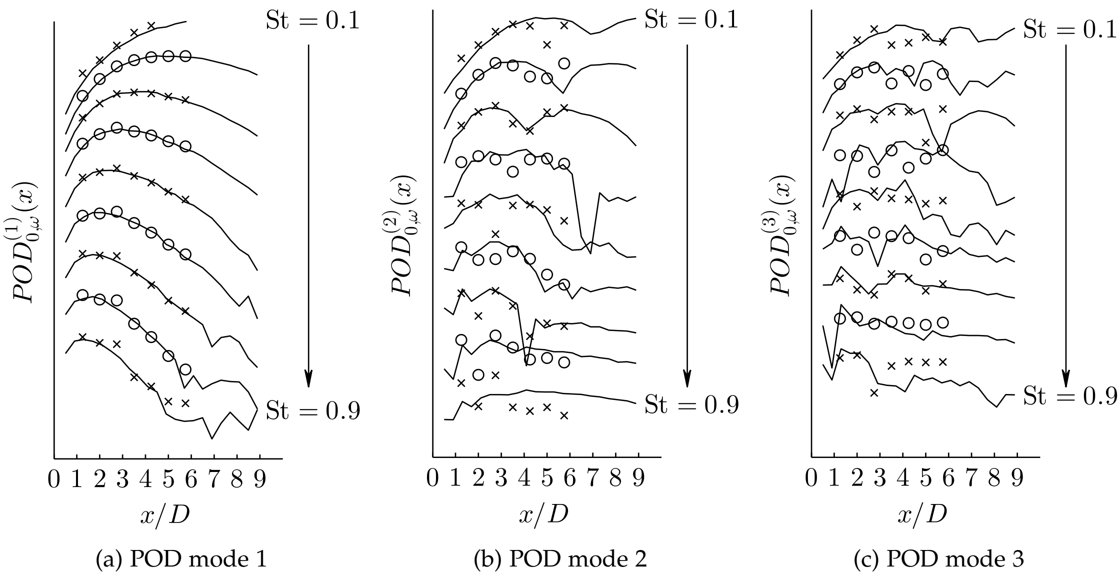

Figure 4.11: $m = 0$ POD modes of $P_{m,\omega}$ for 4-ring (———) and 7-ring ($\times$ and $\bigcirc$) setups. Arbitrary scaling between St.

This result has been considered theoretically by Cavalieri *et al.* (2011), and this serves as corroborating experimental evidence in a subsonic jet.

4.4.3 Near-field–far-field correlation

Figure 4.13 shows the normalized cross-correlation, $R_{\tilde{p}_{NF}\tilde{p}_{FF}}/\sigma_{\tilde{p}_{NF}}\sigma_{\tilde{p}_{FF}}$, between the axisymmetric modes for the near-field and far-field signals ($\tilde{p}_0$). As in § 4.4.2, all the correlation plots shown here are plotted with respect to the retarded time lag, $\tau_r = \tau - |\mathbf{x}_o - \mathbf{x}_s|/c_0$, accounting for an estimated sound propagation time to the observation location. In the case of the correlations, τ is the correlation time tag. The extended nature of the peak signature indicates that the flow phenomena related to sound production are correlated over a large spatial extent (see chapter 3). If such a phenomenon also has high energy compared to other flow fluctuations, it should be detectable in the POD modes. The correlation between the reconstructed POD modes and the far field can indicate if POD efficiently collapses the sound-producing phenomena. If the correlation for any particular mode is significantly higher than the baseline correlations in figure 4.13, then that mode is a good candidate for a sound generation mechanism and a possible target for control schemes. If the correlation magnitudes are similar across all POD modes, then POD—while being optimal in terms of energy in the near field—is inefficient for isolating sound-producing fluctuations. Since the first POD mode was shown in § 4.4.1 to be nearly equivalent to the PSE prediction, the correlation between the first POD mode and the far field also

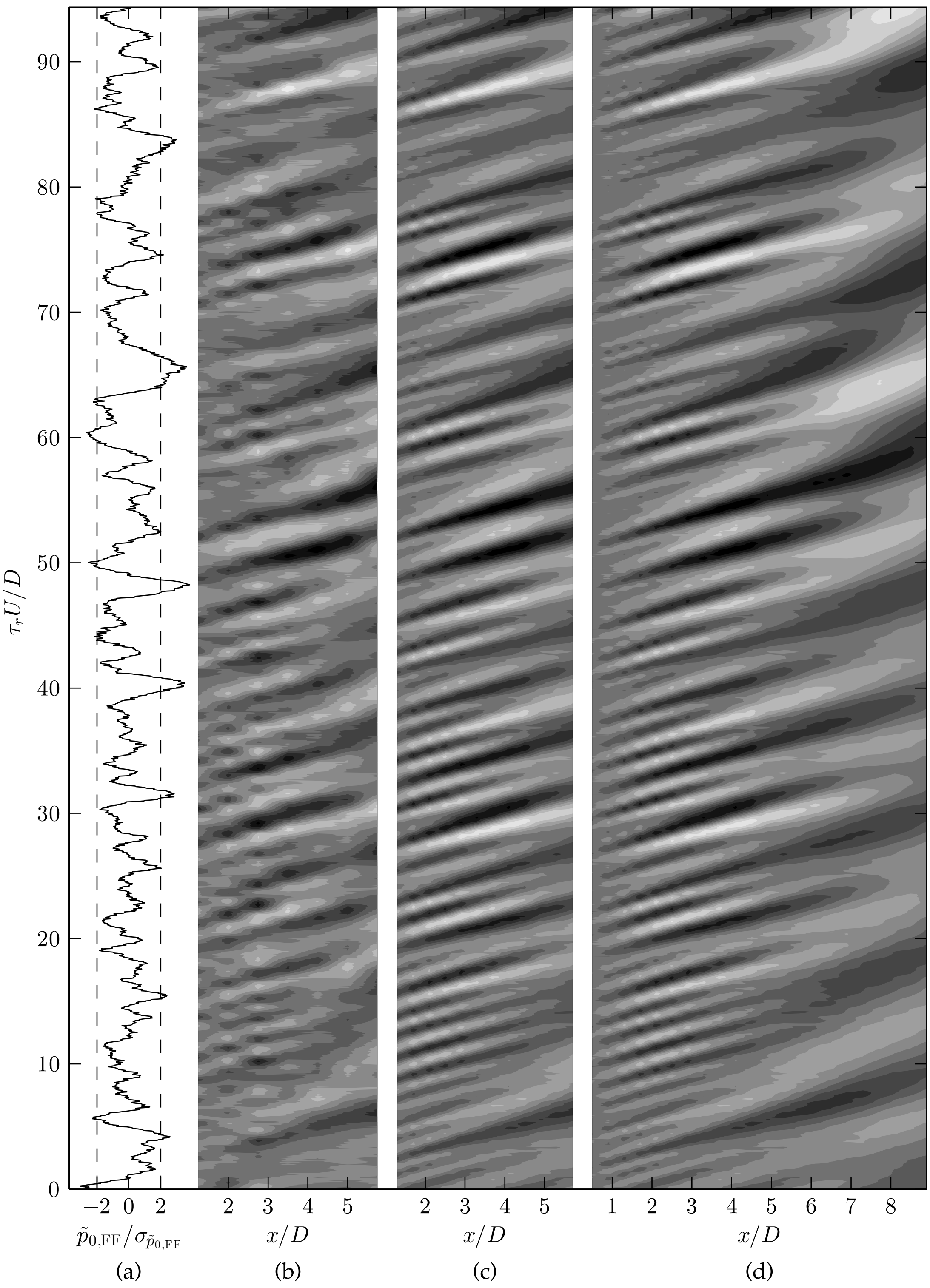

Figure 4.12: Comparison between near-field and far-field $m = 0$ pressure mode signals ($\tilde{p}_m$) for both full signal and POD reconstruction. (a) Far-field signal plotted with $\pm 2\sigma$ to show peaks, (b) full 7-Ring near-field signal, (c) projection to POD mode 1 of the 4-ring basis truncated to 7-ring axial extent, and (d) projection to POD mode 1 of the 4-ring basis.

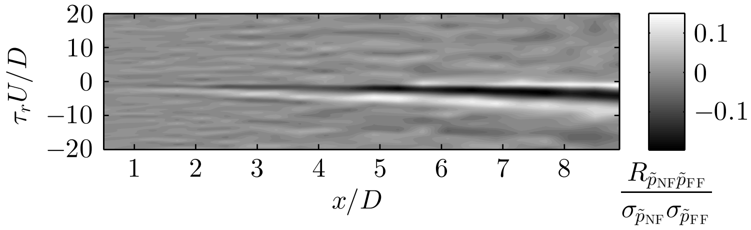

Figure 4.13: Normalized retarded correlation between near-field $\tilde{p}_0$ and far-field $\tilde{p}_0$

constitutes a correlation between a time-domain projection of the near-field array onto the wavepacket model and the far-field pressure. If this correlation is significantly higher than the full signal correlation, then this projection is a suitable denoising method to remove fluctuations uncorrelated to the far field and it provides strong evidence that wavepackets are the main source of sound at $\theta = 20°$.

With the current data, the correlation can be made directly with both the 4-ring and 7-ring data for the full $\tilde{p}_m(x,t)$ for each azimuthal mode, but only the axisymmetric azimuthal mode is shown here. For the 7-ring data, the contributions of the POD modes to the near-field–far-field correlation are presented in figures 4.14 and 4.15 for the individual modes and the cumulative modes, respectively. Figure 4.15(g) corresponds to the full correlation with $\tilde{p}_0(x,t)$, which is consistent with figure 4.13. For the 4-ring data, this POD-mode-by-POD-mode correlation for all POD modes is impossible because not all axial locations were recorded simultaneously. However, using the reconstruction method of § 4.4.2, the 7-ring data were projected to the 4-ring POD modes, allowing the higher-resolution, longer axial extent correlations to be estimated. Figures 4.16 and 4.17 show these POD mode correlations both individually and cumulatively for the first three POD modes using this projection.

Figure 4.16(a) is nearly identical to the full correlation result plotted in figure 4.13, which shows that the first POD mode captures the salient correlation features. Interestingly, the correlations for the other modes show different space–time structures than for the first mode. However, this should not be considered evidence of independent sound generation mechanisms because the POD reconstruction includes a wide range of frequencies, over which it is unlikely that such concerted fluctuations occur in both time and space. Rather, the various correlation features of the higher modes may be better described as coherent deviations from the underlying coherent wavepacket structure. It is unclear why these deviations are as well-correlated to the far-field sound as the POD mode, so this result is rather inconclusive. Either the wavepacket model fails to denoise the non-sound-related fluctuations, or the components of the signal that do not fit well with the wavepacket model (St < 0.3 and possibly St > 0.9) affect the correlation result here. Another possible explanation is that the higher

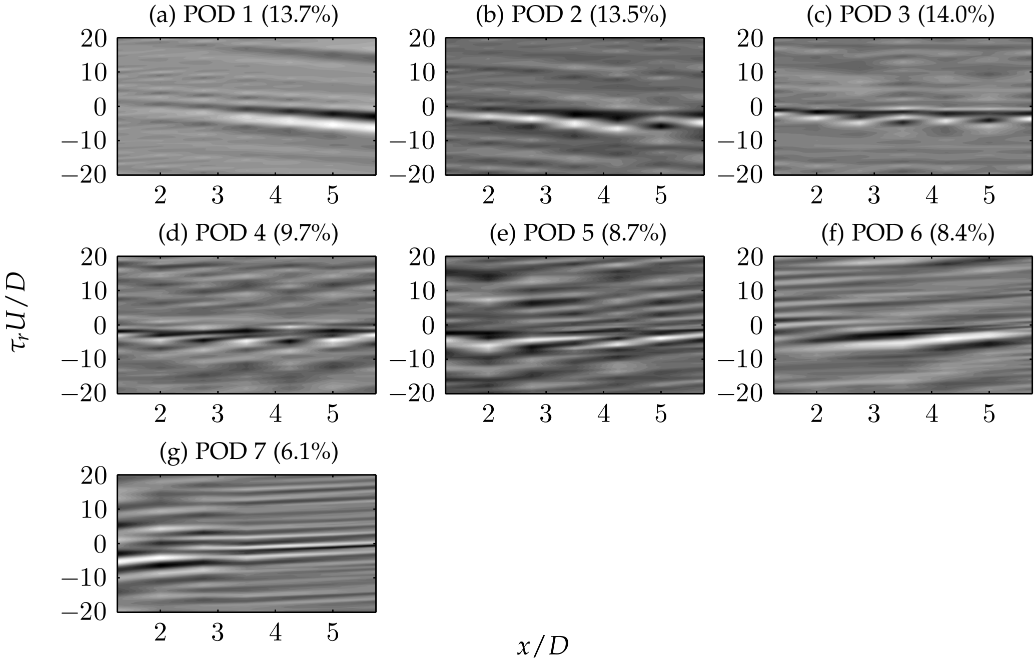

Figure 4.14: Individual $m = 0$ POD mode contributions to near-field–far-field correlation ($R_{\tilde{p}_{\mathrm{NF}}\tilde{p}_{\mathrm{FF}}}/\sigma_{\tilde{p}_{\mathrm{NF}}}\sigma_{\tilde{p}_{\mathrm{FF}}}$) for 7-ring data. The absolute maximum for each subplot is indicated in brackets.

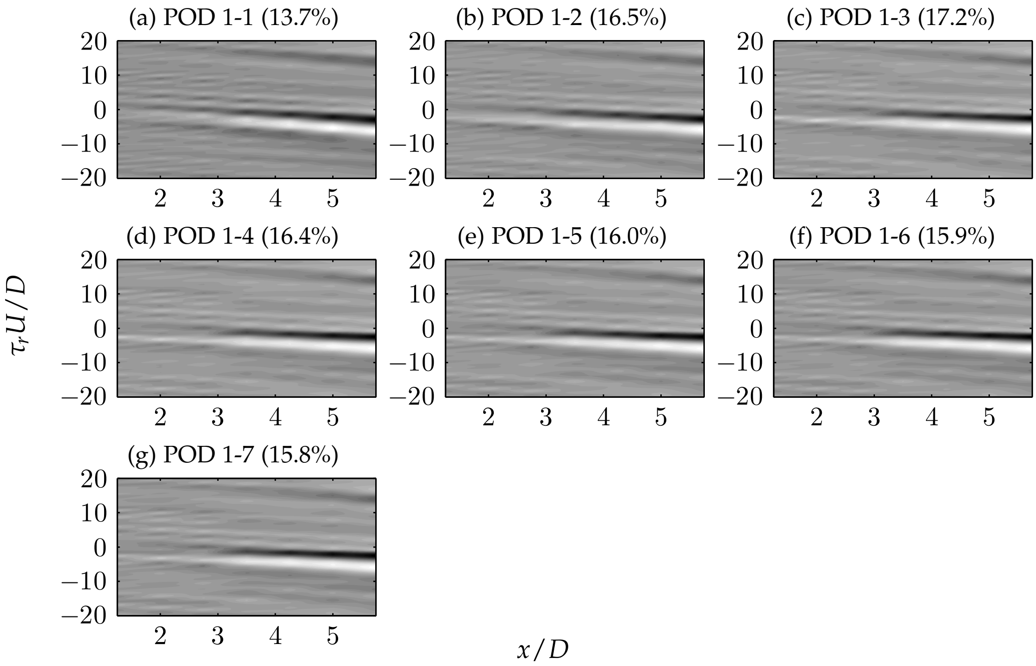

Figure 4.15: Cumulative $m = 0$ POD mode near-field–far-field correlations ($R_{\tilde{p}_{\mathrm{NF}}\tilde{p}_{\mathrm{FF}}}/\sigma_{\tilde{p}_{\mathrm{NF}}}\sigma_{\tilde{p}_{\mathrm{FF}}}$) for 7-ring data. The absolute maximum for each subplot is indicated in brackets.

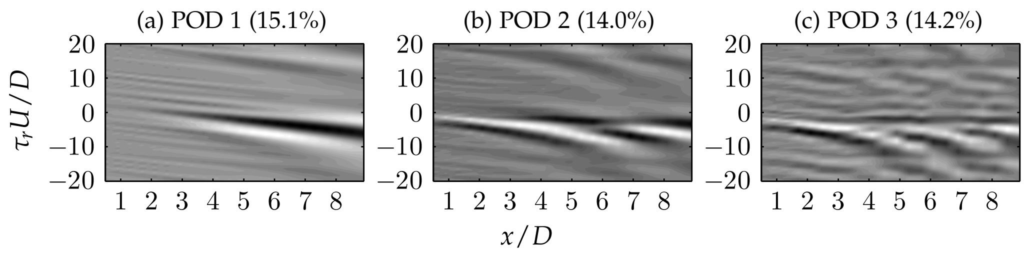

Figure 4.16: Individual $m = 0$ POD mode contributions to near-field–far-field correlation ($R_{\tilde{p}_{NF}\tilde{p}_{FF}}/\sigma_{\tilde{p}_{NF}}\sigma_{\tilde{p}_{FF}}$) for the reduced-order projection using equation (4.8). The absolute maximum for each subplot is indicated in brackets.

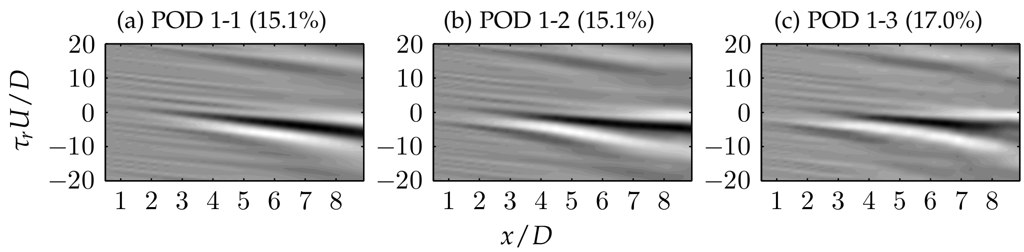

Figure 4.17: Cumulative $m = 0$ POD mode near-field–far-field correlations ($R_{\tilde{p}_{NF}\tilde{p}_{FF}}/\sigma_{\tilde{p}_{NF}}\sigma_{\tilde{p}_{FF}}$) for the reduced-order projection using equation (4.8). The absolute maximum for each subplot is indicated in brackets.

POD modes are capturing jitter about the first POD mode because jitter has been shown to have an impact on the efficiency of wavepacket sources (Cavalieri *et al.*, 2011). Regardless of the specific explanation, a single POD mode is insufficient to extract all the acoustically important fluctuations in the flow.

4.4.4 Far-field predictions from near-field wavepackets

4.4.4.1 Formulation for statistical predictions

Reba *et al.* (2010, 2012) showed, by changing coordinates to a spherical system $(\mathcal{R}, \Theta, \varphi)$ centred at the virtual origin of the conical array, that it is possible to write the far-acoustic field due to a pressure distribution on the near-field conical surface as

$$P_{m,\omega}(\mathcal{R}_o, \Theta_o) = 2\pi \sin\alpha \int_0^\infty P_{m,\omega}(\mathcal{R}, \alpha) \frac{\partial g_{m,\omega}}{\partial \Theta}(\mathcal{R}, \alpha; \mathcal{R}_o, \Theta_o) d\mathcal{R}, \tag{4.9}$$

where $g_{m,\omega}$ is a tailored Green's function for the reduced wave equation and the subscript o indicates the observer coordinate location. Reba *et al.* (2010, 2012) continued with equation (4.9) to write the autospectral density of the far-field pressure as

$$\langle P_{m,\omega}(\mathcal{R}_o,\Theta_o)P^*_{m,\omega}(\mathcal{R}_o,\Theta_o)\rangle = 4\pi^2\sin^2\alpha \times \iint_0^\infty \mathbf{R}_{m,\omega}(\mathcal{R}_1,\mathcal{R}_2)\frac{\partial g_{m,\omega}}{\partial\Theta}(\mathcal{R}_1,\alpha;\mathcal{R}_o,\Theta_o)\frac{\partial g^*_{m,\omega}}{\partial\Theta}(\mathcal{R}_2,\alpha;\mathcal{R}_o,\Theta_o)d\mathcal{R}_1 d\mathcal{R}_2, \quad (4.10)$$

which gives the far-field SPL. A brief validation of this statistical prediction technique is presented in appendix B.1 alongside a validation of the time-domain prediction technique introduced below. Their predictions fit well with experimental data for high-speed ($M \approx 1.6$) jets up to about $\theta < 45°$ at $\mathrm{St} = 0.25$, but the results were significantly worse for slower jets ($M \approx 0.9$) and higher frequency ($\mathrm{St} \geq 0.40$). This may be because wavepackets are not the dominant sound source for the lower-Mach-number jets, but another possible explanation is a Mach-number-dependence of the experimental limitations of the setup, a point considered in detail in § 4.4.4.3 and appendix B.2.

4.4.4.2 Formulation for time-domain predictions

Though the statistical prediction technique has been used before, a prediction of the time-domain far-field pressure has not been attempted by any investigators. Taking the inverse Fourier transform of equation (4.9) gives

$$\tilde{p}_m(\mathcal{R}_o,\Theta_o,t) = \int P_{m,\omega}(\mathcal{R}_o,\Theta_o)e^{\mathrm{i}\omega t}d\omega, \quad (4.11)$$

which is the time-resolved far-field pressure mode. In conjunction with the POD mode projection of § 4.4.2, this technique can give time-domain far-field predictions from near-field microphone measurements. To implement this with discrete data, equation (4.9) must first be solved for every frequency for the number of Fast Fourier Transform (FFT) points, N, used to calculate $P_{m,\omega}(\mathcal{R}_o,\Theta_o)$, which allows the Inverse FFT (IFFT) to be applied. In practice, for each far-field observation location, the signal at each time step is dependent on a number of time steps in the near field. Based on causality, since the fluid everywhere outside of the array cone is quiescent, the contribution from each near-field location takes $\tau = |\mathbf{x}_o - \mathbf{x}_s|/c_0$ to arrive, making each far-field point dependent on a duration of data equal to $\tau_{\max} - \tau_{\min}$, where $\tau_{\min}$ and $\tau_{\max}$ are the minimum and maximum propagation times, respectively, from locations on the array with significant contribution to the far field. So in practice, the number of valid time-series points is limited by the physical layout of the array and far-field observer because the discontinuity at the edge of the FFT window causes an error in the far-field prediction. Since the propagation distances are finite (see figure 4.18) and the sound speed is constant in the ambient fluid, the number of affected points is

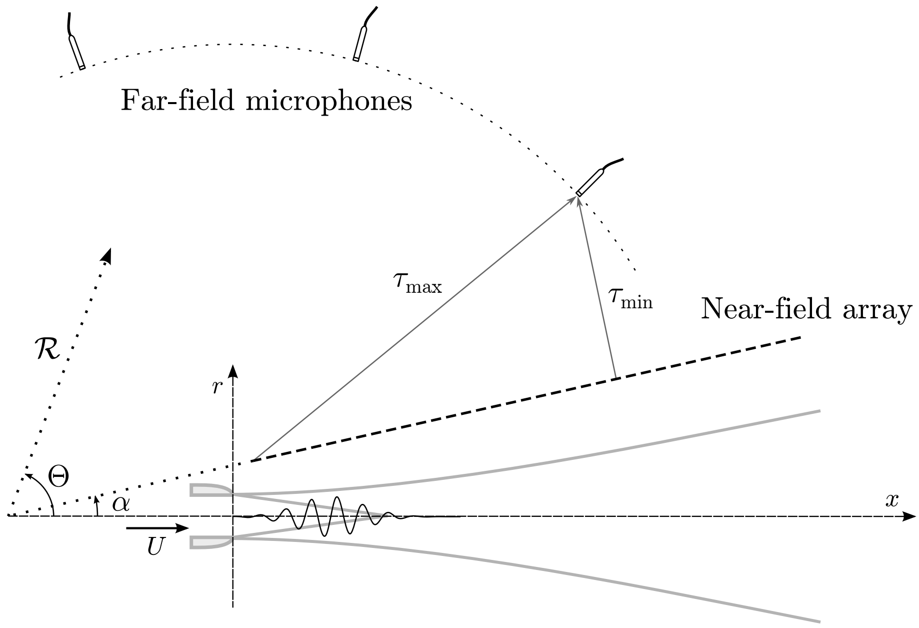

Figure 4.18: Geometric considerations for time-domain predictions with a finite-window Fourier transform

limited, and the number of valid points can be estimated by

$$N_{\text{Valid}} = N - (\tau_{\max} - \tau_{\min}) f_s. \tag{4.12}$$

When calculating a long time series, the series can be broken into blocks, and overlapping the blocks by at least $N - N_{\text{Valid}}$ points overcomes the issue of corrupted points. A validation of the procedure and details of the implementation are presented in appendix B.1.

4.4.4.3 Evaluation of experimental limitations

Since the experimental near-field array's axial extent is limited to $0.5 \leq x/D \leq 8.9$, the predictions with the real data have an additional source of error. To estimate the effect of this spatial truncation, a validation problem, described in appendix B.1 was investigated where only those near-field locations falling in $0.5 \leq x/D \leq x_{\max}$ were used in the calculation. Figure 4.19 shows that the choice of $x_{\max}$ has a major effect on the predicted directivity by making calculations for $x_{\max}/D = 8.9$, 20, and 30. For reference, the result for $X_0/D \leq x/D \leq 70$ is also plotted. A direct interpretation of this result would imply that for accurate predictions at least a $20D$ array is necessary, which would be surprising because the decay of fluctuation energy beyond the potential core is rapid, and the fluctuations well beyond the end of the potential core are not expected to contribute greatly to the far-field sound.

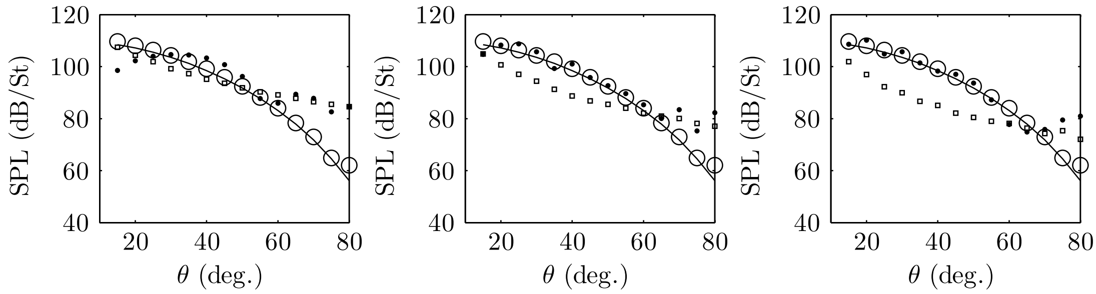

(a) $x_{\max}/D = 8.9$ (b) $x_{\max}/D = 20$ (c) $x_{\max}/D = 30$

Figure 4.19: Effect of experimental near-field array truncation on the statistical far-field Green's function prediction. ——— Lighthill solution and Green's function solutions with ○ $X_0/D \leq x/D \leq 70$, • $X_0/D \leq x/D \leq x_{\max}/D$, and □ $x_{\max}/D \leq x/D \leq 70$ array extents.

However, a more likely explanation is that the sudden source truncation creates a spurious, highly localized source at the array cut-off that is highly correlated with the true wavepacket source. The occurrence of this source is analogous to the Gibbs phenomenon in signal processing, in which an abrupt truncation of a signal causes ringing in its Fourier representation. The interaction between this spurious source and the wavepacket would result in both constructive and destructive interference yielding both underprediction and overprediction of the emissions at different angles, a result consistent with figure 4.19. The strongest evidence for this is in figure 4.19(a), where for high θ, both the results for $X_0/D \leq x/D \leq x_{\max}/D$ and $x_{\max}/D \leq x/D \leq 70$ overpredict the directivity by ≈ 20 dB while both together give the correct result. This is only possible if the two solutions are highly correlated and interfere destructively. Further evidence for this explanation is provided by comparing the prediction at $\theta = 20^\circ$ in figure 4.19(a) for the $X_0/D \leq x/D \leq x_{\max}/D$ array—for which the error is ≈ 6 dB—to the time-domain prediction in figure 4.20(a), where although the amplitude is greatly underpredicted, most of the phase information is still correctly predicted in time domain; that is, the peaks and troughs of the signal are still roughly aligned. This raises the question of how to quantitatively evaluate how 'similar' two time-domain signals are, and whether a definition of 'similar' can be developed that best aids the evaluation of noise source modelling schemes. A first step in this direction is developed in chapter 5.

To better understand this error, the time-domain solution was also calculated for observation locations composing a plane surrounding the abrupt termination of the array at $x_{\max}/D = 8.9$ and extending toward the $\theta = 20^\circ$ observer. These results are presented in figure 4.21. The solid line shows the extent of the near-field array used in the Green's function calculation while, for reference, the dashed line is drawn from the

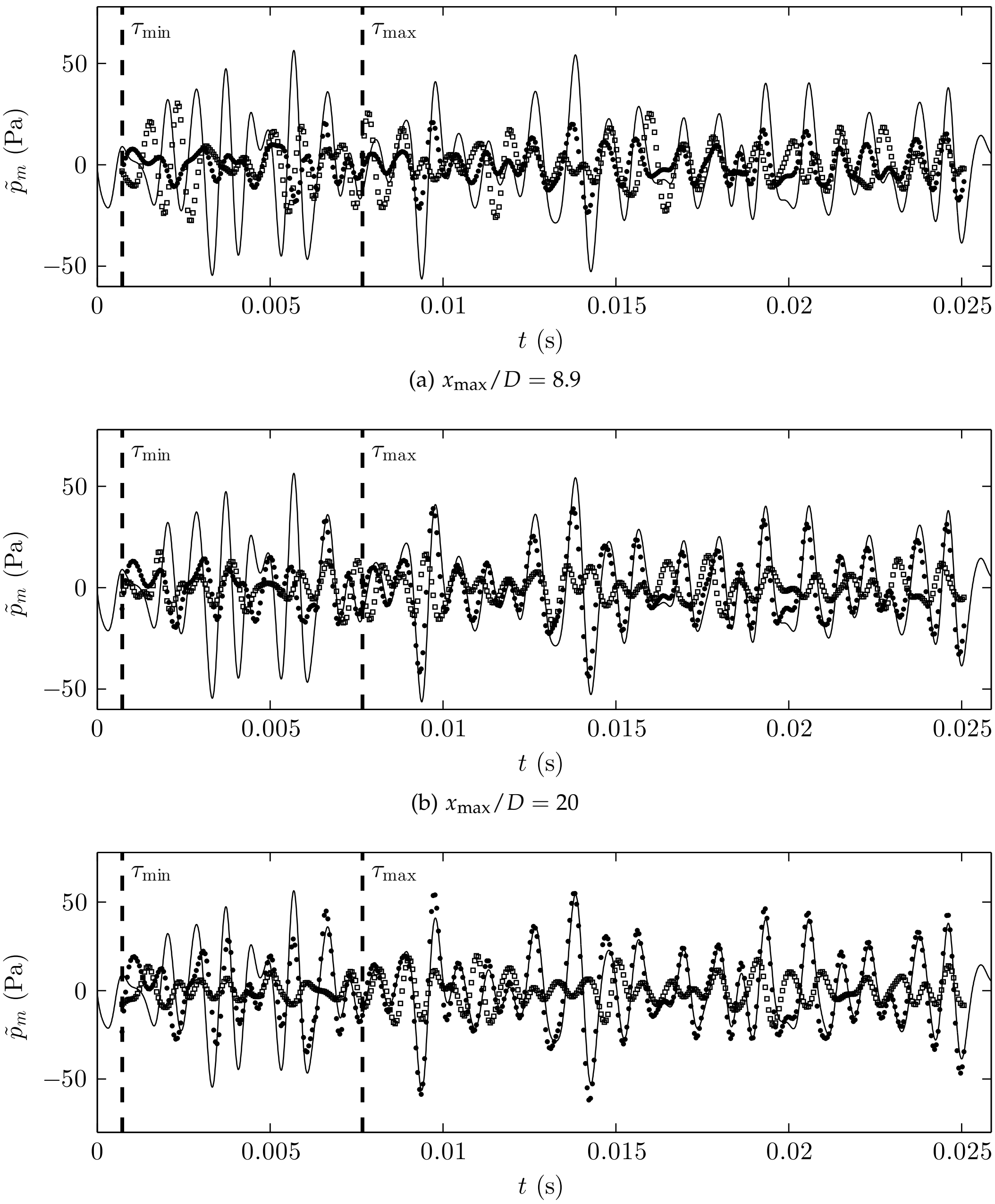

(a) $x_{\max}/D = 8.9$

(b) $x_{\max}/D = 20$

(c) $x_{\max}/D = 30$

Figure 4.20: Effect of experimental near-field array truncation on the time-domain far-field Green's function prediction at $\theta = 20°$. ——— Lighthill solution and Green's function solutions with • $X_0/D \leq x/D \leq x_{\max}/D$, and □ $x_{\max}/D \leq x/D \leq 70$ array extents. Every fifth Green's function data point is shown, and the data between the lines denoted by $\tau_{\min}$ and $\tau_{\max}$ are known to be invalid based on equation (4.12).

jet origin to the far-field observer at $\theta = 20^\circ$. The snapshots were taken at $t = 0.013$ s corresponding to the scale on figure 4.20(a).

In figures 4.21(a) and (b), as expected, there is no discernible difference between the Lighthill solution and the full-array Green's function solution. However, the truncated-array solution in subplot (c) shows a significant change in the directivity. Beginning at the abrupt end of the near-field array and extending into the far field, there is a significant underprediction of the signal amplitude along the direction of the near-field array ($\Theta = \alpha$). Despite the underprediction of the amplitude, the phase of the signal is still roughly the same, which is consistent with the observed peak and trough alignment in figure 4.20 mentioned above. The nature of the error is better apparent in figure 4.21(d), which shows the deviation of the truncated-array prediction from the Lighthill solution. This deviation is a visual representation of the spurious 'source' hypothesized above. A careful investigation of this error shows that it radiates radially with non-uniform directivity from the array cut-off point and is highly correlated to the wavepacket signal. To make this apparent, a visual approximation of the emission pattern has been superimposed on subplots (b) and (d), clearly indicating radial emission. The cancellation is near-perfect along $\Theta = \alpha$ because of the radial emission pattern, but since this pattern is different than the true source's emission pattern, the cancellation rapidly weakens as Θ changes. At certain emission angles ($\theta > 60^\circ$ according to figure 4.19), this source dominates the true source.

It should be noted that Reba *et al.* (2010) overcame the truncation limitation by modelling the axial decay of the CSM beyond the experimental array. This was also attempted with these data (see appendix B.2), but even after testing several models for the wavepacket decay, no significant improvement to the predictions was achieved. This is despite the fact that Reba *et al.*'s (2010) predictions were accurate at least for low θ and low St. The difference here seems to be the much lower Mach number in this case. Reba *et al.*'s (2010) best agreement was for $M = 1.6$, and at $M = 0.9$ the errors were much more significant. In the context of the described spurious-source explanation of the truncation effect, the effect of the spurious source at the array edge is less noticeable because, for a higher-Mach-number jet, the upstream source is more efficient due to the fact that more of the fluctuations reside in the supersonic portion of the wavenumber–frequency spectrum (Jordan & Colonius, 2013; see § 4.1.3). A fuller discussion of the CSM modelling process used here, and the effect of the chosen model as well as Mach number and r_A on the predictions is presented in appendix B.2. The results of this analysis also indicate that for higher-Mach-number jets, accurate predictions are available even without treating the problem of near-field array truncation.

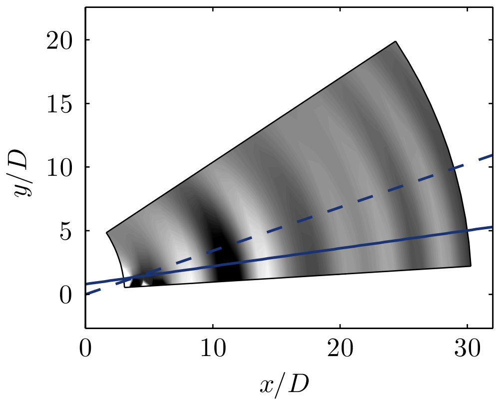

(a) Lighthill solution ($\tilde{p}_{0,\mathrm{LH}}$)

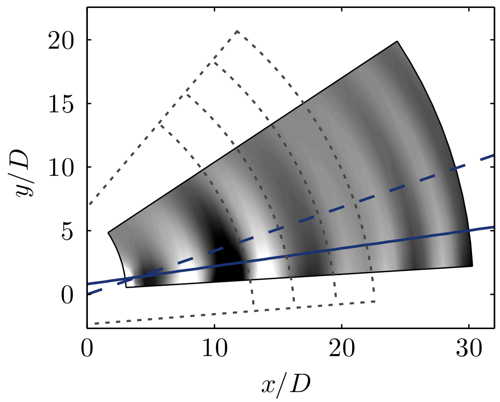

(b) Full-array solution ($\tilde{p}_{0,\mathrm{GF},70D}$)

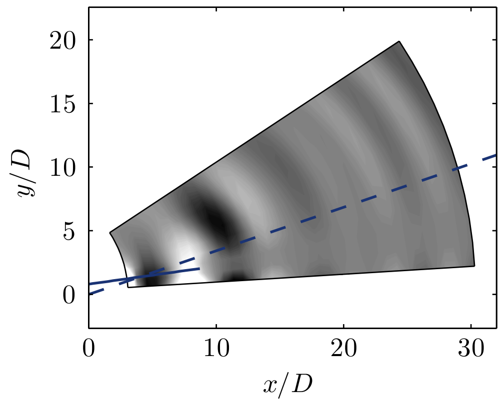

(c) Truncated-array solution ($\tilde{p}_{0,\mathrm{GF},8.9D}$)

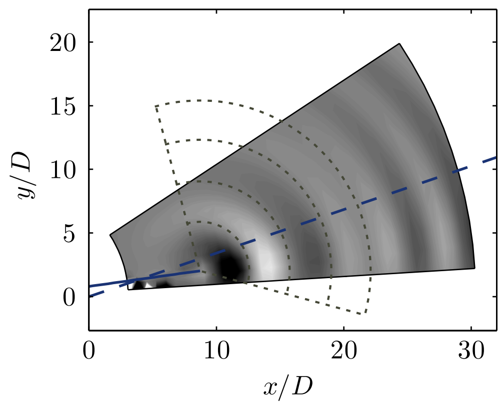

(d) Truncated-array error ($\tilde{p}_{0,\mathrm{LH}} - \tilde{p}_{0,\mathrm{GF},8.9D}$)

Figure 4.21: Snapshot comparison between Lighthill integral solution (subscript LH) and Green's function prediction (subscript GF) for wavepacket sound emissions with a truncated near-field array (x_{max} indicated in subscript). —— Near-field array extent, – – – $\theta = 20°$ (for reference), and ········ approximate radiation pattern.

The observed spurious source is sufficient to explain the error observed in this prediction technique for the validation problem, but a prescription to eliminate the error is not as straightforward. It may be possible to apply an amplitude dampening to the data close to the end of the array to reduce the sharpness of the cut-off and potentially the strength of the spurious source. Whether or not this is possible without significantly affecting the calculated emissions of the true source is unclear, and addressing this issue may be a worthwhile pursuit for future work, but developing this is beyond the scope of this work.

The other experimental factors tested were the axial spacing of the microphone rings, $\Delta x/D$ (0.4 in the experiments); the first microphone ring location, $X_{\min}/D$ (0.5 in the experiments); and the initial radius of the conical array, r_A/D (0.8 in the experiments). For values close to the experimental parameters, none had a significant effect on the results. In fact, for all $\Delta x/D \lesssim 1.2$ and St < 0.7, the results were practically identical, meaning that a sparser microphone experimental array would be practical. Beyond this limit, the directivity was erroneously predicted, particularly for higher St and higher θ. However, within the range of parameters to be expected in various experimental setups, it seems that the only significant limitation is that of the finite axial extent of the near-field array. Future work should be focused on how to overcome this challenge.

4.4.4.4 Application to experimental data

The directivity results for the 4-ring data are compared to the data measured previously for this jet by Cavalieri *et al.* (2012b) in figure 4.22. Clearly, the Green's function predicted directivity is not accurate for any of the CSM representations. Across all frequencies the full-data prediction is closest in terms of magnitude, but it still does not fit the experimental directivity. Using just the PSE or first POD mode shape reduces the prediction by as much as 20 dB over all angles, a level of error that is surprising. This effect could be attributed to either the large difference in fluctuation magnitude beyond the potential core between the full data and the POD and PSE shapes (see figure 4.9) or the effect of a non-unit coherence off the main diagonal of the CSM for the full data. A non-unit coherence could be caused by intermittency (jitter) in the flow as discussed in § 4.1.3. In fact non-unit coherence is one key difference between the experimental data and the validation problem. Though figures 4.9 and 4.10 indicate there is very little difference in the CSM between the first POD mode and PSE, there is still a significant deviation in the directivity in figure 4.22(b), indicating the prediction is sensitive to small deviations in the CSM. Were a suitably accurate prediction available with the experimental data, it would be possible to test the effect of non-unit coherence or the use of single POD modes directly, but the predictions

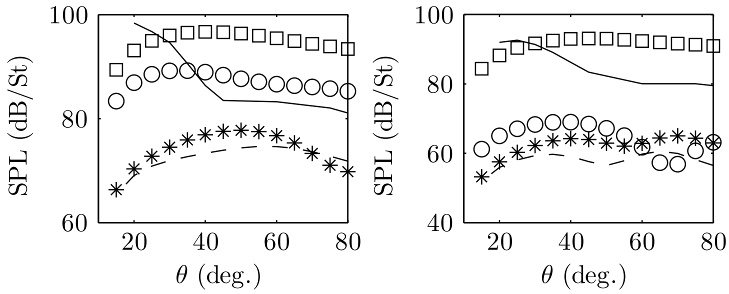

(a) St = 0.2 (b) St = 0.5 (c) St = 0.8

Figure 4.22: Comparison of Green's-function-predicted directivities from the current 4-ring measurements. □ Full prediction, ○ POD mode 1 prediction, – – – PSE prediction, $*$ truncated PSE prediction ($0.5 \leq x/D \leq 8.9$), and ——— Cavalieri *et al.*'s (2012b) experimental data.

here are not suitable for this because there is no way of knowing if these erroneous predictions would respond to such changes in the same way that accurate predictions would.

As discussed in § 4.4.4.3, the effect of the axial truncation of the near-field array is also expected to contribute to this error. To estimate this effect, the PSE CSM was truncated to $0.5 \leq x/D \leq 8.9$, and the result is also presented in figure 4.22. The truncation does cause a significant deviation in the predicted directivity shape, though it is not great enough to account for the large deviation between the predictions and the experimental results. The truncation effect may be sufficient to explain the discrepancy between the full-data prediction and the experimental result, but this is impossible to verify since the modelling techniques used in appendix B.2 are not helpful at this Mach number.

One significant difference between the experimental data and the validation problem in appendix B.1 is that the wavepacket in the validation problem is fully coherent. This allows that the truncation effect could be different on coherent and incoherent wavepacket sources, which increases the ambiguity of the results. Further investigation into the relationship between the truncation effect and the coherence of the CSM will be necessary.

4.5 Conclusion

4.5.1 Summary

In recent years, wavepacket models for jets have shown considerable promise for the prediction of acoustically important flow fluctuations, particularly for fluctuations that are azimuthally and axially coherent, which have been associated with low-angle sound emissions. Recent analysis of the far-field sound emissions and the in-flow velocity field of a subsonic jet by Cavalieri *et al.* (2012b) found close agreement between wavepacket predictions based on PSE and experimental fluctuation measurements on the jet centreline up until the end of the potential core, indicating the presence of wavepackets at least up to this point. From their measurements, the mechanism responsible for this breakdown was unclear and three potential hypotheses were proposed, one of which was that the wavepackets do continue beyond the potential core, but are dominated by incoherent fluctuations. The current investigation analyzed the near-field pressure signatures of the same jet to test this hypothesis and to form a link between the near-field pressure fluctuations and the far-field sound emissions.

The results indicate that linear wavepackets persist in the jet beyond the end of the potential core. The presence of these wavepacket fluctuations is masked by incoherent fluctuations in this region, but wavepackets can be recovered by axial POD filtering. A time-domain reconstruction of the near-field fluctuations for each POD mode has been performed, allowing the near-field fluctuations to be projected onto an empirically obtained wavepacket (POD mode). This made it possible to consider the correlation between the POD modes and the far-field sound. The correlation indicated that the first POD mode captures the salient features of the space–time correlation to the far-field sound, but the higher POD modes also showed significant correlations to the far-field, indicating that a single POD mode is insufficient to extract all the acoustically important flow fluctuations.

The statistical far-field Green's function prediction of the near-field data from a conical microphone array was shown to be valid—a result already known from the work of Reba *et al.* (2010)—but the application to the experimental data gave poor directivity predictions. The Green's function prediction method was also extended to make time-domain predictions of the far-field sound, a quantity that that could be compared directly with the current experimental dataset. A comparison of the both the directivity and time-domain predictions for a validation problem, in which it was possible to consider arrays matching the experimental extent as well as those with much longer extents, gave clear evidence that the poor predictions result from the finite extent of the near-field array. This truncation creates a spurious source at the array edge that is perfectly correlated with the wavepacket source, resulting in constructive and destructive interference and leading to poor predictions. The effect of this spurious source was also shown to be less important for higher-Mach-number jets, which is consistent with Reba *et al.*'s (2010) successful predictions at high Mach number.

Clearly, for accurate far-field predictions from near-field wavepackets at low Mach number, it will be necessary to deal with the problem of truncation of the near-field microphone array. While this truncation is not an issue for PSE-based wavepacket prediction schemes, the current results show that in order to provide accurate predictions at low Mach number, PSE solutions may have to incorporate extra information. It is not yet clear whether this information is the incoherent fluctuation levels making up the difference between the measured signal and the PSE predictions (see figure 4.9) or simply information about the non-unit coherence off the main diagonal of the CSM. Determining which of these pieces of information—or combination thereof—is necessary for accurate predictions will have to remain the work of future studies.

4.5.2 Outlook

The analysis toolbox presented in the current chapter contains many of the tools necessary to make statistical and time-domain predictions of far-field sound emissions from real jets based on a wavepacket representation of the dominant sound source. These tools also make it possible to address the problem of the finite extent of the near-field array, which may be a fruitful avenue of research. A treatment of this truncation problem in experimental cases may also be beneficial for CFD simulations in which the source domain is calculated separately from the observer domain using an arbitrary delineation. In such cases, it is possible that a spurious source like the one seen here could also appear, requiring similar treatment.

Wavepackets remain a promising candidate for a sound source structure in jets. Their existence within the jet near-field is apparent from quantitative comparisons, and the current results indicate they indeed persist beyond the potential core. In order to finish the jigsaw puzzle that links wavepacket sources to far-field jet noise emissions, it will be necessary to address the outstanding questions of how to address the experimental limitation of a finite microphone array and what the effects of both non-unit coherence of the CSM and incoherent fluctuations downstream of the potential core are on jet noise emissions.

Chapter 5

Time-resolved similarity in aeroacoustic signals

5.1 Introduction

5.1.1 Similarity in aeroacoustic signals

The ultimate aim of jet noise prediction schemes is an estimate of the far-field sound that is identical to—or at least 'similar' to—the actual far-field sound produced by a jet. In general, a time-domain description of the far-field sound is unnecessary because regulatory noise limits use statistical measures in their definition. This is because the human ear is also sensitive to noise on a statistical basis (see § 2.2.1). Therefore, for the purposes of jet design, knowledge of the sound emissions on a statistical basis is sufficient to make design decisions. However, to understand and describe jet source mechanics and to test the performance of jet noise models based on time-domain source models, time-domain comparisons between predictions and simulated data are useful. The usefulness arises from the different perspective that is available in the time domain, allowing a fuller picture of the jet physics and prediction performance to be drawn. This can lead to a better understanding of which source mechanics are being captured by a particular source model and which are not, allowing improvements to prediction techniques to be developed more effectively.

Recent techniques that allow comparison between time-resolved predicted and recorded sound fields include time-resolved comparisons of acoustic analogies with DNS calculations (Samanta *et al.*, 2006), semi-empirical sound calculations from TR-PIV data (Haigermoser, 2009; Koschatzky *et al.*, 2011), Kirchhoff surface projection methods (Lyrintzis, 1994), and time-domain projections to simplified source models with analytical solutions (Cavalieri *et al.*, 2011; Kerhervé *et al.*, 2012). Ultimately, the comparisons are made between either spectral or time-domain signal shapes, finding the maximum deviation or determining qualitatively if they are 'similar'. While these types of comparisons yield insight into the accuracy of such predictions, the picture they draw is still incomplete. Comparing two spectra can indicate if a prediction is sufficiently accurate, but if the predictions are not similar, the comparison cannot give hints as to what is missing from the prediction scheme. While purely qualitative time-domain comparisons can help in this regard, they cannot provide an objective evaluation of what prediction scheme is best or be used as input in an optimization algorithm. A quantitative, time-domain *similarity metric* would fulfill both criteria. An ideal metric would be sensitive to errors indicating poor model agreement while remaining relatively invariant to random noise and small errors arising from (non-dominant) unmodelled phenomena.

The usefulness of a time-domain perspective on understanding model errors was demonstrated in § 4.4.4.3, in which a spurious source arising from the abrupt truncation of the near-field microphone array was identified. This explanation was not apparent from a simple comparison of the statistical sound properties of the sound generation (SPL spectra). Combining such a time-domain perspective with an objective metric suitable for comparison and optimization problems may prove to be a useful tool in the development of noise source prediction techniques.

5.1.2 Toward an improved similarity metric

The definition of a suitable similarity metric is not straightforward. It depends on a precise definition of what is meant by 'similar.' A suitable definition for the current work can now be chosen: two time-domain signals are *similar* if the difference between them is small errors arising from common, unimportant uncertainties in aeroacoustics predictions. The precise definition, therefore, depends on the types of errors expected and which are considered significant. For the current work, these are selected and described in § 5.1.3. In general, for each of these errors, an ideal metric should have the following characteristics:

Monotonicity It should monotonically depart from the optimal value as the error magnitude increases.

Uniqueness It should reach its optimal value only when the error magnitude is zero.

Orthogonality If the full signal error is due to a combination of these errors, increasing any of them should move the metric's value farther from the optimal value, not closer.

The importance of monotonicity is that it allows a parametric optimization to be performed on a particular prediction technique, allowing the best prediction—or the first within a certain tolerance—to be determined. If the departure from the optimal metric value is not monotonic, the objective function may contain multiple local minima or maxima on axes other than the error magnitude. Uniqueness is necessarry to ensure a unique solution to the optimization problem. The simplest example of a metric that has more than one solution (non-unique) is one based only on the energy in the signal (*e.g.* see § 5.2.3.1). Since the energy of a signal is not a unique descriptor, any number of signals could have the same energy as the reference signal, and the metric would hold no power to discriminate between them. Finally, orthogonality is desirable because it allows the isolation of errors affecting the noise predictions. However, determining the orthogonality of the metrics under the errors tested here is beyond the scope of this work.

Again, an ideal metric is one that is sensitive to the errors that are considered important and insensitive to those considered unimportant. This work considers four metrics from this perspective. A Structural Similarity metric (SSIM) originating from image compression analysis has been successfully applied recently to time–frequency representations of biological neurogram signals (Hines & Harte, 2012) and speech signals (Hines *et al.*, 2012), prompting the current study into its use for aeroacoustics. For images, the optimal compression stores an acceptable representation of the image as compactly as possible, ignoring extraneous detail and retaining only the information most important for human interpretation (*i.e.* structural information). The aeroacoustic analogue is that sound predictions cannot be expected to predict all the rich detail of the sound emissions (see § 2.1), but they must capture the mechanics of the dominant sound emissions to be useful.

Rather than to fully generalize the SSIM for a variety of aeroacoustics applications, the aim of the present study is to adapt the SSIM for use with time-domain pressure signals and test its performance against a number of common aeroacoustics-type errors. Further development of the technique and application to more realistic problems will be left to future investigations. The SSIM could be applied to a number of problems in aeroacoustics. One example would be the determination of the optimal microphone array spacing and axial extent for experiments of the type presented in chapter 4. This would be a good evaluation to show its usefulness in aeroacoustics, but such an evaluation is beyond the scope of the current work. Some potential applications of the SSIM to additional practical aeroacoustics problems are listed in § 5.4.

5.1.3 Errors expected in aeroacoustics predictions

The previous section noted that the evaluation of a similarity metric requires a choice of which errors are important in aeroacoustic predictions and which are not. The results of the far-field predictions in the validation problem of § 4.4.4.3 (particularly figure 4.20) give an example of the some of the types of errors that can arise in prediction schemes in aeroacoustics problems. Figure 4.20 shows that the occurrences of the peaks and troughs in the prediction correspond well to the reference solution even though there is an ≈ 6 dB discrepancy in magnitude for the statistical comparisons. This is an example of *amplitude error*: although the features of the signal are well represented, the absolute level of the fluctuations are not captured. Arguably, this is the most important type of error since the magnitude of a signal across a wide range of frequencies is precisely what jet noise prediction for regulatory purposes requires. However, this information is already available directly from statistical measures, and no real benefit is gained from incorporating this error again in a time-domain metric. To reiterate, the perceived advantage of a time-domain metric is to better understand what part of flow physics is either captured or not captured as opposed to determining absolute levels for a final design decision. In fact, due to scaling in the SSIM procedure used here, it will be seen that the SSIM is completely insensitive to such amplitude errors. But due to the fact that this type of error is not particularly informative in the type of applications imagined for the SSIM in aeroacoustics, this is not considered a drawback but rather an advantage of the technique. Ultimately, a successful similarity metric will not simply replace simple statistical measures but complement them, leading to a more effective comparison technique.

A second group of errors, which will be the focus of the current investigation, arises from uncertainties in the source and propagation mechanics of jet noise emissions:

Random-noise error This error is apparent particularly in figure 4.20(c), where the prediction captures the behaviour of the reference signal very well except there are some small random fluctuations about the reference signal. These fluctuations are not particularly important in noise prediction if they only make up a very small portion of the signal energy. This is especially true if the fluctuations occur at frequencies far from the spectral peaks of the signal. An ideal metric would be relatively insensitive to this type of error as long as the noise is at reasonable levels.

Time-lag error Uncertainty in the exact propagation time from a source to an observer is a common issue in jet noise predictions. Uncertainty in the exact source location is the first contributor to this issue, but there are others. In a quiescent fluid, since the propagation path is direct, the propagation time can be determined directly from $\tau = |\mathbf{x}_o - \mathbf{x}_s|/c_0$. However, in the presence of a non-zero mean flow, the effect of ray refraction frequently causes the propagation path—even on average—to be unknown. Unsteady fluctuations in the jet also have an effect on the exact propagation time. The result of these factors is an ambiguity that is particularly important in beamforming and correlation-based source localization techniques, which assume a particular propagation time. The monotonic departure from the optimal metric value is especially important in this case, because the shape of the autocorrelation, which will be seen in § 5.3.2 to affect certain types of metrics, can create local maxima and minima far from the optimum time lag. If the departure is monotonic, than this allows a more robust determination of the optimum lag by incorporating a metric into a cross-correlation-like routine.

Frequency-shift error This is most likely to arise from the Doppler effect when the source of the noise is convecting in the flow. If the observation location is stationary and the source is moving toward it, the observed frequency will be higher than the source frequency. An ideal metric would be able to distinguish if a frequency shift is present in the same way that the an optimal time lag is found in a correlation. The signal could then be systematically Doppler shifted and the shift at which the most optimal metric value is determined would estimate the frequency shift. Again, this requires a monotonic departure from the optimal metric value.

Jittery-phase (Random-cancellation) error Unsteady fluctuations in the jet can cause variations in propagation paths allowing for multiple paths of arrival for the emissions from a single in-jet sound source. When the propagation paths are different lengths, the signal phases at arrival will be different, leading to self-interference of the sound source's emissions. If the fluctuations are random and normally distributed around the mean path length, the effect will most likely be decreased strength at the observer as well as a broadening of the signal. It is difficult to prescribe how an ideal metric should respond to such an error beyond a monotonic departure from the optimal value.

Non-linear errors Non-linear interactions can lead to far-field fluctuations that are related to a near-field source but will not correlate well. Traditional tools for detecting these types of interactions include the bispectrum and the bicoherence. Again, prescribing a behaviour for an ideal metric beyond the monotonic departure from the optimal value is difficult. In this work, the non-linear effects will be simulated by quadratic and cubic interactions.

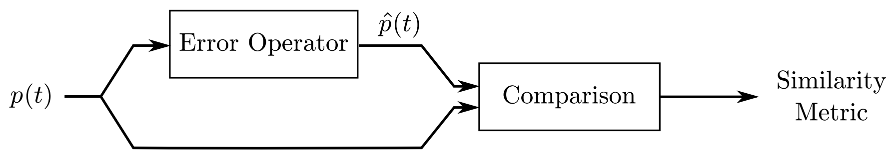

Figure 5.1: Process model for current study

5.2 Analysis procedure

5.2.1 Outline

Figure 5.1 shows the process model used in this study. A reference signal, $p(t)$, undergoes one of four different error operators (see § 5.2.2 and table 5.1 below) resulting in a corrupted signal, $\hat{p}(t)$, and the two signals are compared to give a single similarity metric. The candidate metrics are compared as a function of the magnitude of the applied error; this magnitude is set by prescribing the pertinent variable in table 5.1. Figure 5.2 shows examples of the corrupted signals in comparison to the reference signals for each error type with the error magnitude set to 0.75. Table 5.1 also gives the expressions used for each type of error while § 5.2.2 describes the expressions in more detail. The metrics used here are summarized in table 5.2 and detailed in § 5.2.3.

5.2.2 Error operators

Random noise Normally distributed random signal noise was added to the time series scaled by ϵ so that when $\epsilon = 1$, the energy of the signal noise is the same magnitude as the signal energy. This represents measurement errors and uncorrelated, unmodelled sound generation.

Time lag The time lag was applied by a frequency domain $e^{-i\omega t_{\mathrm{lag}}}$ phase shift such that when $t_{\mathrm{lag}} f_c = 1$, the signal has been shifted by one period of the centre frequency. This represents uncertainty in the sound propagation path from aeroacoustic sources in turbulence.

Frequency shift A linearly interpolated resampling of the signal provided the frequency shift where the shifted centre frequency is $f_c + \Delta f_c$, representing errors due to Doppler shift, associated with convecting sources.

Jittery phase This error simulates the effect of multiple paths from a turbulent sound source to an observer, a phenomenon attributable to turbulent fluctuations that cause differences in refraction during sound propagation, leading to random self-interference of the source. κ controls the standard deviation (σ_p) of the propagation time. When $\kappa f_c = 1$, σ_p is one period of the signal's centre frequency.

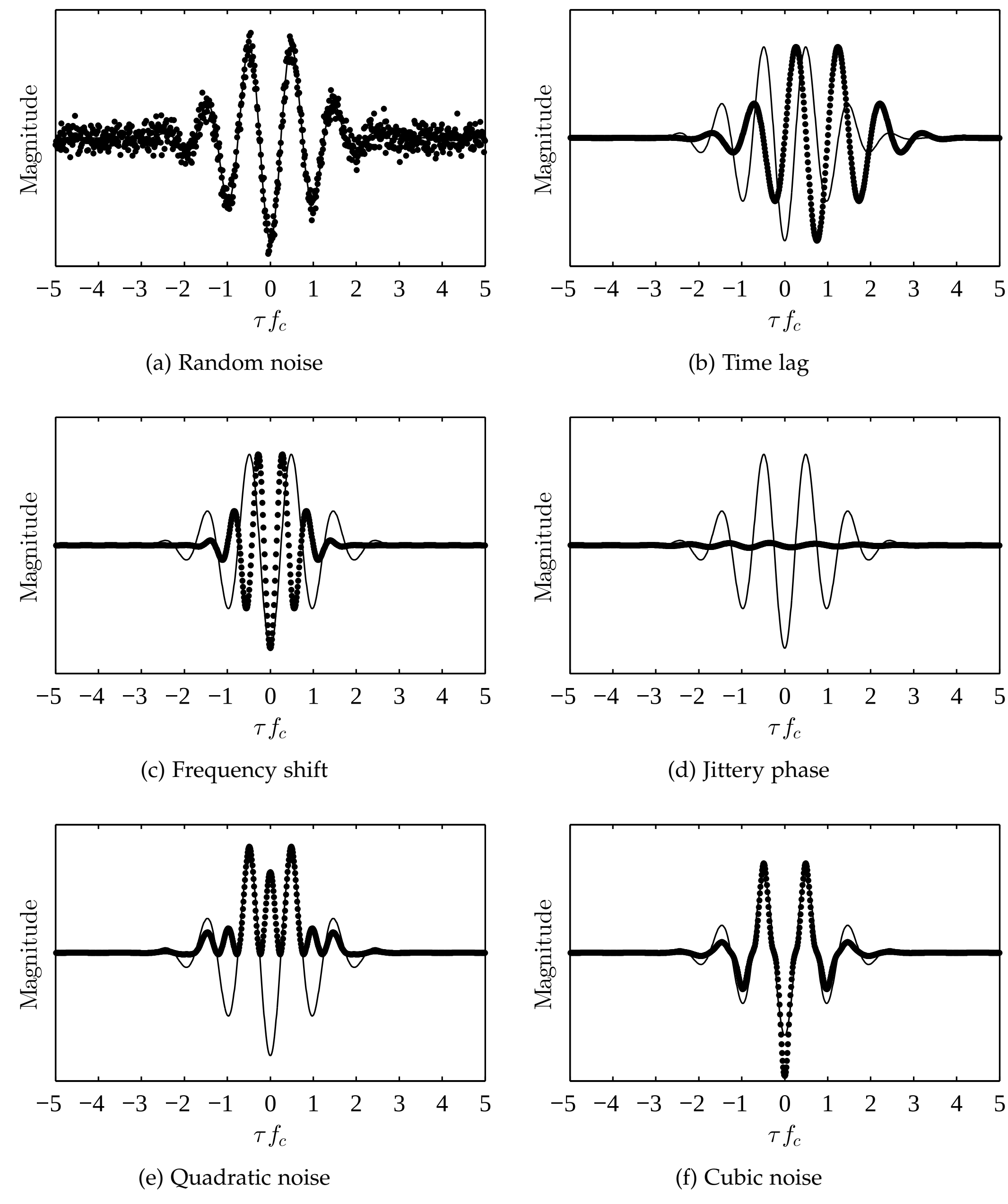

(a) Random noise

(b) Time lag

(c) Frequency shift

(d) Jittery phase

(e) Quadratic noise

(f) Cubic noise

Figure 5.2: Sample comparison between ——— $p(t)$ and $\cdots\cdots$ $\hat{p}(t)$ for the different error types with the pertinent error variable set to 0.75

Quadratic and cubic noise These types of noise imitate non-linear interactions between acoustic sources. The noise is controlled as a ratio of linear and higher-order terms. When $\nu_i = 1$, with $i = 2$ or 3, the signal is fully quadratic or cubic, while $\nu_i = 0$ gives linear signals.

5.2.3 Metric types

Four metrics are investigated in this work: two classical metrics—the Relative-Energy metric (RE) and the Mean-Square-Error metric (MSE)—and two variations of the SSIM introduced by Wang *et al.* (2004). These metrics are summarized in table 5.2.

5.2.3.1 Relative Energy (RE)

The RE simply compares the ratio of the total energy of two time signals. In functional form

$$\mathrm{RE} = \frac{\int \hat{p}(t)^2 dt}{\int p(t)^2 dt}. \tag{5.1}$$

For identical signals, RE $= 1$, which is the optimal value for similarity. The RE is invariant under shifts in time and frequency provided the signal has a constant envelope. Different signals can have the same energy, leaving the RE with little discriminative power. The spectral and directivity comparisons used frequently in aeroacoustics are a form of energy metric, where the comparison is made with subsets of the collected data.

5.2.3.2 Mean Square Error (MSE)

The MSE is a normalized measure of the mean deviation between two signals. It is expressed simply as

$$\mathrm{MSE} = \frac{\int (\hat{p}(t) - p(t))^2 dt}{\int p(t)^2 dt}. \tag{5.2}$$

Unlike the RE, the MSE is highly discriminatory between different signals, and MSE $= 0$ (the optimal value) only occurs when the signals are identical.

5.2.3.3 Structural Similarity (SSIM)

The SSIM was developed for the comparison of the quality of images subject to various compression algorithms (Wang *et al.*, 2004), and measures how similar images are with respect to their structure within a particular convolution window. In each convolution window and for each image (x, y), local means (μ_x, μ_y), standard deviations (σ_x, σ_y), and an autocovariance (σ_{xy}) are calculated and compared. The SSIM is a local measure,

Table 5.1: Error expressions for metric comparison

Name	Expression	Variable
Random noise[a]	$p(t) + \sqrt{\epsilon \langle p^2 \rangle} X(t)$	ϵ
Time lag	$p(t - t_{\text{lag}})$	$t_{\text{lag}} f_c$
Frequency shift	$p(t/(1 + \Delta f_c / f_c))$	$\Delta f_c / f_c$
Jittery phase[a]	$\frac{1}{N} \sum_i^N p(t + \kappa X(i)), N = 500$	κf_c
Quadratic noise	$\nu_2 p(t)^2 \sqrt{\langle p^2 \rangle / \langle p^4 \rangle} + (1 - \nu_2) p(t)$	ν_2
Cubic noise	$\nu_3 p(t)^3 \sqrt{\langle p^2 \rangle / \langle p^6 \rangle} + (1 - \nu_3) p(t)$	ν_3

[a] $X(\cdot)$ is a normally distributed random variable with unit standard deviation

Table 5.2: Metrics used in similarity analysis

Name	Symbol	Expression	Optimal Value
Energy	RE	$\frac{\int \hat{p}(t)^2 dt}{\int p(t)^2 dt}$	1
Mean square error	MSE	$\frac{\int (\hat{p}(t) - p(t))^2 dt}{\int p(t)^2 dt}$	0
1D SSIM	WSSIM_{1D}	Equation (5.7) using $p(t)$	1
Time–frequency SSIM	WSSIM	Equation (5.7) using $\check{p}(t, f_{\text{pseudo}})$	1

which operates on a 2D scalar field, returning a 2D scalar field that can be averaged to find the mean SSIM (MSSIM) for a particular image pair. These values are calculated by

$$\mathrm{SSIM}(x, y) = l(x, y)c(x, y)s(x, y), \tag{5.3}$$

$$\mathrm{MSSIM} = \frac{1}{N}\sum_{j=1}^{N} \mathrm{SSIM}(x_j, y_j), \tag{5.4}$$

where

$$l(x, y) = \frac{2\mu_x\mu_y + C_1}{\mu_x^2 + \mu_y^2 + C_1}, \qquad c(x, y) = \frac{2\sigma_x\sigma_y + C_2}{\sigma_x^2 + \sigma_y^2 + C_2}, \qquad s(x, y) = \frac{\sigma_{xy} + C_3}{\sigma_x\sigma_y + C_3}, \tag{5.5}$$

$$C_1 = (K_1L)^2, \qquad C_2 = (K_2L)^2, \qquad C_3 = C_2/2. \tag{5.6}$$

C_1, C_2, and C_3 avoid singularities when the denominators would otherwise be small, where K_1 and K_2 are arbitrarily taken as 0.01 and 0.03, respectively, and L is the dynamic range of the image (Wang *et al.*, 2004). Regardless of the choice of constants, MSSIM $= 1$ occurs only if the images are identical. Following Wang *et al.* (2004), a Gaussian-weighted convolution window was chosen.

Equation (5.4) implies that every part of the 2D field is equally important for analyzing the structure, which is a poor assumption for acoustic signals. In light of this, a weighted SSIM was used:

$$\text{Weighted SSIM} = \sum_{j=1}^{N} w(x_j)\mathrm{SSIM}(x_j, y_j), \tag{5.7}$$

where $w(x_j)$ is a weighting function defined by the local magnitude of the reference signal.

Some details of the SSIM analysis that are not important for considering its performance but would be necessary to reproduce the current results are presented in appendix C.

1D SSIM (WSSIM$_{\mathbf{1D}}$) Though the SSIM was developed for 2D signals (images), it can be applied to 1D time series by considering the signal as a $N_t \times 1$ pixel image and using a 1D convolution window. The formula is still given by equation (5.7). Computationally, this is preferable to the time–frequency case because it eliminates several steps from the calculation.

Time–frequency SSIM (WSSIM) Hines *et al.* (2012) applied the SSIM to short-time Fourier transforms of acoustic signals, where the image 'intensity' was the modulus of the Fourier coefficients. In this work, a continuous wavelet transform (CWT) was used to take advantage of the higher temporal resolution for higher frequency signal components. The wavelet used here was a complex-valued Morlet wavelet with $\omega_0 = 6$ as it shares the characteristic shape of a modulated wavepacket, leading to efficient collapse of the investigated signals onto a few wavelet coefficients. The wavelet scales can be converted to pseudo-frequencies (Torrence & Compo, 1998), and the resulting time–frequency 'image' is then $\check{p}(t, f_{\text{pseudo}}) = |\text{CWT}[p(t)]|$ for use in equation (5.7).

5.3 Results

5.3.1 Test signals

Two test signals were investigated: a simulated Gaussian-modulated sinusoid and an experimental far-field recording from the free jet flow in chapter 4. Both signals were sampled at $f_s = 100$ kHz. The chosen centre frequency for the simulated signal was $f_c = 1/T_0 = 1225$ Hz, which corresponds to a Strouhal number $St = fD/U = 0.3$ for the experimental recording. In each case, the signals spanned $-300T_0 < t < 300T_0$, but only the centre third of the points were used in the comparison to avoid edge effects after applying the frequency and time shift errors. The simulated signal corresponds in shape to the solution of wavepacket-type models for jet noise (Cavalieri *et al.*, 2011):

$$p(t) = -\exp(-t^2/T^2)\exp(\mathrm{i}2\pi f_c t), \tag{5.8}$$

where the characteristic width was set by $T = \sqrt{2}T_0$.

The experimental pressure signal was the axisymmetric mode of the far-field microphone ring from the jet flow considered in chapter 4. For the WSSIM, the wavelet scales were chosen to correspond to 200 evenly spaced pseudo-frequencies ranging from the experimental anechoic cut-off, 200 Hz, to 50 000 Hz ($\Delta f \approx 250$ Hz).

5.3.2 Metric performance

Figures 5.3 and 5.4 present the results of the metric computations for the simulated and experimental cases, respectively. The criteria for evaluating the performance of each metric were discussed in § 5.1.2, the most important of which are a monotonic departure from the optimal value as the error magnitude is increased and a resistance to random-noise error.

The RE performs as expected with a monotonic sensitivity to signal noise and no

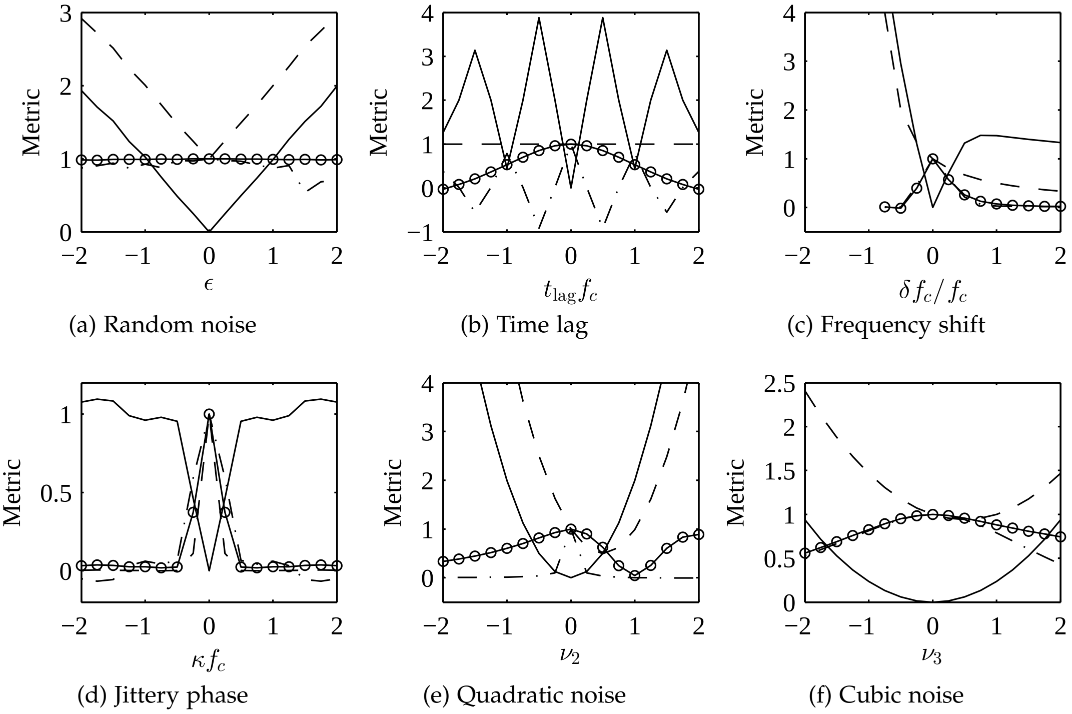

(a) Random noise (b) Time lag (c) Frequency shift

(d) Jittery phase (e) Quadratic noise (f) Cubic noise

Figure 5.3: Results from metric tests with simulated data. – – – Relative energy (RE), ——— Mean square error (MSE), · – · – · 1D SSIM (WSSIM_{1D}), —⚬— Time–frequency SSIM (WSSIM).

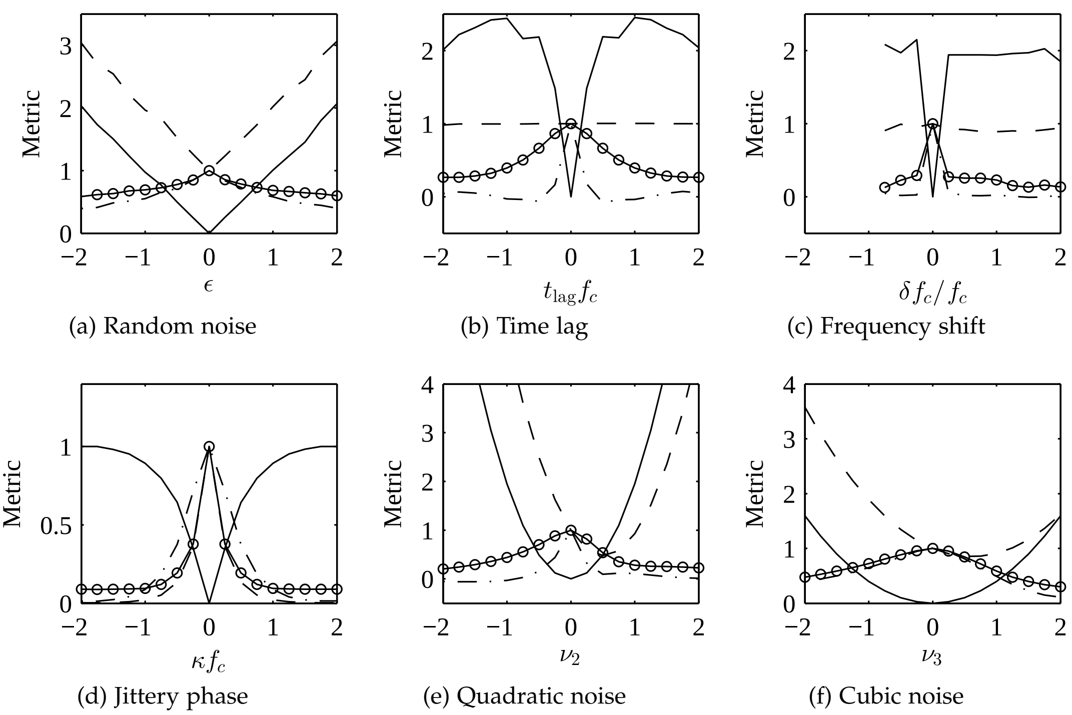

(a) Random noise (b) Time lag (c) Frequency shift

(d) Jittery phase (e) Quadratic noise (f) Cubic noise

Figure 5.4: Results from metric tests with experimental far-field data. – – – Relative energy (RE), ——— Mean square error (MSE), · – · – · 1D SSIM (WSSIM_{1D}), —⚬— Time–frequency SSIM (WSSIM).

discrimination under time and frequency shifts.[1] The biggest issue with the RE is this lack of discrimination between signals, which may have the same energy. This shortcoming makes the RE unsuitable for similarity analysis.

The MSE shares this monotonic sensitivity to signal noise, but the bigger issue is the dependence of the response to a time lag on the autocorrelation of the input signal. If the signal has minima and maxima in the autocorrelation, they also appear in the metric. For periodic and semi-periodic signals, the presence of local minima and maxima could be misleading for prediction verification (see § 5.1.2). Under a frequency shift, the MSE also discriminates well with a distinct minimum at zero.

The WSSIM_{1D} performs better with random signal noise. The high resistance is due to the convolution operator, which tends to average out random signal noise, causing it to only weakly affect the WSSIM_{1D}. However the difficulty apparent in the MSE results, in which additional minima and maxima appear in the curves is shared by the WSSIM_{1D}. This effect arises from the σ_{xy} term in $s(x, y)$ of equation (5.5), which can take negative values if the corrupted signal is correlated to the original signal in the convolution window. The performance under a frequency shift is nearly ideal: a sharp peak at zero with slow, even decay as the error increases. This is precisely the type of feature that could be easily detected by an optimization algorithm.

Strikingly, the WSSIM overcomes both the issue of random noise sensitivity and multiple minima and maxima, indicating the best performance. The extra resistance to random signal noise over the WSSIM_{1D} is due to the wavelet decomposition, which effectively distributes the noise across all the wavelet coefficients, minimizing the impact on the metric. In fact, across all pertinent error types, the WSSIM gives a peak at zero error with monotonic decay as the absolute error increases. Although in the quadratic noise case a second peak is present near $\nu_2 = 2$, this is not present in the experimental data. Again, this clear peak around zero error is the desired response that was proposed for an ideal metric in § 5.1.2.

The interpretation of the jittery-phase and non-linear noise results is less straightforward than the simpler error types, but the same general principle applies: the desired feature is an identifiable peak or valley at zero error. From this perspective, both the WSSIM_{1D} and WSSIM perform nearly the same. For the jittery-phase error, all four metrics perform equally well. The MSE performs well for both quadratic and cubic noise while the RE is misleading because there is no identifiable feature at $\nu_i = 0$.

Considering the performance across all error types, the WSSIM is the best-

[1]With the simulated signal, the RE does depend on the frequency shift. This is because the signal has a finite-width temporal envelope which narrows as the frequency is shifted upward, reducing the total energy. The RE follows a $1/\Delta f_c$ relationship in this case and yields no useful information. Since the experimental signal has no such envelope, the RE is constant under a frequency shift.

performing metric. Particularly with the experimental signal, it gives a clearly identifiable peak feature in each case. The WSSIM performs like the ideal metric proposed in § 5.1.2, showing considerable promise as a similarity metric for aeroacoustic applications.

5.4 Conclusion

5.4.1 Summary

This work compared the performance of four similarity metrics for time-domain pressure signals. The relative-energy metric exhibits poor discrimination between signals and high sensitivity to random noise. The mean-square-error metric is also highly sensitive to random noise and phase error. The WSSIM using a time–frequency signal representation is resistant to random signal noise and provides clear discrimination between time lags and frequency shifts as well as other types of error. While a one-dimensional version of the WSSIM also performed well for most error types, the dependence of the response to a time-lag error on the signal's autocorrelation makes it unsuitable for use aeroacoustics applications. The performance of the WSSIM in a test of an artificially corrupted experimental jet-noise signal was outstanding, giving an easily identifiable peak feature around the zero-error mark and with no other distracting peaks. This characteristic is necessary for a successful similarity metric because it allows its use in parametric optimization algorithms and parameter identification problems.

5.4.2 Outlook

The WSSIM shows great promise as a useful similarity metric for quantitative time-domain signal comparisons in aeroacoustic applications. Some examples of aeroacoustics applications that could benefit from the use of the WSSIM include

- determining the necessary axial extent of a near-field array for Green's function projections of the type performed in chapter 4,
- determining the optimal number of detectors and their locations for Linear Stochastic Estimation (Adrian, 1979) of noise sources in jets,
- comparing the performance of different acoustic analogies in the prediction of far-field sound from TR-PIV data (Haigermoser, 2009; Koschatzky *et al.*, 2011),
- and comparing the efficacy of far-field sound calculations based on various simplified source models with analytical solutions (Cavalieri *et al.*, 2011; Kerhervé *et al.*, 2012).

It still remains to determine how the WSSIM will perform in more practical applications such as those listed above, but this will remain the work of future investigations.

Chapter 6

Conclusion

6.1 Summary

For over six decades, the aeroacoustics community has been determinedly studying the problem of aircraft noise emissions, seeking to reduce the perceived noise emissions from aircraft, making room for the aviation industry to continue to grow, and thereby allowing it to meet to the changing needs of global culture and commerce. The most significant contributor to these noise emissions at takeoff is jet noise. Though many significant advances have been made, an adequate theory of jet noise comprising a sufficient understanding of jet noise production to make accurate predictions that can be fully incorporated into the aircraft design cycle does not yet exist, and more fundamental research into the sources of jet noise is necessary.

Building on the foundation laid by the aeroacoustics community during the past decades, this thesis contributes to furthering the understanding of jet noise by developing and testing tools for time-resolved source analysis. This avenue of research has been made possible by the introduction of new measurement and analysis techniques that were not available at the advent of aeroacoustics research. Though statistical predictions of jet noise emissions are sufficient for regulatory qualification of aircraft, the advantage of time-domain analysis is the additional insight available for the development of jet noise prediction schemes from information that would be unavailable or masked in a statistical description of the jet noise sources. Adding context to the novel techniques, each development is compared and contrasted to results available from traditional statistical techniques.

This thesis has presented three studies investigating independent aspects of time-resolved jet noise source analysis. Chapter 3 applied Time-Resolved Particle Image Velocimetry (TR-PIV) to the localization of noise sources in a subsonic jet using the direct correlation technique, noting the advantages and shortcomings of TR-PIV for this type of analysis, as well as noting the ambiguity of such techniques in the presence of non-compact sources. Chapter 4 compared statistical predictions of near-field wavepacket signatures to near-field pressure measurements on a conical microphone array and developed a technique for predicting the far-field sound emissions in the time domain using the near-field data, comparing the results to experimental far-field measurements. Chapter 5 introduced a structural similarity metric originating from image compression analysis as a quantitative metric for comparing time-domain aeroacoustic pressure signals. Among other benefits, such a metric is suitable for use in optimization-based development of noise source models.

Unified by the common paradigm of time-resolved analysis, each element of this study contributes to the understanding of jet noise sources by approaching the analysis from a different perspective. The principal findings are as follows:

Time-resolved Particle Image Velocimetry jet noise source analysis

- TR-PIV can produce direct correlation plots with the same flow features as traditional techniques such as standard PIV and hot-wire anemometry.
- The error in practical TR-PIV measurements, particularly at high frequencies and low fluctuation energies, yields corrupted frequency-domain estimates of statistical quantities and acts to reduce coherence estimates. This frequency-domain error minimizes an important advantage of TR-PIV over standard PIV: the availability of a coherence estimate.
- For the flow configurations tested, the TR-PIV error does not significantly affect estimates of the time-domain correlation coefficient.
- The direct in-flow–far-field correlation signature detected in the low-Mach-number jet investigated can be reproduced by a simple simulation of an axially extended wavepacket source.
- In the presence of such an axially extended wavepacket source, the localization of the peak sound generation region using direct correlation is ambiguous.
- The TR-PIV analysis results are consistent with—but do not require—the dominance of an acoustically important, axially extended wavepacket noise source for the low-speed jet studied.

Prediction of near-field wavepackets and time-resolved far-field sound

- The presence of linear wavepackets in the axisymmetric mode of the pressure field beyond the potential core of a subsonic jet has been verified. This is despite the fact that beyond the potential core their signatures were not apparent in velocity measurements of the same jet.

- Beyond the jet's potential core, wavepackets in the pressure field are masked by incoherent fluctuations, but filtering the signal using axial Proper Orthogonal Decomposition (POD) is sufficient to uncover their signatures.

- Throughout the entire jet, predictions of the wavepacket amplitudes and phases provided by the parabolized stability equations closely match the experimental measurements for Strouhal numbers ranging from 0.3 to 0.7.

- Using time-domain measurements, the near-field pressure signal can be projected onto an independently recorded, empirically obtained statistical POD basis in the time-domain, providing a reduced-order reconstruction of the near-field jet dynamics. For low POD mode numbers, this time-domain reconstruction is possible using a sensor array with a shorter axial extent and coarser spacing than is necessary to initially obtain the POD modes.

- The cross-correlation signatures between each near-field POD mode projection and the far-field sound showed that the first POD mode had similar correlation features to the full near-field–far-field correlation, but other modes also had different correlation features that were also significant, indicating that a single POD mode does not capture all the salient sound-generating behaviour.

- The Green's-function-based far-field sound prediction scheme based on near-field wavepacket sources, successfully used by Reba *et al.* (2010) for higher-Mach-number jets, did not perform as well for the present jet because of the artificial introduction of a spurious source caused by the finite extent of the near-field microphone array. This source does not appear to be as important for higher-Mach-number jets, explaining why Reba *et al.*'s (2010) predictions were more successful than those performed here.

- The Green's function prediction technique has been extended to provide time-resolved predictions using time-domain near-field recordings, opening the door to time-resolved far-field predictions. This technique has been demonstrated using an artificially generated sample dataset, but meaningful comparisons with experimental data were not possible due to the same spurious source effect observed in the statistical predictions.

Similarity in time-resolved aeroacoustic signals

- A structural similarity metric originating from image compression analysis has been applied to aeroacoustic pressure signals, providing a quantitative metric for comparing two signals that are expected to be similar or identical.

- The structural similarity metric performs better than traditional metric types such as relative energy and mean-square-error metrics in the sense that it provides more discrimination between important aeroacoustic error types while remaining resilient to contamination by random signal noise.
- The structural similarity metric's performance makes it a strong candidate for use in the development of aeroacoustic noise source prediction schemes based on optimization procedures or parameter identification.

6.2 Outlook

The current theory of jet noise available to the aeroacoustics community is still far from complete, requiring better understanding of noise source mechanisms and greater predictive power. This thesis has contributed to a specific area of the problem by increasing the understanding of jet noise sources, developing tools and techniques for time-resolved jet noise source analysis with the aim to aid the development of more comprehensive jet noise prediction schemes. Many questions remain outstanding, and the results presented in this thesis have also raised new questions warranting further investigation by future researchers. Among the most pressing of the outstanding and new questions addressed by this thesis are the following:

- Can the abundance of spatial and temporal information provided by TR-PIV measurements be used to extract the acoustically important components of the in-flow velocity fluctuations in a jet?
- Can the fuller space–time history provided by TR-PIV—compared to traditional PIV and single-point measurements—be used to make firmer connections between statistical turbulence properties and the individual flow events leading to them?
- Can the spurious source effect observed in the time-domain far-field noise predictions from wavepacket sources be treated with appropriate post-processing techniques to obtain accurate predictions?
- Can the success of the time-domain far-field predictions observed in the validation problem be replicated with experimental data for higher-Mach-number jets?
- How does the structural similarity metric perform in more realistic aeroacoustic noise source model optimization problems?

Further details of these issues and more specific questions raised by this work are described in the conclusions of their respective chapters.

Over the past century, aircraft have gone from a hobbyist's dream to a staple of international transport and logistics. It is clear from the importance of the aviation industry in today's society and the growing need for air transport that the role of aircraft will only become more important in the years to come. The complexity of the jet noise problem coupled with the ardent fervour of those in the aeroacoustics community seeking to effect practical aircraft noise reductions ensures that jet noise will be an active and fruitful field of research many years into the future.

Appendix A

Details of jet flow studied in the TR-PIV analysis

A.1 Baseline free jet flow

Figure A.1 gives the mean and root-mean-square velocity development along the centre-line of the free jet flow. There is close agreement between the historical LDA measurements for this jet (Kerhervé *et al.*, 2010), the current TR-PIV measurements, and the current HWA measurements, which are only available from 2 – 4D. For the TR-PIV measurements, there is a clear bias error in AOI1 (0 – 1.5D). This error is not surprising when figure 3.7(a) shows that AOI1 is essentially random noise. Additionally, the edges of each AOI suffer from errors, which are likely the result of random noise. This is because the light sheet and camera focus were optimized for the centre of each AOI, leaving less than ideal PIV conditions for the AOI edges. There is also a slight overestimation of the RMS fluctuations beyond the end of the potential core. The effect of these errors is a reduction in the magnitude of the correlation coefficient, but the general correlation features remain unaffected, allowing the interpretation of the results given in § 3.6.3 to stand. Figure A.2 shows that the axial turbulence intensity is significantly higher than the radial intensity. This helps justify the choice of u' in the correlation instead of u'_r in the correlation.

More detail about the baseline jet flow, and its comparison to similar jets in the literature is available from Kerhervé *et al.* (2010). As a brief summary, the jet has a peak turbulence intensity of 16% in the mixing region, the shear layer spreads at an angle of roughly 5°, and both the momentum and vorticity thicknesses increase roughly linearly with x at rates comparable to the relevant literature.

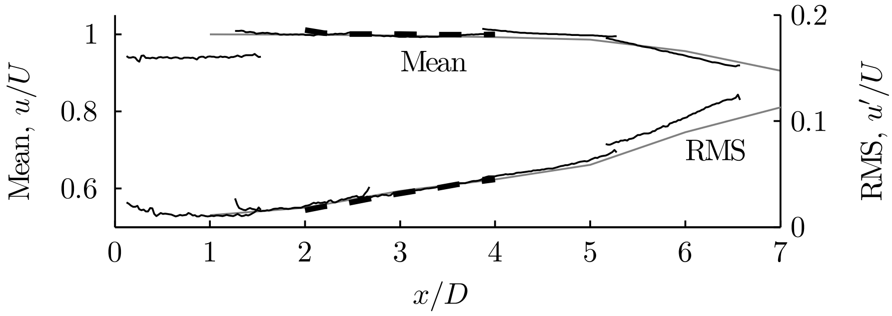

Figure A.1: Mean and root-mean-square u velocity development on free jet centre-line. ——— TR-PIV, – – – HWA, ——— Kerhervé *et al.* (2010) (LDA).

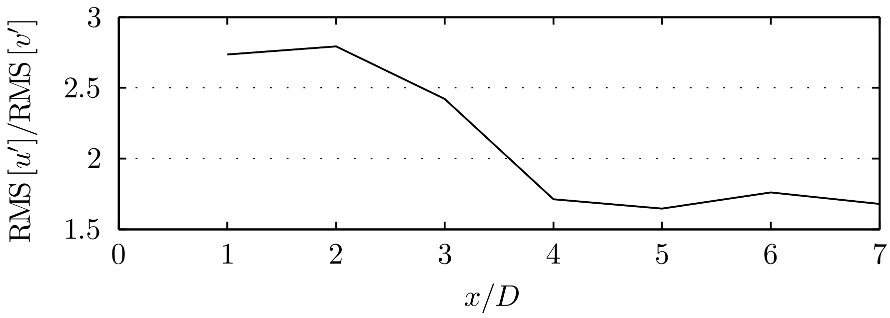

Figure A.2: Ratio of axial (u') to radial (v') turbulence intensity along free jet centre-line. Data from Kerhervé *et al.* (2010).

Appendix B

Validation and extension of the far-field Green's function predictions

B.1 Far-field prediction validation

The code developed for the calculation of the far-field pressure has been extensively validated by Léon (2012) and Léon & Brazier (2013), and a modified validation suitable for time-domain signals is presented here. The validation problem is generated for the azimuthal pressure mode by prescribing a simple line source for the Lighthill stress tensor given by[1]

$$T_{11}(x,t) = A(x)\tilde{p}_{\mathrm{exp}}(t - x/U_c),$$

where $A(x)$ represents an arbitrary spatial envelope, $U_c = 0.6U$ is an estimated wavepacket convection velocity, and $\tilde{p}_{\mathrm{exp}}(t)$ is an experimental pressure signal taken from the azimuthal mode of the microphone ring at $x/D = 4.1$. This was chosen so that the frequency content of the validation problem would be similar to the real case. $A(x)$ was taken to correspond roughly to the amplitude envelope of the first 4-ring POD mode using the model function

$$A(x) = A\exp\left[-\frac{(x-B)^2}{(C(x-b)+D)^2}\right], \tag{B.1}$$

where the coefficients A, B, C, and D were determined from a least-squares fit of the experimental data. For reference, the coefficients are tabulated in table B.1.

[1] $T_{11}(x,t) = \delta(y)\delta(z)T_{11}(x,y,z,t)$ where $\delta(\cdot)$ is the Dirac delta function.

Table B.1: Model constants used in validation problem

a	b	c	d
1.04	2.47 D	0.15	1.20 D

The Lighthill integral for this line source is solved using a high spatio-temporal resolution numerical calculation in the time domain by equation (3.1):

$$p'(\mathbf{x}_o, t) = \frac{1}{4\pi} \int \frac{1}{r} \frac{\partial^2 T_{ij}(\mathbf{x}_s, t - r/c_0)}{\partial x_i \partial x_j} d\mathbf{x}_s, \tag{B.2}$$

where the subscript o again indicates the observer location. The integral is solved for observers at positions along the near-field array from the array origin (X_0) to $x/D = 70$ with a spacing of $0.4D$ as well as at the position of each far-field microphone ($|\mathbf{x}_o|/D = 47.1$ and $15° \leq \theta \leq 80°$). To avoid edge effects from the finite time window, the Lighthill solution is calculated for a larger time window and only the central points are used in the predictions. The Green's function prediction for the far field is made by propagating the near-field Lighthill solution from equation (B.2) using the Green's function technique. This prediction is then compared directly to far-field Lighthill solution calculated directly from equation (B.2). The entire procedure is presented schematically in figure B.1, where the subscripts LH and GF represent the solutions by the Lighthill and Green's function methods, respectively.

In a direct numerical implementation of the time-domain formulation, the discontinuity also appears somewhere in the middle of the time series, and the periodicity of the Fourier transform causes some of the information from the end of the time series to be shifted to the front. This causes the portion of the data occurring before τ_{min} to be aligned improperly. The proper alignment can easily be recovered—along with the shifting of the discontinuity to the beginning of the time series—by applying a frequency-domain phase shift before performing the IFFT. This operation is represented in the schematic in figure B.1 by the operator $e^{i\omega\tau_{\text{min}}}$. Alternatively, the erroneous points could be placed at the end of the signal by replacing τ_{min} with τ_{max} in the operation.

Figure B.2 shows the results for both the statistical prediction and the time-domain prediction. Both sets of results used blocks of $N = 2440$ points corresponding to $\Delta\text{St} = 0.01$, where the time-domain result was calculated from a single block, and the statistical results were calculated by a series of blocks with 50% overlap. Since the statistical results compare only single frequencies, a Hann window was used in the calculation of $\mathbf{R}_{m,\omega}$ to avoid spectral leakage. No windowing was used for the time-domain result. The Green's function predictions faithfully reproduce the Lighthill

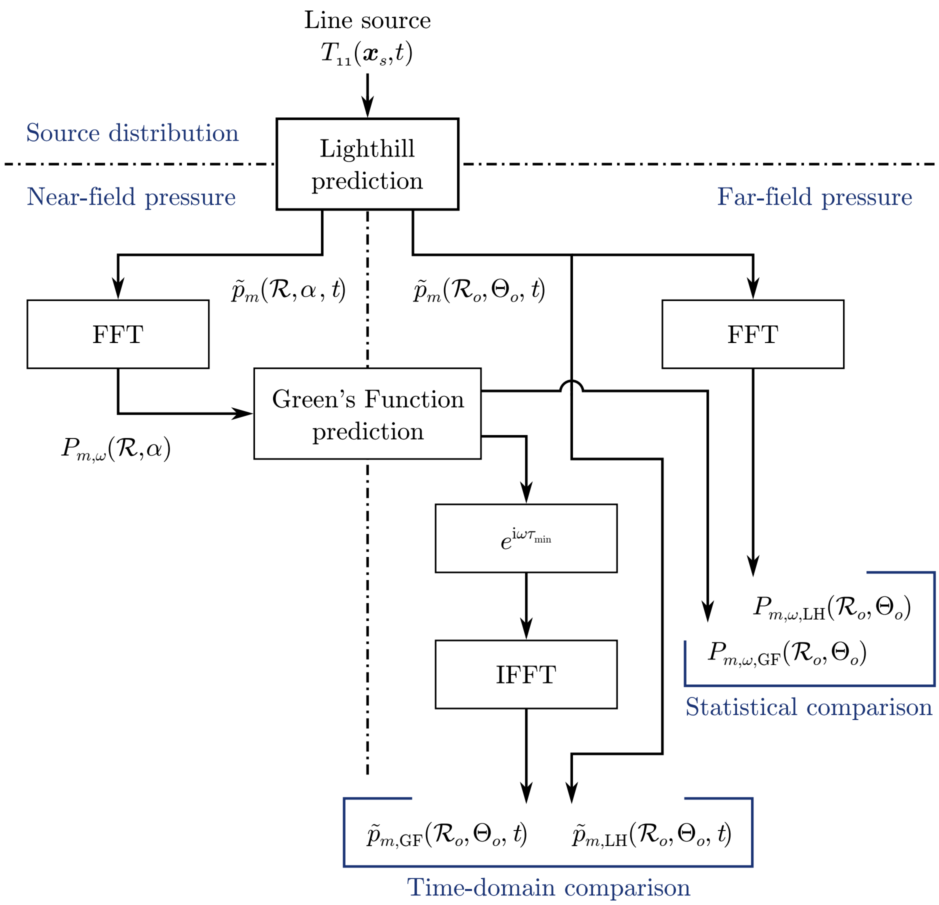

Figure B.1: Analysis procedure for time-domain far-field signal prediction

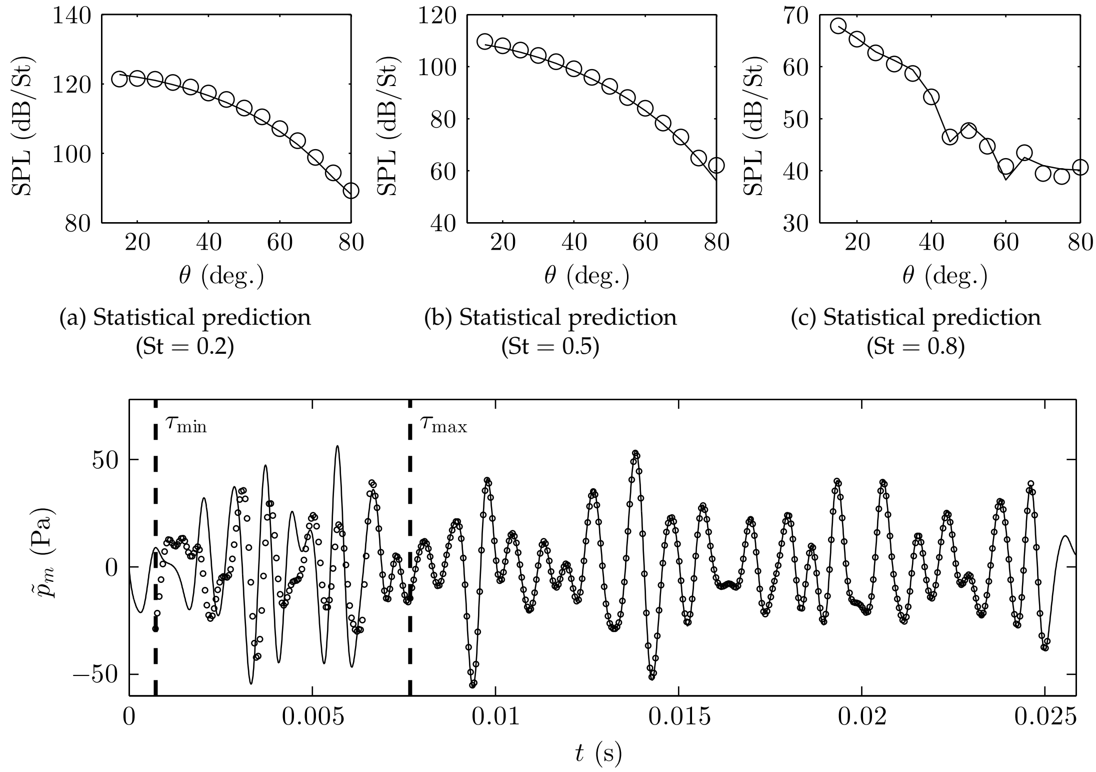

(a) Statistical prediction (St = 0.2)

(b) Statistical prediction (St = 0.5)

(c) Statistical prediction (St = 0.8)

(d) Time-domain prediction at $\theta = 20°$. (Every fifth data point of the Green's function result is shown.)

Figure B.2: Validation results for the far-field Green's function predictions from the near-field array with $X_0 \leq x/D \leq 70$. — Lighthill solution, ○ Green's function solution.

solution in both cases, verifying the propagation technique. In the time-domain case, the result shown is one block of $N = 2440$ points, and the points between $\tau_{\min}$ and $\tau_{\max}$ are corrupted as predicted.

B.2 Modelling the near-field Cross-Spectral Matrix (CSM)

In Reba *et al.*'s (2010) work, the authors used a curve fit with a model function to extend the CSM beyond the length of the experimental array. Their resulting far-field predictions were accurate for low θ. The same technique was also attempted here with both the validation problem and the experimental data but without such success. This is thought to be because of the effect of the spurious source created by the finite axial extent of the near-field microphone array, an effect that is less noticeable for higher Mach number. These comparisons are made with the data generated by the validation problem presented in appendix B.1 since the Mach number cannot be varied for the experimental data. Several different model functions were tested to extend the CSM.

Amplitude Models	$\lvert\mathbf{R}_{m,\omega}(x,x')\rvert$	Definitions
Coherent Analytical	$M_1(x)M_1(x')$	$M_1(x) = a\exp[-(x-b)^2/(cx+L)^2]$
Incoherent Analytical	$M_2(x,x')$	$M_2(x,x') = a\exp\left[-\dfrac{(x-b)^2}{(cx+L)^2} - \dfrac{(x'-b)^2}{(dx'+L')^2}\right]$
Generic Surface	$\mathcal{M}_3(x,x')$	$\mathcal{M}_3(x,x')$ is a generic non-linear surface fit
Reba *et al.* (2010)	$\sqrt{M_4(x)M_4(x')} \times \exp\left[-\dfrac{s}{L_{\text{corr}}(\bar{x})}\right]^2$	$M_4(x) = A(x/L_s)^{\gamma-1}e^{-\gamma x/L_s}$, $L_{\text{corr}}(\bar{x}) = B\bar{x} + C$, $\bar{x} = (x+x')/2$, $s = (x-x')/2$
Phase Models	$\arg(\mathbf{R}_{m,\omega}(x,x'))$	**Definitions**
Generic surface	$\text{unwrap}[\phi(x,x')] = \mathcal{P}_1(x,x')$	$\mathcal{P}_1(x,x')$ is a generic non-linear surface fit with linear extrapolation
Reba *et al.* (2010)	$\phi(\bar{x}) = 2s\kappa(\bar{x})$	$s = (x-x')/2$ and $\bar{x} = (x+x')/2$ with $\kappa(\bar{x})$ solved from a linear least-squares problem.

Table B.2: Tested models for the CSM beyond the experimental near-field array's axial extent

These are tabulated in table B.2. For the results presented here, only the generic surface phase model was used.

As the principal difference between the current dataset and Reba *et al.*'s (2010), Mach number was a natural parameter to investigate in the validation problem. r_A (the radius of the conical array at the jet exit) was also pertinent because it affects the rate of decay with increasing x of the pressure fluctuations on the near-field array, thereby changing the shape of the curve that needs to be modelled. Figure B.3 shows the effect of both Mach number and r_A on the accuracy of the directivity predictions. For the experimental conditions (figure B.3(a)), none of the models is able to accurately reproduce the directivity, though near $\theta = 40°$, all the predictions are accurate. While r_A has a noticeable effect for some models for low Mach number, the most significant thing to note is that for higher Mach number all the models collapse to the right directivity. This is despite the fact that the truncated, un-modelled estimate shows only moderate improvement at higher Mach number, implying that the chosen model does have an effect on the spurious source. This is probably because since the wavepacket source is nearly as strong as the spurious source as high Mach number only a small amount of smoothing (damping) at the edge of the array is sufficient to eliminate it's appearance in the directivity. In fact, for $M = 1.2$ (figure B.3(c)), the coherent model is sufficient to accurately predict the directivity. This helps explain the discrepancy

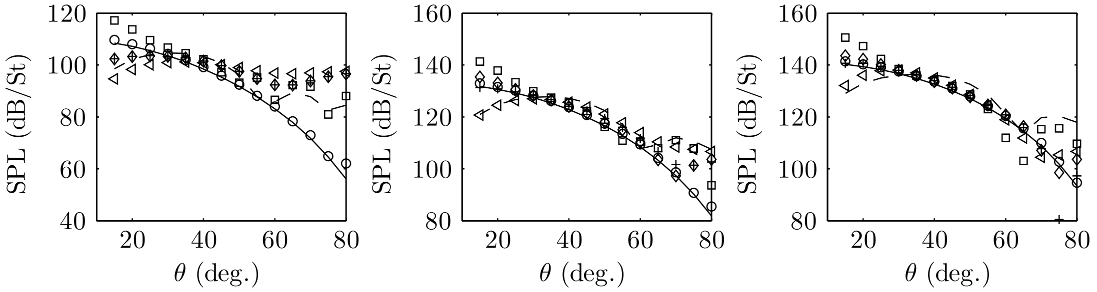

(a) $M = 0.6$ and $r_A = 0.8D$ (b) $M = 0.9$ and $r_A = 0.8D$ (c) $M = 1.2$ and $r_A = 0.8D$

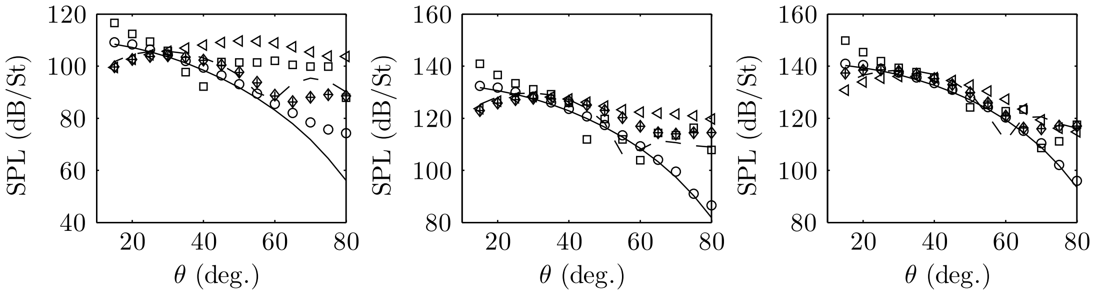

(d) $M = 0.6$ and $r_A = 0.04D$ (e) $M = 0.9$ and $r_A = 0.04D$ (f) $M = 1.2$ and $r_A = 0.04D$

Figure B.3: Effect of M and r_A on the far-field statistical predictions with different CSM models. — Lighthill solution, ○ $0 \leq x/D \leq 70$, – – $0.5 \leq x/D \leq 8.9$, + Coherent analytical, ◇ Incoherent analytical, □ Generic surface, ◁ Reba *et al.* (2010) model.

between Reba *et al.*'s (2010) application of this technique and the current results. In fact, it may help explain why Reba *et al.*'s (2010) results were so poor for their lower-Mach-number jets.

Appendix C

Further details of the SSIM analysis

C.1 Introduction

The Structural Similarity Metric (SSIM) analysis presented in chapter 5 includes some details that are unimportant in discussing the performance of the metric but that are important in reproducing the presented results. These details are included here.

C.2 SSIM definition

Wang *et al.*'s (2004) original definition of the SSIM, equation (5.3) was formulated in a slightly more flexible way than was used here:

$$\mathrm{SSIM}(x,y) = [l(x,y)]^{n_l} \cdot [c(x,y)]^{n_c} \cdot [s(x,y)]^{n_s}, \tag{C.1}$$

where $n_l > 0$, $n_c > 0$, and $n_s > 0$ weight the relative importance of each component of the metric. The advantage of this weighting is that the metric can be fine-tuned to best respond to the problem at hand. However, for initial testing purposes, the extra complication was unnecessary and, as was implied by equation (5.3), $n_l = n_c = n_s = 1$ was used in this case.

The choice of the constants C_1, C_2, and C_3 is not very important to the solution, but they must be used in the equation or the result becomes unstable when $\mu_x^2 + \mu_y^2$ or $(\sigma_x^2 + \sigma_y^2)$ are small. The constants chosen here were the same used by Wang *et al.* (2004). Mathematically, if $C_3 = 0$ both the SSIM and MSSIM are bounded in the range [-1,1], though for finite C_3, the lower bound is slightly higher.

C.3 Wavelet decomposition

The wavelet decomposition for the time–frequency WSSIM was carried out by a Continuous Wavelet Transform (CWT) (Torrence & Compo, 1998) using a complex-valued Morlet wavelet. The CWT is given as

$$\mathrm{CWT}[a(t)] = \int_{-\infty}^{\infty} a(\tau) \frac{1}{\sqrt{s}} \Psi^* \left(\frac{\tau - t}{s} \right) d\tau, \tag{C.2}$$

where $\Psi(\zeta)$ is the wavelet mother function and s is the scale of the analyzing wavelet, where ζ is a dummy variable. $\mathrm{CWT}[a(t)]$, a complex-valued function of both t and s, is the wavelet coefficient corresponding to the particular time delay and wavelet scale.

The complex-valued Morlet wavelet is defined by

$$\Psi(\zeta) = \pi^{-1/4} e^{\mathrm{i}\omega_0 \zeta} e^{\zeta^2/2}, \tag{C.3}$$

where ω_0 is the nondimensional frequency, which was chosen here as 6, corresponding to normal use of the Morlet wavelet (Torrence & Compo, 1998). The formula for converting the wavelet scale, s, into pseudo-frequencies is then (Torrence & Compo, 1998)

$$f_{\mathrm{pseudo}} = \frac{\omega_0 + \sqrt{2 + \omega_0^2}}{4\pi s}. \tag{C.4}$$

The moduli of the coefficients were then converted into an 'image' in the time–frequency domain as

$$\breve{a}(t, f_{\mathrm{pseudo}}) = |\mathrm{CWT}[a(t)]|. \tag{C.5}$$

C.4 Convolution window and weighting

C.4.1 WSSIM$_{\mathrm{1D}}$

The $p(t)$ signal is considered as an image with dimensions $N_t \times 1$. The convolution window is then $N_{ct} \times 1$. To calculate the WSSIM$_{\mathrm{1D}}$, it is necessary to define $w(x_j)$ as a local measure of the energy. For the simulation case, $w(x_j)$ is taken as the envelope of the reference signal, while in the experimental case, $w(x_j)$ was obtained by a Hilbert transform of the reference signal. The convolution window used was $N_{ct} \times 1 = 501 \times 1 \approx 6.1 T_0 \times 1$. It should be noted that a width equal to half the convolution window is trimmed off each side of each dimension, but this causes no difficulties in the 1D case because a slightly wider sample of the time series can be used just as easily.

C.4.2 WSSIM

The 'image' given by $\check{a}(t, f_{\text{pseudo}})$ has dimensions $N_t \times N_f$ where N_t is the number of samples in the time series, and N_f is the number of pseudo-frequency scales. The wavelet scales for the CWT were selected so that f_{pseudo} would be an evenly spaced series of 200 frequencies ranging from the experimental cut-off frequency (200 Hz) to the Nyquist frequency ($f_s/2 = 50\,000$ Hz) yielding $\Delta f \approx 250$ Hz. The weighting function, $w(x_j)$, in the WSSIM was then simply $\check{p}(t, f_{\text{pseudo}})$ of the reference signal since it is ensured to be greater than zero and representative of the local signal energy. The 2D convolution window used was rectangular and had dimensions $N_{ct} \times N_{cf} = 501 \times 3 \approx 6.1T_0 \times 1.2f_0$. Again, the trimming effect of the convolution poses no difficulty in the time dimension, and only two frequencies are lost in the frequency dimension since the convolution window is only three frequencies wide. Several other convolution window sizes were tested, but no significant deviations were observed.

References

ACARE-SRIA (2012) Strategic research & innovation agenda. Report, Advisory Council for Aviation Research and Innovation in Europe (ACARE).

Adrian RJ (1979) Conditional eddies in isotropic turbulence. *Physics of Fluids* 22:2065.

Armstrong RR, Michalke A, & Fuchs HV (1977) Coherent structures in jet turbulence and noise. *AIAA Journal* 15(7):1011–1017.

Arndt REA, Long DF, & Glauser MN (1997) The proper orthogonal decomposition of pressure fluctuations surrounding a turbulent jet. *Journal of Fluid Mechanics* 340:1–33.

Ashforth-Frost S & Jambunathan K (1996) Effect of nozzle geometry and semi-confinement on the potential core of a turbulent axisymmetric free jet. *International Communications in Heat and Mass Transfer* 23(2):155–162.

Atvars J, Schubert LK, Grande E, & Ribner H (1966) Refraction of sound by jet flow or jet temperature. Contractor Report NASA-CR-494, NASA, Toronto, Canada.

Berkooz G, Holmes P, & Lumley JL (1993) The proper orthogonal decomposition in the analysis of turbulent flows. *Annual Review of Fluid Mechanics* 25(1):539–575.

Bogey C & Bailly C (2007) An analysis of the correlations between the turbulent flow and the sound pressure fields of subsonic jets. *Journal of Fluid Mechanics* 583:71–97.

Bridges J (2002) Measurements of turbulent flow field in separate flow nozzles with enhanced mixing Devices—Test report. Technical Memorandum NASA/TM–2002-211366, NASA Glenn Research Center, Cleveland, Ohio.

Bridges J & Brown C (2004) Parametric testing of chevrons on single flow hot jets. Technical Memorandum NASA/TM–2004-213107; AIAA–2004-2824, NASA Glenn Research Center, Cleveland, Ohio.

Bridges J & Wernet M (2007) Effect of temperature on jet velocity spectra. Technical Memorandum NASA/TM–2007-214993; AIAA–2007-3628, NASA Glenn Research Center, Cleveland, Ohio.

Bridges J, Wernet M, & Brown C (2003) Control of jet noise through mixing enhancement. Technical Memorandum NASA/TM–2003-212335, NASA Glenn Research Center, Cleveland, Ohio.

Brown C & Bridges J (2006) Acoustic efficiency of azimuthal modes in jet noise using chevron nozzles. Technical Memorandum NASA/TM–2006-214364; AIAA–2006-2654, NASA Glenn Research Center, Cleveland, Ohio.

Bruun HH (1995) *Hot-wire anemometry: principles and signal analysis*. Oxford University Press, Oxford, United Kingdom.

Cavalieri AVG, Jordan P, Agarwal A, & Gervais Y (2011) Jittering wave-packet models for subsonic jet noise. *Journal of Sound and Vibration* 330(18-19):4474–4492.

Cavalieri AVG, Jordan P, Colonius T, & Gervais Y (2012a) Axisymmetric superdirectivity in subsonic jets. *Journal of Fluid Mechanics* 704:388–420.

Cavalieri AVG, Rodríguez D, Jordan P, Colonius T, & Gervais Y (2012b) Wavepackets in the velocity field of turbulent jets. In: *18th AIAA/CEAS Aeroacoustics Conference*, Colorado Springs, CO.

CFR-14 (2011) Title 14—Aeronautics and space: Part 36—Noise standards: aircraft type and airworthiness certification. Electronic Code of Federal Regulations. United States Code.

Chatellier L & Fitzpatrick J (2005) Spatio-temporal correlation analysis of turbulent flows using global and single-point measurements. *Experiments in Fluids* 38(5):563–575.

Crighton DG (1975) Basic principles of aerodynamic noise generation. *Progress in Aerospace Sciences* 16(1):31–96.

Crighton DG & Huerre P (1990) Shear-layer pressure fluctuations and superdirective acoustic sources. *Journal of Fluid Mechanics* 220:355–368.

Crow SC (1972) Acoustic gain of a turbulent jet. In: *Annual Meeting of the Division of Fluid Dynamics, American Physical Society*, Paper IE.6, Boulder, CO.

Crow SC & Champagne FH (1971) Orderly structure in jet turbulence. *Journal of Fluid Mechanics* 48(3):547–591.

DANTEC-HWA Probes for hot-wire anemometry. Dantec Dynamics. Educational Poster.

DANTEC-PIV Particle image velocimetry. Dantec Dynamics. Educational Poster.

Elsinga GE, Scarano F, Wieneke B, & Oudheusden BW (2006) Tomographic particle image velocimetry. *Experiments in Fluids* 41(6):933–947.

European Commission (2008) Report from the Commission to the Council and the European Parliament - Noise operation restrictions at EU airports - (Report on the application of directive 2002/30/EC). Technical report, European Commission, Brussels, Belgium.

Ffowcs Williams JE (1963) The noise from turbulence convected at high speed. *Philosophical Transactions of the Royal Society of London Series A, Mathematical and Physical Sciences* 255(1061):469–503.

Ffowcs Williams JE & Gordon C (1965) Noise of highly turbulent jets at low exhaust speeds. *AIAA Journal* 3(4):791–793.

Fisher MJ & Morfey CL (1982) Jet noise. In: White R & Walker JG (eds.) *Noise and vibration*, Ellis Horwood, Chichester, UK.

Fitzpatrick JA & Rice HJ (1988) Simplified partial coherence functions for multiple input/output analysis. *Journal of Sound and Vibration* 122(1):171–174.

Gliebe PR, Brausch J, Majjigi R, & Lee R (1991) Jet noise suppression. In: Hubbard HH (ed.) *Aeroacoustics of Flight Vehicles: Theory and Practice. Volume 2. Noise Control*, Reference Publication NASA/RP–1258-VOL-2. NASA Office of Management. Washington, DC, pp. 207–269.

Goldstein M (1974) Aeroacoustics. Special Publication NASA SP-346, NASA.

Goldstein M (2003) A generalized acoustic analogy. *Journal of Fluid Mechanics* 488:315–333.

Goldstein ME (2001) An exact form of Lilley's equation with a velocity quadrupole/temperature dipole source term. *Journal of Fluid Mechanics* 443:231–236.

Grizzi S & Camussi R (2012) Wavelet analysis of near-field pressure fluctuations generated by a subsonic jet. *Journal of Fluid Mechanics* 698:93–124.

Gudmundsson K & Colonius T (2011) Instability wave models for the near-field fluctuations of turbulent jets. *Journal of Fluid Mechanics* 689:97–128.

Haigermoser C (2009) Application of an acoustic analogy to PIV data from rectangular cavity flows. *Experiments in Fluids* 47(1):145–157.

Henderson B (2009) Fifty years of fluidic injection for jet noise reduction. *International Journal of Aeroacoustics* 9(1-2):91–122.

Henning A & Ehrenfried K (2008) On the accuracy of one-point and two-point statistics measured via high-speed PIV. In: *14th International Symposium on the Application of Laser Techniques to Fluid Mechanics*, Lisbon, Portugal.

Henning A, Kaepernick K, Ehrenfried K, Koop L, & Dillmann A (2008) Investigation of aeroacoustic noise generation by simultaneous particle image velocimetry and microphone measurements. *Experiments in Fluids* 45(6):1073–1085.

Henning A, Koop L, & Ehrenfried K (2010a) Causality correlation in aeroacoustic experiments by means of simultaneous PIV and microphone-array. In: *3rd Berlin Beamforming Conference*, Berlin, Germany.

Henning A, Schröder A, Krebs I, & Agocs J (2010b) Aeroacoustic investigations on a cold jet by means of simultaneous PIV and microphone measurements. In: *15th International Symposium on Applications of Laser Techniques to Fluid Mechanics*.

Herbert T (1997) Parabolized stability equations. *Annual Review of Fluid Mechanics* 29(1):245–283.

Herkes W, Olsen R, & Uellenberg S (2006) The Quiet Technology Demonstrator program: Flight validation of airplane noise-reduction concepts. In: *12th AIAA/CEAS Aeroacoustics Conference*, Cambridge, MA.

Hines A & Harte N (2012) Speech intelligibility prediction using a neurogram similarity index measure. *Speech Communication* 54(2):306–320.

Hines A, Skoglund J, Kokaram A, & Harte N (2012) ViSQOL: the virtual speech quality objective listener. In: *Proceedings of the International Workshop on Acoustic Signal Enhancement*, Aachen, Germany, pp. 1–4.

Hinsch KD (1995) Three-dimensional particle velocimetry. *Measurement Science and Technology* 6:742–753.

Hirschberg A (2001) Introduction to aero-acoustics of internal flows. In: Antoine J & Schram C (eds.) *Advances in Aeroacoustics*, Von Karman Institute for Fluid Dynamics, Rhode-St-Genese, Belgium, pp. 1–112.

ICAO-ER (2010) ICAO environmental report 2010. Technical report, International Civil Aviation Organization (ICAO), Montreal, Canada.

Jordan P & Colonius T (2013) Wave packets and turbulent jet noise. *Annual Review of Fluid Mechanics* 45(1):173–195.

Jordan P & Gervais Y (2007) Subsonic jet aeroacoustics: associating experiment, modelling and simulation. *Experiments in Fluids* 44(1):1–21.

Jung D, Gamard S, & George WK (2004) Downstream evolution of the most energetic modes in a turbulent axisymmetric jet at high Reynolds number. Part 1. The near-field region. *Journal of Fluid Mechanics* 514:173–204.

Kastner J, Kim J, & Samimy M (2006) Noise sources in controlled high reynolds number and high speed jets. In: *12th AIAA/CEAS Aeroacoustics Conference*, Cambridge, MA.

Keane RD & Adrian RJ (1990) Optimization of particle image velocimeters. I. Double pulsed systems. *Measurement Science and Technology* 1:1202–1215.

Kennedy J (2010) The influence of chevrons on the turbulent characteristics of jets. PhD thesis, University of Dublin – Trinity College, Dublin, Ireland.

Kennedy J & Fitzpatrick J (2010) The effect of chevrons on the turbulence characteristics of jets. In: *16th AIAA/CEAS Aeroacoustics Conference*, Stockholm, Sweden.

Kerhervé F & Fitzpatrick J (2010) Measurement and analysis of the turbulent length scales in jet flows. *Experiments in Fluids* 50(3):637–651.

Kerhervé F, Guitton A, Jordan P, Delville J, Fortuné V, Gervais Y, & Tinney C (2008) Identifying the dynamics underlying the large-scale and fine-scale jetnoise similarity spectra. In: *14th AIAA/CEAS Aeroacoustics Conference*, Vancouver, Canada.

Kerhervé F, Fitzpatrick J, & Kennedy J (2010) Determination of two-dimensional space–time correlations in jet flows using simultaneous PIV and LDV measurements. *Experimental Thermal and Fluid Science* 34(6):788–797.

Kerhervé F, Jordan P, Cavalieri AVG, Delville J, Bogey C, & Juvé D (2012) Educing the source mechanism associated with downstream radiation in subsonic jets. *Journal of Fluid Mechanics* 710:606–640.

Kœnig M, Fourment-Cazenave C, Jordan P, & Gervais Y (2011) Jet noise reduction by fluidic injection from a rotating plug. In: *17th AIAA/CEAS Aeroacoustics Conference*, Portland, Oregon.

Kœnig M, Cavalieri AVG, Jordan P, & Gervais Y (2013) Jet-noise control by fluidic injection from a rotating plug: linear and non-linear sound source mechanisms. In: *19th AIAA/CEAS Aeroacoustics Conference*, Berlin, Germany.

Koschatzky V, Moore P, Westerweel J, Scarano F, & Boersma B (2011) High speed PIV applied to aerodynamic noise investigation. *Experiments in Fluids* 50(4):863–876.

Laurendeau E, Jordan P, Bonnet JP, Delville J, Parnaudeau P, & Lamballais E (2008) Subsonic jet noise reduction by fluidic control: The interaction region and the global effect. *Physics of Fluids* 20:101,519.

Lee HK & Ribner H (1972) Direct correlation of noise and flow of a jet. *The Journal of the Acoustical Society of America* 52(5A):1280–1290.

Léon O (2012) Étude du rayonnement acoustique des instabilités hydrodynamiques de jets double-flux par les équations de stabilité parabolisées (PSE). PhD thesis, University of Toulouse, Toulouse, France, English title: *Acoustics of hydrodynamic instabilities in dual-stream jets using parabolized stability equations (PSE)*.

Léon O & Brazier J (2011) Application of the linear Parabolized Stability Equations to a subsonic coaxial jet. In: *17th AIAA/CEAS Aeroacoustics Conference*, Portland, Oregon.

Léon O & Brazier J (2013) Investigation of near and far pressure fields of dual-stream jets using an euler-based PSE model. In: *19th AIAA/CEAS Aeroacoustics Conference*, Berlin, Germany.

Lighthill MJ (1952) On sound generated aerodynamically: I. General theory. *Proceedings of the Royal Society of London Series A Mathematical and Physical Sciences* 211(1107):564–587.

Lighthill MJ (1954) On sound generated aerodynamically: II. Turbulence as a source of sound. *Proceedings of the Royal Society of London Series A, Mathematical and Physical Sciences* 222(1148):1–32.

Lighthill MJ (1962) The Bakerian lecture, 1961: Sound generated aerodynamically. *Proceedings of the Royal Society of London Series A, Mathematical and Physical Sciences* 267(1329):147–182.

Lilley GM (1973) On the noise from jets. In: *Noise Mechanisms; AGARD-CP-131*, NATO Advisory Group for Aerospace Research and Development (AGARD), Brussels, Belgium, pp. 13—1–13–12.

Lilley GM (1991) Jet noise classical theory and experiments. In: Hubbard HH (ed.) *Aeroacoustics of Flight Vehicles: Theory and Practice. Volume 1. Noise Sources*, Reference Publication NASA/RP–1258-VOL-1. NASA Office of Management. Washington, DC, pp. 211–289.

Lyrintzis AS (1994) Review: the use of Kirchhoff's method in computational aeroacoustics. *Journal of Fluids Engineering* 116(4):665–676.

Martens S & Haber L (2008) Jet noise reduction for high speed exhaust systems. In: *Proceedings of ASME Turbo Expo 2008: Power for Land, Sea and Air*, Berlin, Germany.

Maury R, Cavalieri AVG, Jordan P, Delville J, & Bonnet JP (2011) Jet noise reduction using pulsed fluidic actuation. In: *7th International Symposium on Turbulence and Shear Flow Phenomema*, Ottawa, Canada.

Maury R, Koenig M, Cattafesta L, Jordan P, & Delville J (2012) Extremum-seeking control of jet noise. *International Journal of Aeroacoustics* 11(3-4):459–474.

Mollo-Christensen E (1963) Measurements of near field pressure of subsonic jets. Technical Report ASRL TR 1009, Massachusetts Institute of Technology, Aeroelastic and Structures Research Laboratory, Cambridge, MA.

Mollo-Christensen E (1967) Jet noise and shear flow instability seen from an experimenter's viewpoint. Contractor Report NASA/CR–93838, NASA.

Morris PJ & Boluriaan S (2004) The prediction of jet noise from CFD data. In: *10th AIAA/CEAS Aeroacoustics Conference*, Manchester, United Kingdom.

Morris PJ & Viswanathan K (2011) Jet noise. In: *Noise Sources in Turbulent Shear Flows*, Course Notes, International Centre for Mechanical Sciences, Udine, Italy.

Morris PJ & Zaman K (2010) Velocity measurements in jets with application to noise source modeling. *Journal of Sound and Vibration* 329(4):394–414.

Morris SC (2011) Shear-layer instabilities: Particle Image Velocimetry measurements and implications for acoustics. *Annual Review of Fluid Mechanics* 43(1):529–550.

Nogueira J, Lecuona A, Nauri S, Legrand M, & Rodríguez PA (2011) Quantitative evaluation of PIV peak locking through a multiple Δt strategy: relevance of the rms component. *Experiments in Fluids* 51(3):785–793.

Panda J (2005) Identification of noise sources in high speed jets via correlation measurements: A review. Contractor Report NASA/CR–2005-213817, NASA Glenn Research Center, Cleveland, Ohio.

Papamoschou D, Morris PJ, & Mclaughlin DK (2010) Beamformed flow–acoustic correlations in a supersonic jet. *AIAA Journal* 48(10):2445–2453.

Peart NA, Smith MJT, Magliozzi B, & Sternfield H (1991) Flyover-noise measurement and prediction. In: Hubbard HH (ed.) *Aeroacoustics of Flight Vehicles: Theory and Practice. Volume 2. Noise Control*, Reference Publication NASA/RP–1258-VOL-2. NASA Office of Management. Washington, DC, pp. 357–382.

Phillips OM (1960) On the generation of sound by supersonic turbulent shear layers. *Journal of Fluid Mechanics* 9:1–28.

Powers RW, Kuo C, & McLaughlin DK (2013) Experimental comparison of supersonic jets exhausting from military style nozzles with interior corrugations and fluidic inserts. In: *19th AIAA/CEAS Aeroacoustics Conference*, Berlin, Germany.

Proudman I (1952) The generation of noise by isotropic turbulence. *Proceedings of the Royal Society A: Mathematical, Physical and Engineering Sciences* 214(1116):119–132.

Rackl R (1973) Two causality correlation techniques applied to jet noise. PhD thesis, University of British Columbia, Vancouver, Canada.

Raffel M, Willert C, Wereley S, & Kompenhans J (2007) *Particle Image Velocimetry: A Practical Guide*, 2nd edn. Springer-Verlag, Berlin, Germany.

Reba R, Narayanan S, & Colonius T (2010) Wave-packet models for large-scale mixing noise. *International Journal of Aeroacoustics* 9(4-5):533–558.

Reba R, Simonich J, & Schlinker R (2012) Chevron nozzle effects on wavepacket sources in a supersonic jet. In: *18th AIAA/CEAS Aeroacoustics Conference*, Colorado Springs, CO.

Richarz WG (1978) Direct correlation of noise and flow of a jet using Laser Doppler. UTIAS Report 230, University of Toronto Institute for Aerospace Studies, Toronto, Canada.

Rienstra S & Hirschberg A (2010) An introduction to acoustics. Technical Report IWDE 92-06, Eindhoven University of Technology.

Ruppert-Felsot J, Farge M, & Petitjeans P (2009) Wavelet tools to study intermittency: application to vortex bursting. *Journal of Fluid Mechanics* 636:427–453.

Samanta A, Freund JB, Wei M, & Lele SK (2006) Robustness of acoustic analogies for predicting mixing-layer noise. *AIAA Journal* 44(11):2780–2786.

Samimy M, Adamovich I, Webb B, Kastner J, Hileman J, Keshav S, & Palm P (2004) Development and characterization of plasma actuators for high-speed jet control. *Experiments in Fluids* 37(4):577–588.

Sandham N, Morfey C, & Hu Z (2006) Sound radiation from exponentially growing and decaying surface waves. *Journal of Sound and Vibration* 294(1-2):355–361.

Scarano F, Bryon K, & Violato D (2010) Time-resolved analysis of circular and chevron jets transition by Tomo-PIV. In: *15th International Symposium on Applications of Laser Techniques to Fluid Mechanics*, Lisbon, Portugal.

Schaffar M (1979) Direct measurements of the correlation between axial in-jet velocity fluctuations and far field noise near the axis of a cold jet. *Journal of Sound and Vibration* 64(1):73–83.

Schröder A, Dierksheide U, Wolf J, Herr M, & Kompenhans J (2004) Investigation on trailing-edge noise sources by means of high-speed PIV. In: *12th International Symposium on the Application of Laser Techniques to Fluid Mechanics*, Lisbon, Portugal.

Seiner JM (1998) A new rational approach to jet noise reduction. *Theoretical and Computational Fluid Dynamics* 10(1-4):373–383.

Self R (2004) Jet noise prediction using the Lighthill acoustic analogy. *Journal of Sound and Vibration* 275(3-5):757–768.

Siddon TE (1970) Surface dipole strength for flow past airfoils. *The Journal of the Acoustical Society of America* 48(1A):75.

Suzuki T & Colonius T (2006) Instability waves in a subsonic round jet detected using a near-field phased microphone array. *Journal of Fluid Mechanics* 565:197–226.

Tam C (1998) Jet noise: Since 1952. *Theoretical and Computational Fluid Dynamics* 10(1-4):393–405.

Tam CKW, Golebiowski M, & Seiner J (1996) On the two components of turbulent mixing noise from supersonic jets. Contractor Report NASA/CR–202816; AIAA–96-1716, NASA Langley Research Center, Hampton, Virginia.

Tam CKW, Viswanathan K, Ahuja K, & Panda J (2008) The sources of jet noise: experimental evidence. *Journal of Fluid Mechanics* 615:253–292.

Tanna H, Dean P, & Fisher M (1975) The influence of temperature on shock-free supersonic jet noise. *Journal of Sound and Vibration* 39(4):429–460.

Tinney CE & Jordan P (2008) The near pressure field of co-axial subsonic jets. *Journal of Fluid Mechanics* 611:175–204.

Torrence C & Compo GP (1998) A practical guide to wavelet analysis. *Bulletin of the American Meteorological Society* 79(1):61–78.

Violato D & Scarano F (2011) Three-dimensional evolution of flow structures in transitional circular and chevron jets. *Physics of Fluids* 23(124104).

Viswanathan K (2004) Aeroacoustics of hot jets. *Journal of Fluid Mechanics* 516:39–82.

Viswanathan K (2006) Scaling laws and a method for identifying components of jet noise. *AIAA Journal* 44(10):2274–2285.

Viswanathan K (2010) Best practices for accurate measurement of pure jet noise. *International Journal of Aeroacoustics* 9(1-2):145–206.

Wang Z, Bovik A, Sheikh H, & Simoncelli E (2004) Image quality assessment: from error visibility to structural similarity. *IEEE Transactions on Image Processing* 13(4):600–612.

Wernet M (2007a) Time-resolved PIV for space–time correlations in hot jets. In: *22nd International Congress on Instrumentation in Aerospace Simulation Facilities, 2007. ICIASF 2007*, pp. 1–11.

Wernet MP (2007b) Temporally resolved PIV for space–time correlations in both cold and hot jet flows. *Measurement Science and Technology* 18(5):1387.

WHO-NNGL (2007) Night noise guidelines (NNGL) for Europe. Final implementation report, World Health Organization, Regional Office for Europe, European Centre for Environment and Health.

Willert C & Gharib M (1991) Digital particle image velocimetry. *Experiments in Fluids* 10(4):181–193.